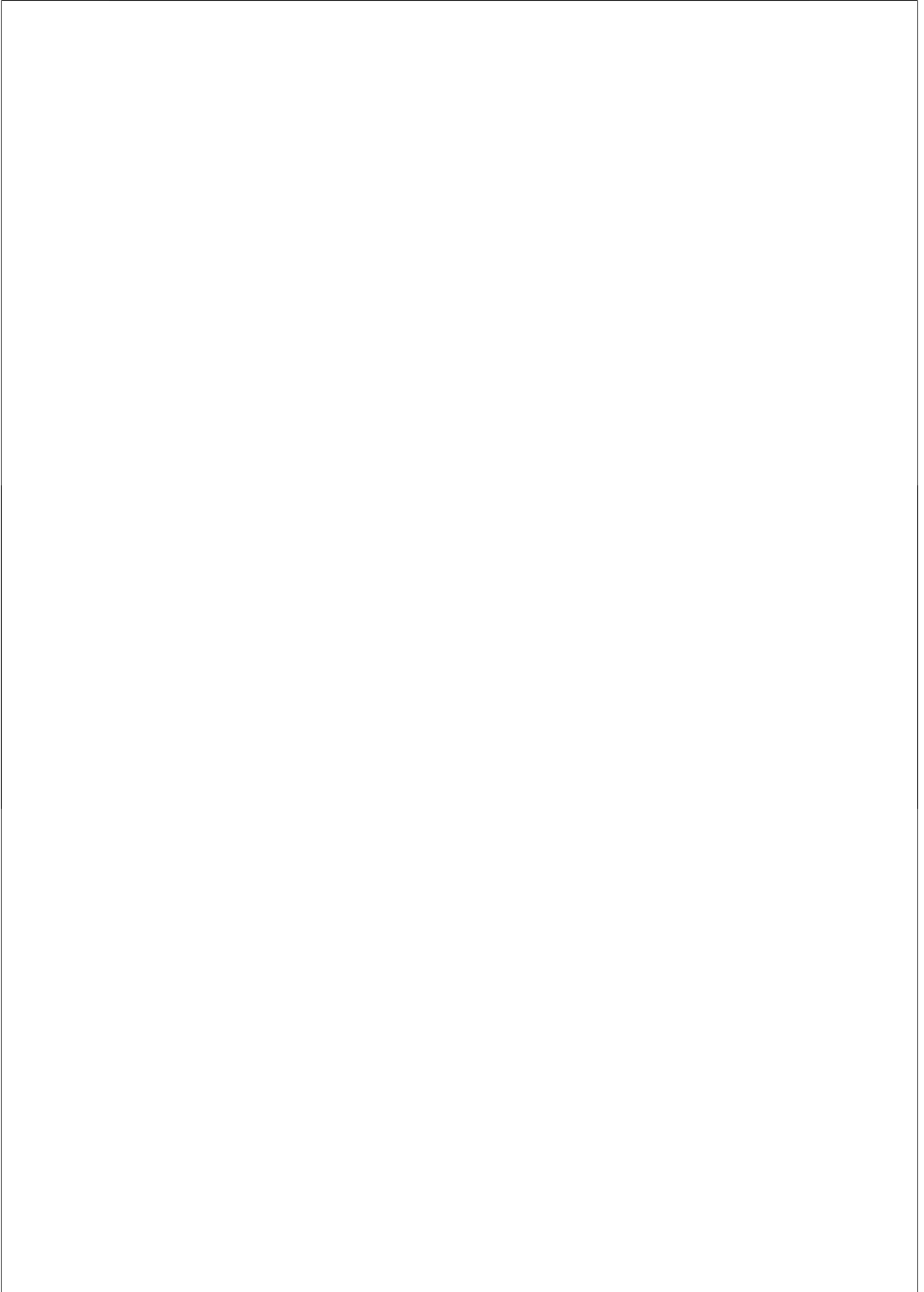


Transparent Conductive Oxides for Thin-Film Silicon Solar Cells



Transparent Conductive Oxides for Thin-Film Silicon Solar Cells

**Transparante geleidende oxides
voor dunne film silicium zonnecellen**

(met een samenvatting in het Nederlands)

PROEFSCHRIFT

TER VERKRIJGING VAN DE GRAAD VAN DOCTOR
AAN DE UNIVERSITEIT UTRECHT OP GEZAG VAN
DE RECTOR MAGNIFICUS, PROF. DR. W. H. GISPEN,
INGEVOLGE HET BESLUIT VAN HET COLLEGE VOOR
PROMOTIES IN HET OPENBAAR TE VERDEDIGEN OP
MAANDAG 25 APRIL 2005 DES MIDDAGS TE 14.30 UUR

DOOR

Jochen Löffler

GEBOREN OP 17 SEPTEMBER 1971 TE ULM

PROMOTOR: PROF. DR. R. E. I. SCHROPP

Faculteit Natuur- en Sterrenkunde
Universiteit Utrecht

The work described in this thesis was partially supported by the Netherlands Agency for Energy and the Environment (SenterNovem).

Druk: PrintPartners Ipskamp, Enschede

ISBN 90-393-06702

Contents

| | | |
|----------|---|-----------|
| 1 | Introduction | 7 |
| 1.1 | Solar Energy | 7 |
| 1.2 | Thin-Film Silicon Solar Cells | 8 |
| 1.3 | Transparent Conductive Oxides | 11 |
| 1.4 | Aim and Outline of this Thesis | 16 |
| 2 | Experimental | 19 |
| 2.1 | Sample Preparation | 19 |
| 2.1.1 | TCO Fabrication | 19 |
| 2.1.2 | Solar Cell Deposition | 21 |
| 2.2 | Layer Characterization | 24 |
| 2.2.1 | UV VIS Spectroscopy | 24 |
| 2.2.2 | Angular Resolved Scattering | 27 |
| 2.2.3 | Raman Spectroscopy | 27 |
| 2.2.4 | Activation Energy of Dark Conductivity | 28 |
| 2.3 | Device Characterization | 28 |
| 2.3.1 | Solar simulator | 28 |
| 2.3.2 | Spectral Response | 30 |
| 3 | Properties of Undoped and Aluminum Doped Zinc Oxide Layers | 31 |
| 3.1 | Introduction | 31 |
| 3.2 | Experimental | 31 |
| 3.3 | Reference TCOs | 33 |
| 3.4 | Undoped Zinc Oxide | 35 |
| 3.4.1 | Layer Thickness | 36 |
| 3.4.2 | Substrate Temperature | 37 |
| 3.4.3 | Oxygen Flow | 47 |
| 3.4.4 | Argon Flow through the Cascaded Arc | 51 |
| 3.5 | Aluminum Doped Zinc Oxide | 54 |
| 3.5.1 | TMA Flow | 54 |
| 3.5.2 | Substrate Temperature | 58 |
| 3.5.3 | Ar Flow through the Cascaded Arc | 61 |
| 3.6 | Conclusions | 65 |

| | | |
|----------|--|------------|
| 4 | Solar Cells on Zinc Oxide Superstrates | 67 |
| 4.1 | Introduction | 67 |
| 4.2 | Light trapping in Solar Cells | 68 |
| 4.2.1 | Scattering at Rough Interfaces | 68 |
| 4.2.2 | Modelling of Light Propagation through the Solar Cell Structure | 71 |
| 4.3 | Non-ideal Solar Cells | 76 |
| 4.4 | Experimental | 79 |
| 4.5 | a-Si pin Cells on Reference Substrates | 80 |
| 4.6 | The ZnO / p-Layer Interface | 82 |
| 4.6.1 | The TCO / p Interface | 83 |
| 4.6.2 | Development of Microcrystalline Silicon p-Layers | 84 |
| 4.6.3 | Microcrystalline Silicon p-Layers in pin Solar Cells on ZnO:Al | 87 |
| 4.7 | a-Si pin Cells on Undoped ZnO Superstrates | 89 |
| 4.8 | a-Si pin Cells on Doped ZnO:Al Superstrates | 95 |
| 4.9 | Microcrystalline Silicon Solar Cells | 103 |
| 4.10 | Conclusions | 105 |
| 5 | Fluorinated Tin Oxide by Atmospheric Pressure Chemical Vapor De- position | 109 |
| 5.1 | Introduction | 109 |
| 5.2 | Atmospheric Pressure Chemical Vapor Deposition of Fluorinated Tin Oxide | 109 |
| 5.3 | Experimental | 110 |
| 5.4 | Results and Discussion | 111 |
| 5.4.1 | SnO ₂ :F Layers | 111 |
| 5.4.2 | Solar Cells | 115 |
| 5.5 | Conclusions | 118 |
| 6 | Summary | 121 |
| | References | 127 |
| | Samenvatting | 137 |
| | List of publications | 141 |
| | Nawoord | 145 |
| | Curriculum Vitae | 147 |

1 Introduction

This chapter provides a general introduction to the thesis, motivating the relevance of solar energy as a source of electricity from an environmental point of view, and discussing the related economic issues. The advantages of thin-film silicon solar cells are deduced. A short overview over this field is given, and the important role of the transparent conductive oxide (TCO) for this type of solar cells is introduced. After an overview of the most common TCO materials, their properties and growth, the aim and outline of the thesis are explained.

1.1 Solar Energy

In recent years, the need for renewable energy sources has become evident. Apart from the discussion on the amount of accessible resources for conventional electricity production, scientific studies have proven recently that at least part of the global warming is indeed due to human activity leading to an increase in CO₂ concentration in the earth atmosphere, and is thus closely related to electricity production and energy consumption [1,2].

In 1997, the European Union has targeted a 100-fold increase in the power generated by photovoltaic systems [3]. By 2010, a capacity of 3 GW_p¹ has to be installed. Due to the fast growing markets, especially in Japan and Germany, the largest producers of solar cells, Sanyo in Japan, and Q-Cells AG in Germany, have recently announced plans to extend their production capacity beyond 1 GW_p per year [4,5]. Even in these scenarios, with annual growth rates of 30%, it will take until 2030 before PV has gained a significant share in the global energy production. Following the scientific council of the German Government, the projected share of global energy supply covered by PV and solar thermal systems will further increase to 20% by 2050, and it will become the major energy source by the end of this century [6].

While photovoltaic systems have become a mature technology for reliable electricity supply, they can currently only compete in markets with feed-in incentives, in subsidized markets, and for remote applications where no electricity grid is available. If society does not accept the current price for electricity from

¹The unit W_p stands for Watt peak and represents a system which generates 1 W under conditions with clear skies (AM 1.5 spectrum with 100 mW/cm² insulation).

renewable energy sources for ecological reasons, a drastic reduction in the cost of electricity supplied by photovoltaic systems is needed in order to achieve the above mentioned targets. A photovoltaic system consists of one or more solar modules which actually convert the sunlight into DC electricity, a DC/AC converter for grid connection, and the so-called balance of system components necessary to install the system. Currently, the module amounts for approximately 50% of the system cost. In crystalline silicon technology, such a module consists of a number of solar cells laminated into a frame. The solar cells are fabricated from highly purified crystalline silicon wafers with a thickness of typically 300 μm . Standard modules often have 36 cells of 5 by 5 to 6 by 6 inch in size. The first 8 inch cells have been presented recently, and efforts are ongoing to decrease the thickness of the silicon wafers below 150 μm . In spite of these developments, the large amount and extreme purity of silicon, which is still needed for the production of these thick wafer type crystalline silicon solar cells, limits the potential for cost reduction.

In contrast to the self-supporting wafer type crystalline silicon solar cells, thin-film solar cells can be deposited on cheaper substrates like glass, metal foils, or even plastic foils. They have in general the advantage of 100 to 1000 times thinner absorber layers, reducing the material cost in production substantially. For thin-film silicon solar cells also the requirements for the material purity and quality are greatly relieved. Thin-film modules can be directly fabricated on the substrate by monolithic series integration, thus avoiding the intermediate production step of individual cells as in crystalline silicon wafer technology. When deposited on foil, potentially cheap roll-to-roll production techniques can be applied [7]. What is more, reduction in balance of system cost is feasible for thin-film solar cells when they are directly deposited onto roof and facade building materials.

Therefore, the PVnet roadmap [8] published in 2004 by a consortium of European PV companies, research institutes and University groups predicts that thin-film silicon will gain a share of 10% of installed PV power by 2010, and by 2020 this share will increase to 30%.

1.2 Thin-Film Silicon Solar Cells

Thin-film silicon solar cells are often separated into three categories [9], depending on the highest temperature during the fabrication of the silicon layers. The high temperature approach with temperatures above 650°C allows the growth of high quality crystalline silicon films, either on foreign substrates like ceramics, or epitaxial growth on defective silicon. The medium temperature approach makes

use of temperatures between 400°C and 650°C for the deposition of polycrystalline silicon on seed layers or solid phase crystallization of an amorphous silicon film deposited at a lower temperature of typically 200°C. The obtained materials are aimed for high crystalline quality allowing high carrier lifetimes, which are sufficient for a diffusion type solar cell, where the transport of photoexcited charge carriers is mainly driven by diffusion. In such a device, the diffusion length of the charge carriers has to be larger than the absorber thickness of the solar cell [10].

This thesis is focused on the low temperature type of thin-film silicon solar cells which are deposited at temperatures below 400°C by plasma enhanced chemical vapor deposition (PECVD) from silane (SiH_4) containing gas mixtures. For this thesis, the deposition temperature for silicon layers did not exceed 200°C. At these low temperatures, generally an amorphous network is formed. Amorphous silicon (a-Si) is characterized by the absence of long range order, which is characteristic for the crystalline solid phase. The short range order in a-Si is similar to that of crystalline silicon, so that most of the silicon atoms are bonded to four silicon atoms. The bond angle and bond length distribution are broadened compared to the crystalline case by 10% and 3%, respectively [11]. This results in a characteristic density-of-states distribution with exponential band tails representing localized states within the forbidden gap. Due to the low deposition temperature, not all silicon atoms are 4-fold coordinated in the amorphous network. Unsaturated bonds, so-called dangling bonds, generate localized states in the middle of the band gap acting as effective recombination centers. Thus, for solar cell applications, hydrogenated amorphous silicon (a-Si:H) is used which contains about 10% hydrogen that saturates the vast majority of the dangling bonds. Device quality a-Si:H has a dangling bond density below 10^{16} cm^{-3} [12]. An important issue for its application in solar cells is the degradation of amorphous silicon under light exposure. Staebler and Wronski found that the dangling bond density of amorphous silicon increases under light exposure [13]. The created defects are metastable and can be annealed e.g. by exposure of the material to elevated temperature. In practical solar cell operation, the defect density stabilizes at an equilibrium level depending on the intensity and spectrum of the light, operating temperature, and electrical load [14]. The microscopic mechanisms involved in the defect creation, especially the role of hydrogen, are still under discussion [15]. Certainly nonradiative recombination of charge carriers at least indirectly attributes to the energy necessary to break a so called weak (i.e. strained) Si-Si bond for the dangling bond creation [16].

The band gap of amorphous silicon can be defined as a mobility gap, such that the band edge separates mobile carriers from those trapped in localized states. De-

pending on the deposition conditions, a wider band gap around 1.7 eV for device quality amorphous silicon compared to the 1.1 eV for crystalline silicon is obtained. Due to the absence of long range order, the momentum conservation rule for photon absorption is relieved. Therefore amorphous silicon has a high absorption coefficient for wavelengths above the band gap energy like a semiconductor with direct band gap, in contrast to the indirect band gap of crystalline silicon. Substitutional doping with boron and phosphorus [17] enables to deposit p - and n - doped amorphous silicon layers.

Under certain deposition conditions, e.g. high hydrogen dilution, microcrystalline silicon ($\mu\text{c-Si}$) is obtained, which is a two phase material consisting of silicon crystallites with nanometer size in an amorphous matrix. If the crystalline fraction of this material is high enough, the effective optical band gap approaches the value of 1.1 eV as for crystalline silicon. The combination of the band gaps of 1.7 eV for amorphous silicon and 1.1 eV for microcrystalline silicon is optimum for a stacked tandem solar cell [18]. This 'micromorph' concept was first proposed and realized by Meier *et al.* [19], and cell efficiencies up to 14.7% have recently been achieved [20].

The high defect density and thus low carrier lifetime even in the intrinsic absorber material of amorphous and microcrystalline silicon solar cells require a drift type solar cell, see Figure 1.1. An electric field, which is built up by the p- and n- doped layers, extends throughout the entire intrinsic layer and thus assists the collection of photoexcited charge carriers. It is evident that a higher field is obtained when the intrinsic layer of the solar cell becomes thinner. This is especially important under operating conditions and after degradation, when the field in the middle of a thick cell would collapse as a result of higher carrier and defect concentrations, respectively. Thus, a cell with thinner intrinsic absorber layer exhibits better stability against light degradation.

On the other hand, a thicker cell allows more light to be absorbed and thus results in a higher photocurrent generation especially for light with long wavelengths above 600 nm. For these wavelengths the absorption coefficient of amorphous silicon is low, so that the absorption length exceeds the thickness of the intrinsic absorber layer of the solar cell. Deckman *et al.* [21] introduced the concept of optical enhancement of amorphous silicon solar cells by increasing the effective optical path length of the light through the solar cell structure. This is achieved by a combination of light scattering at rough interfaces in combination with a highly reflective back contact. Multiple (total) internal reflections can then lead to virtual 'trapping' of the light in the solar cell, and thus enhance the absorption and photocurrent generation especially for light that has an absorption length that is longer than the thickness of the intrinsic absorber layer.

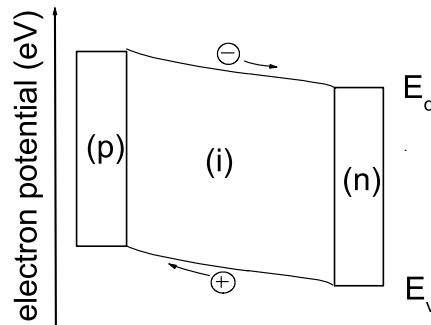


Figure 1.1: Band diagram of a pin drift type solar cell showing schematically the edges of the conduction and valence bands, E_c and E_v , under operating conditions of the solar cell.

Technologically, one distinguishes between pin and nip cells, named after the sequence in which the individual layers are being deposited. In both configurations, the p-layer is situated on the side where light enters the cell. Thus, nip cells can be deposited on opaque substrates like metal foil, while pin cells have to be deposited on transparent superstrates like glass. On the other hand, series connection of individual solar cells into large-area modules is easier achieved in pin configuration than for nip cells on conductive substrates. Currently, both concepts are followed in research [22,23] and industry [20,24]. This thesis focuses on single junction pin type amorphous and microcrystalline silicon solar cells.

1.3 Transparent Conductive Oxides

While the rear contact of the cells is composed of a highly conducting metal, due to the relatively low conductivity of the p-type amorphous and microcrystalline layers in the order of $10^{-5} \Omega^{-1}cm^{-1}$ and $10^{-2} \Omega^{-1}cm^{-1}$, at the p-side of the cell an additional layer has to be implemented in order to allow lateral conduction with low resistive losses over distances in the order of one centimeter, which are common in practical thin-film silicon modules. As this electrode layer is situated at the front side of the solar cell, where the light enters the device, in addition to a high lateral electrical conductivity, this layer has to exhibit a high optical transmittance to the sunlight. Metal oxides belonging to the class of transparent conductive oxides (TCOs) combine these two properties. Transparent conductive

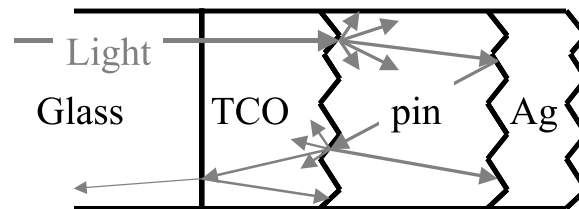


Figure 1.2: Light trapping in a pin type thin-film silicon solar cell with rough front TCO.

oxides are applied for a broad variety of applications, e.g. low-E glass, heating of airplane windows, gas sensors, displays, and solar cells [25].

The front TCO in pin type thin-film silicon solar cells plays also an important role in the light trapping. When the front TCO is rough, all subsequently deposited layers and their interfaces replicate this roughness for a major part [26]. Especially the TCO/p and n/back contact interfaces are then effectively scattering the light, see figure 1.2.

Thus, in order to reach a high stable conversion efficiency for amorphous silicon pin solar cells, the front TCO layer has to fulfil a number of requirements:

- high optical transmittance in the wavelength interval from 350-800 nm (350 - 1100 nm for $\mu\text{c-Si}$),
- low lateral electrical resistance,
- appropriate surface roughness for light scattering,
- chemical inertness to reactive hydrogen species, that are created in the PECVD process during deposition of the silicon layers from silane or even silane/ hydrogen mixtures.

Another important application of TCOs for light trapping in thin-film silicon solar cells, which is not treated in this thesis, is an enhanced back reflector consisting of a $\lambda/4$ layer for long wavelength light in combination with a highly reflecting metal at the back contact [27].

Electrical versus Optical Properties

Transparent conductive oxides are degenerately doped wide-gap semiconductors. The ZnO and SnO₂ layers described in this thesis are n-type, so that their conduc-

tivity can be written as

$$\sigma = n\mu_n e \quad (1.1)$$

with n the concentration, μ_n the mobility and e the charge of the electrons. An important figure to characterize a TCO layer is the sheet resistance R_{\square} representing the resistance of a square area in lateral direction:

$$R_{\square} = \frac{\rho}{d} \quad (1.2)$$

with $\rho = 1/\sigma$ the resistivity of the material, and d the film thickness.

Thus, to achieve a low sheet resistance, either the thickness of the TCO, the carrier concentration, or the electron mobility can be increased. While the electron mobility is often limited by the effective mass which is a fundamental material property, thickness and electron concentration have a direct effect on the optical properties of the material. Following Beer's law, the absorption in the TCO increases with increasing layer thickness.

The electron density influences the absorption of the TCO in two ways. The effective optical band gap of a degenerate semiconductor is widened with increasing electron concentration because of the high occupation of the lowest states in the conduction band by electrons excited from the shallow donor states, so that absorption into these conduction band states is forbidden by the Pauli principle. Assuming parabolic bands and a direct band gap, this so-called Burstein-Moss shift [28] amounts to

$$\Delta E_{BM} = \frac{h^2}{8} \left(\frac{3n}{\pi} \right)^{2/3} \left(\frac{1}{m_e^*} + \frac{1}{m_h^*} \right), \quad (1.3)$$

with h Planck's constant, and m_e^* and m_h^* the effective masses of electrons and holes, respectively. Band gap narrowing as a result of many-particle effects and scattering at ionized impurities are calculated in [29]. Experiments have shown however, that band gap widening due to the Moss-Burstein shift is the dominant effect for doped zinc oxide layers [30].

For long wavelength light, the absorption by free carriers limits the transmittance of TCOs with high carrier concentrations. Following the Drude model for free electrons, the absorption and reflection of an electron gas increases, and the transmission decreases for frequencies lower than the plasma frequency

$$\omega_p^2 = \frac{ne^2}{\epsilon_{\infty}\epsilon_0 nm_e^*}, \quad (1.4)$$

with ϵ_{∞} the dielectric constant representing the TCO at high frequencies, and ϵ_0 the dielectric constant of vacuum. This so-called plasma edge for TCOs usually lies in the near-infrared region. Thus, a higher electron density allowing for

a higher conductivity (Formula 1.1) at the same time shifts the plasma edge to a higher frequency (Formula 1.4), resulting in higher free carrier absorption at shorter wavelengths.

Thus, increasing the mobility is the only way to achieve a higher conductivity of the TCO material without sacrificing its long wavelength transmittance. In general, apart from the effective mass resulting from the band structure of the material, the mobility of TCOs is limited by scattering at grain boundaries in the polycrystalline material, at (ionized) impurities, and at phonons. The influence of grain boundary scattering decreases with increasing grain size due to the lower grain boundary density. For the polycrystalline TCOs applied for solar cells, phonon scattering is often negligible compared to (ionized) impurity scattering [31]. Ionized impurity scattering is the dominant effect limiting the conductivity of the best highly doped TCOs reported in literature [31]. To achieve even higher conductivities at the same high transmittance, new TCO materials have to be explored exhibiting a lower effective electron mass and a very high crystalline quality enabling higher intra-grain mobilities [32].

TCO materials

For thin-film solar cells, indium tin oxide (ITO), fluorinated tin oxide ($\text{SnO}_2\text{:F}$), and aluminum, gallium or boron doped zinc oxide (ZnO) are the most widely used TCOs.

Fluorine-doped SnO_2 layers have shown to meet all the above mentioned requirements for the front TCO in thin-film silicon pin solar cells directly upon deposition by Atmospheric Chemical Vapor Deposition (APCVD) at temperatures above 550°C . While all commercially produced pin type thin-film silicon solar cells use $\text{SnO}_2\text{:F}$ as front TCO, the high quality of the Asahi U-type TCO widely used in research laboratories is not readily available for industrial production. There is an urgent need for a high quality TCO at low price which is available on large area substrates with uniform film properties [33].

A promising alternative TCO material to commercial $\text{SnO}_2\text{:F}$, allowing for lower deposition temperature, lower cost, and less environmental impact [31], is zinc oxide. The preparation of rough ZnO films for thin-film silicon solar cells is described below. Undoped single crystalline zinc oxide has a band gap of 3.30 eV [34]. Zinc oxide films can be intrinsically doped when they are sub-stoichiometric, i.e. oxygen deficient. Zinc interstitials [35] and oxygen vacancies [36] are known to form donor states. Extrinsic n-type doping can be achieved e.g. by substituting zinc in the crystal lattice by Ga, Al, or B [25].

Deposited ITO films are extremely flat. For thin-film silicon solar cells, ITO is

thus mainly used as front TCO for nip type solar cells which have been deposited on textured substrates [24]. ITO is more expensive than ZnO and SnO₂, and In is a far less abundant element (0.1 ppm) in the earth's crust compared to Sn (40 ppm) and Zn (132 ppm) [31].

Recently, cadmium oxide (CdO) and cadmium stannate (Cd₂SnO₄) have been presented as TCOs with extremely high electron mobility of 200 cm²/Vs and 80 cm²/Vs, respectively [32]. All currently available TCOs with high conductivity above 10³ Ω⁻¹cm⁻¹ are degenerately n-type doped wide-gap semiconductors. In the past years, many groups have been searching for p-type TCOs [37] such as CuAlO₂ [38], allowing the fabrication of complete transparent electronic devices such as thin-film transistors.

Also nitrogen doped ZnO [39] and undoped ZnO deposited under controlled O₂ flow [40] have shown p-type conductivity. Apart from the relatively low conductivity in the order of 10⁻¹ Ω⁻¹cm⁻¹, the observed p-type conductivity for such materials is often not stable and turns into n-type conductance after exposure to air, probably because of the effective n-type doping of ZnO by hydrogen [41].

Growth of Rough Zinc Oxide Films

Zinc oxide crystallizes in the hexagonal wurtzite structure, see Figure 1.3. The energetically preferred growth orientation is with the c-axis ([002] direction) perpendicular to the substrate. Such films have in principle a smooth surface. Polycrystalline [002] oriented films can have a rough surface if during growth preferential etching of facets other than [002] takes place resulting in crystallite facets forming a rough surface [43], see Figure 1.4.

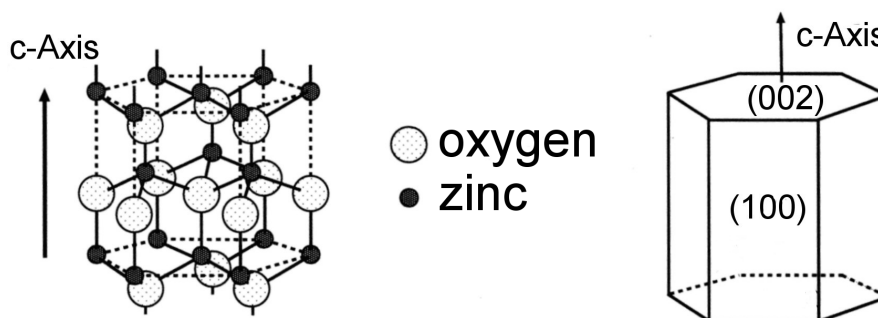


Figure 1.3: The hexagonal wurtzite structure of ZnO, and a schematic drawing visualizing the crystal facets [42].

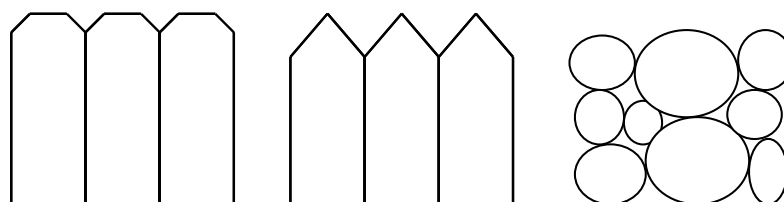


Figure 1.4: Schematic drawing of rough polycrystalline ZnO films (from left to right) with c-axis perpendicular to the substrate, c-axis parallel to the substrate, and with granular structure.

When the c-axis is oriented parallel to the substrate plane, a textured surface can be formed by the facets of the hexagon, like e.g. highly [110] oriented films exhibiting a pyramidal texture [44], see Figure 1.4. A polycrystalline film also exhibits a rough surface when it has a granular crystallite structure. This occurs when adatoms reaching the growing film surface have a low mobility so that crystallite grains oriented in different crystallographic directions are formed (see also Figure 1.4). The rough film surface is then defined by the envelope of the differently sized and shaped crystal grains.

Surface textured ZnO films have been deposited by atmospheric chemical vapor deposition (APCVD) [45], (photo-assisted) metalorganic chemical vapor deposition (MOCVD) [46] also called low pressure CVD (LPCVD) [47], Atomic Layer Deposition (ALD) [48], and sputtering in water atmosphere [49]. Another approach is to sputter flat ZnO films and subsequently texture them by wet-etching [50]. Also the use of textured glass substrates [51] in combination with conformally deposited TCOs may be an interesting alternative to textured TCOs on flat substrates.

1.4 Aim and Outline of this Thesis

Aim of the presented research

In this thesis the front TCO for thin-film silicon solar cells has been studied. In addition to a deeper understanding of the optical processes involved in the light trapping in thin-film solar cells, the development and characterization of TCO materials are the subject of this thesis. Finally, the developed TCOs have been tested in thin-film silicon solar cell structures.

Two approaches have been studied. From the introduction above, it becomes clear that there is an urgent need for TCOs with high quality at low cost and good

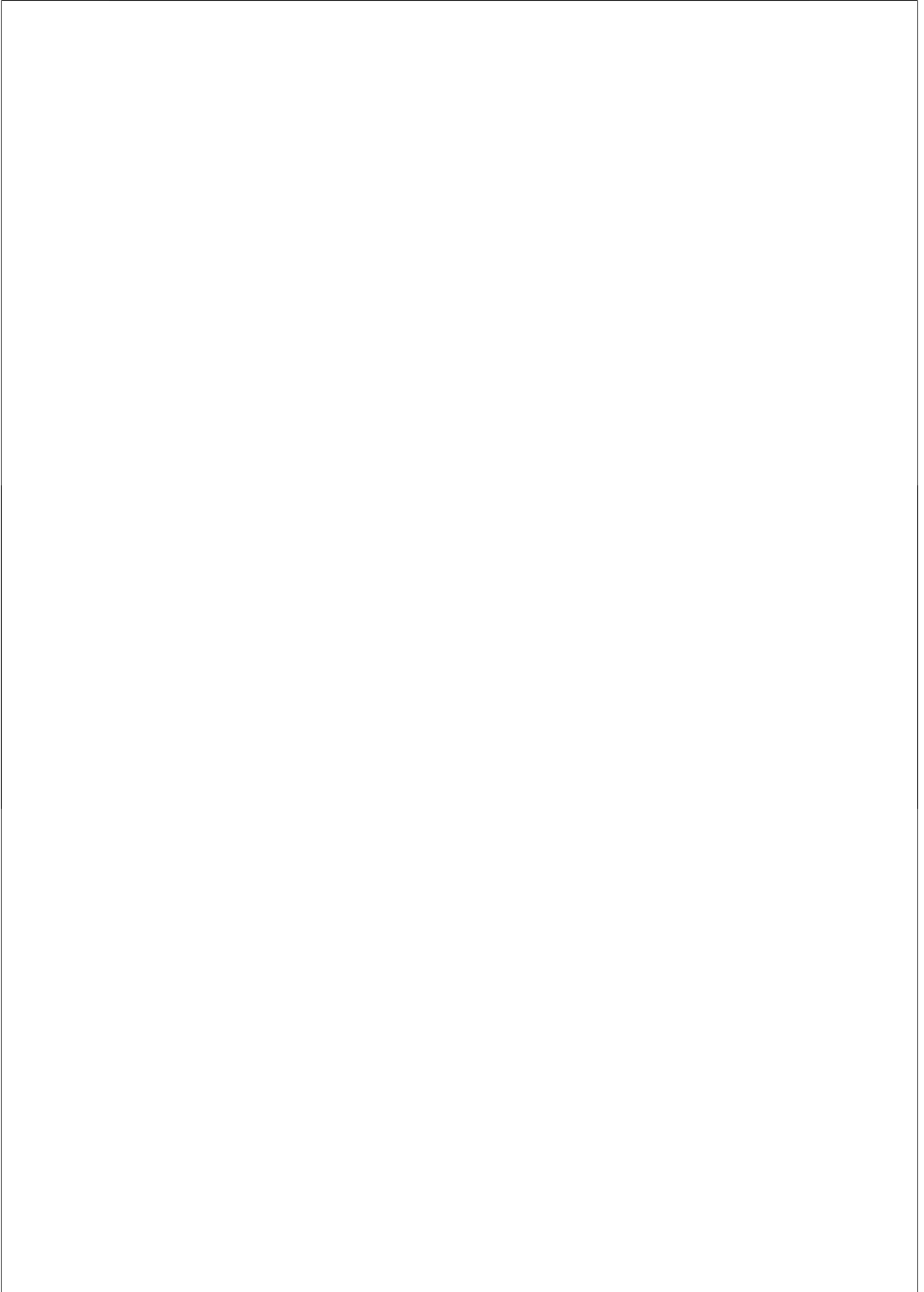
uniformity on large area substrates.

On the one hand, a new technique has been investigated for the deposition of zinc oxide. This material is currently widely applied in the glass industry, but has not yet passed the research and development stage as front TCO for thin-film silicon solar cell production. The Expanding Thermal Plasma Chemical Vapor Deposition technique, which has shown promising results for high-rate deposition of amorphous [52] and microcrystalline silicon [53] as well as silicon nitride layers [54], has for the first time been applied for the deposition of natively textured undoped and aluminum doped zinc oxide layers. Aim was the development of suitable undoped and aluminum doped zinc oxide layers on glass as front electrodes for thin-film silicon solar cells. Emphasis has been laid on the understanding of the layer growth, the resulting film properties, and the factors determining the performance of the solar cells deposited on these TCOs.

The second approach for the front TCO followed here is the APCVD deposition of fluorinated tin oxide. In order to close the gap between the limited quality of the TCOs that are commercially available on large areas, and the best TCOs, which are only available at limited size of 40 x 30 cm² and for a high price, it is important to understand the growth and properties of the high quality TCOs. This understanding may indicate the path to combining cheap deposition on large areas, and the high quality readily obtained on laboratory scale.

Outline of this Thesis

In chapter 2 the experimental techniques for sample preparation and characterization used throughout this thesis are introduced. Details on experimental procedures are further mentioned in the succeeding chapters. In Chapter 3 undoped and aluminum doped zinc oxide layers deposited by Expanding Thermal Plasma CVD under variation of several deposition parameters are presented. Their optoelectronic, structural and morphological properties are related to the deposition process, and compared to two types of reference TCO. A selection of the most promising layers has been implemented in thin-film silicon solar cells. In Chapter 4, the performance of these cells is described and their electrical and light trapping properties are related to the TCO properties. In Chapter 5 fluorinated tin oxide layers deposited by APCVD from three different tin precursors are compared with respect to their optoelectronic and morphological properties. Thin-film silicon solar cells have been deposited on these TCOs, and their performance is related to the TCO properties. Chapter 6 summarizes the main results of this thesis.



2 Experimental

In this chapter the main sample preparation and characterization techniques used for the research described in this thesis are presented. Experimental details and additional techniques that have been used are mentioned in the subsequent chapters.

2.1 Sample Preparation

2.1.1 TCO Fabrication

Expanding Thermal Plasma Chemical Vapor Deposition

Undoped and aluminum doped Zinc Oxide films have been deposited on Corning 1737 F glass substrates ($100 \times 50 \text{ mm}^2$) by Expanding Thermal Plasma Chemical (ETP) Vapor Deposition in an Aixtron AIX 2300 MX pre-production reactor set-up shown in Figure 2.1, at TNO-TPD Eindhoven. The ETP technique is a remote

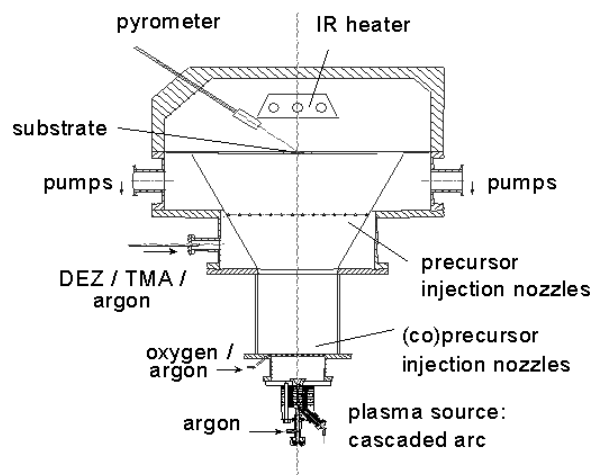


Figure 2.1: Reactor for Expanding Thermal Plasma Chemical Vapor Deposition of undoped and aluminum doped zinc oxide.

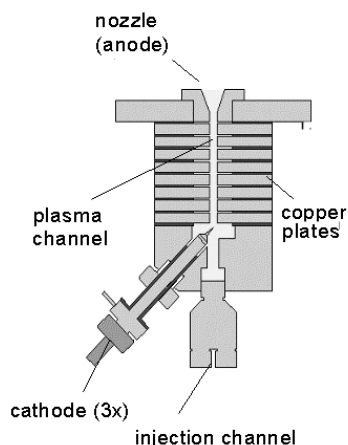


Figure 2.2: Cascaded arc plasma source.

plasma deposition technique. A subatmospheric thermal argon plasma (typically $0.3 - 0.4 \times 10^5$ Pa) is generated in a dc arc discharge. A low-flow cascaded arc (see Figure 2.2) serves as plasma source, consisting of 3 cathodes, a stack of water-cooled circular copper plates insulated from each other by boron nitride rings, and an anode plate. This Argon plasma is subsequently expanded into the low pressure (250 Pa) reactor chamber. Oxygen, diethylzinc (DEZ) and additionally trimethylaluminum (TMA) for doped films are symmetrically injected at different positions into the reactor chamber. No power is coupled in downstream, leading to a low electron temperature (0.2 - 0.3 eV) in the expanding beam [55,56]. The (co-)precursors are ionized via charge exchange with Argon ions and recombine dissociatively with electrons downstream of the plasma source. The mixture of reactive particles flows at subsonic velocities to the substrate where deposition takes place without any significant ion bombardment. The substrate is heated radiatively. The minimum temperature of 150°C is obtained mainly as a result of substrate heating due to the plasma process. The highest temperature available with the present lamp array is 350°C . During the course of the research described here, two different gas injection rings have been used, and two different cascaded arc plasma sources. The DEZ and TMA injection was first realized via tempered bubblers using argon as carrier gas, and later changed to Bronkhorst Hi-Tec Controlled Evaporation and Mixing (CEM) systems.

Atmospheric Pressure Chemical Vapor Deposition

Atmospheric chemical vapor deposition of fluorinated tin oxide ($\text{SnO}_2:\text{F}$) has been performed at TNO-TPD Eindhoven in a modified Watkins-Johnson WJ998 system. This APCVD apparatus has a 21 cm wide conveyor belt which is heated by a 12-zone furnace. The belt transports the substrates through the reactor at an adjustable speed between 0.25 and 25 cm / min. The belt passes an ultrasonic HF bath for continuous belt cleaning with subsequent air drying. The precursors used for deposition can be injected into the deposition chamber via three injector heads which are separated by nitrogen gas curtains. Also at the end of the conveyor belt such nitrogen gas curtains are placed to prevent hazardous gasses from escaping into the laboratory environment. In this study, only the second injector was used for precursor injection, while the other two injectors were fed with nitrogen as to maintain the flow balance. The different precursors used for the deposition of $\text{SnO}_2:\text{F}$ are presented in Chapter 5.

2.1.2 Solar Cell Deposition

Amorphous silicon pin structures have been deposited by plasma enhanced chemical vapor deposition (PECVD), in the first phase of the research at 13.56 MHz in the PASTA system, and at a later stage at 50 MHz in the ASTER system in the Utrecht Solar Energy Laboratory (USEL). Usually, strips of 2 cm width and 10 cm length are used as superstrates, with thermally evaporated silver grid lines for current transport at the p- side of the solar cell in the direction of the long edge of the TCO sample, thus mimicking the series connection in actual solar modules. The silver back contacts, which are at the same time defining the effective solar cell area, are thermally evaporated through a shadowing mask. Most cells have a size of $4 \times 4 \text{ mm}^2$. This cell layout is depicted in Figure 2.3.

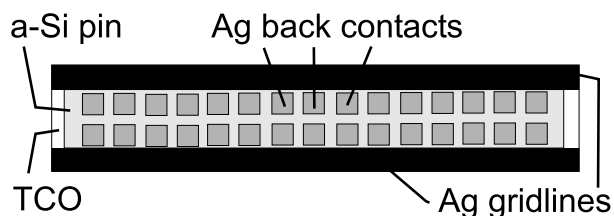


Figure 2.3: Solar cell layout on a 2 cm wide and 10 cm long TCO/ glass strip, sketched from the back contact side of the solar cell.

PASTA System

The PASTA deposition system has been built by Elettrorava, Italy, under licence of MV Systems, USA. It is a versatile multichamber UHV system, in which we have exchanged an RF assembly for a Utrecht University proprietary Hot Wire assembly. The system is used for PECVD deposition as well as Hot-Wire CVD of thin films of silicon and silicon alloys. For PECVD, RF generators operating at 13.56 MHz have been used for the research described in this thesis. The substrate holder can hold samples up to 10 x 10 cm² in size and is heated via radiation sources which are placed outside the vacuum. A detailed description of the system is given in [57].

Standard amorphous silicon pin solar cells deposited in the PASTA system consist of a 10 nm thick wide-gap amorphous silicon carbide (a-SiC) p-layer, a patented p/i buffer [58], a 450 to 500 nm thick intrinsic layer deposited from undiluted silane, and a 20 nm thick amorphous silicon n-layer. The p/i buffer consists of a SiC layer in which the boron content is graded towards zero, and an intrinsic SiC layer where the carbon content is graded to zero. The intrinsic and p- respectively n-doped layers are deposited in separate chambers to avoid cross contamination of the layers and unintentional smearing of the doping profiles. Trimethyl boron (B₃(CH₃)₃, TMB), 2% diluted in H₂, is used as precursor for boron doping of the p-layers, and phosphine (PH₃), 2% diluted in H₂, for n-type doping with phosphorus. The p-layer and the first part of the p/i buffer are deposited at 160°C, the remainder of the layers at 200°C. All layers exhibit device quality properties as defined in [12].

Under optimized deposition conditions regarding issues such as TCO cleaning, deposition chamber cleaning and preconditioning, substrate holder cleaning and grounding, quality of the vacuum and source gases, etc., these solar cells with a simple silver back contact reach initial conversion efficiencies of typically 9.0 to 9.5 % on commercial Asahi U-type SnO₂:F substrates. The properties of these standard solar cells are very uniform over the entire area of the substrate holder with only minor edge effects, so that solar cells in the center area of approximately 8 x 8 cm² of the substrate holder are virtually identical, so that up to 4 strips of TCO with a width of 2 cm can be compared in one solar cell deposition run. This way errors due to run-to-run variations can be excluded, thus increasing the experimental accuracy when comparing different TCOs.

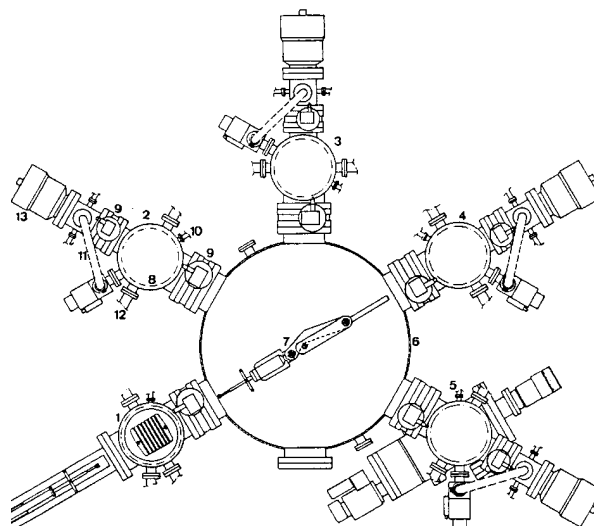


Figure 2.4: The ASTER UHV multichamber plasma deposition system.

ASTER System

Also the ASTER system is a multichamber UHV deposition tool with 4 deposition chambers and one load lock chamber located around a central distribution chamber, see Figure 2.4. Details about the system are given in [59]. The bottom flange of each deposition chamber accompanies either the powered electrode for PECVD processes, or a Hot-Wire assembly. The substrate holder and heater are mounted to the top flange. For this research, a VHF (50 MHz) plasma generator was used. The same types of source gasses are used as for the PASTA system described above. The standard amorphous silicon pin solar cell in the ASTER system consists of only three layers: an 8 nm a-SiC p-layer, a 450 nm thick intrinsic layer deposited from lightly diluted Silane (SiH_4 to H_2 flow ratio of 1:1), and a 20 nm a-Si n-layer. Deposition parameters and layer properties are given in Table 2.1¹. The value E_{04} is the photon energy where the absorption coefficient α of the material is 10^4 which is related to the band gap of amorphous silicon and silicon carbide [11]. All layers are deposited at a substrate temperature of 200°C (heater setting 280°C).

Under optimized deposition conditions, efficiencies between 9.0 % and 9.5%

¹The properties of the doped layers are for thicker samples (between 150 and 250 nm) than the actual layers in the solar cell.

| | (p) a-SiC:H | (i) a-Si:H | (n) a-Si:H |
|---|---------------------|----------------------|---------------------|
| SiH ₄ flow [sccm] | 30 | 30 | 30 |
| H ₂ flow [sccm] | - | 30 | 22.5 |
| TMB (2% H ₂) flow [sccm] | 15 | - | - |
| PH ₃ (2% H ₂) flow [sccm] | - | - | 7.5 |
| CH ₄ flow [sccm] | 40 | - | - |
| pressure [mbar] | 0.15 | 0.15 | 0.15 |
| VHF power [W] | 5 | 5 | 5 |
| E ₀₄ band gap [eV] | 2.05 | 1.91 | 1.89 |
| activation energy [eV] | 0.43 | 0.90 | 0.17 |
| dark conductivity at 300 K [$\Omega^{-1}\text{cm}^{-1}$] | $2.6 \cdot 10^{-6}$ | $2.9 \cdot 10^{-11}$ | $6.2 \cdot 10^{-3}$ |
| photo conductivity at 300 K [$\Omega^{-1}\text{cm}^{-1}$] | $3.0 \cdot 10^{-6}$ | $5.4 \cdot 10^{-5}$ | $8.0 \cdot 10^{-3}$ |
| deposition rate [$\text{\AA}/\text{s}$] | 2.2 | 1.9 | 0.7 |

Table 2.1: Deposition parameters and layer properties of the standard layers used for pin amorphous silicon solar cells in the ASTER system.

have been obtained reproducibly on commercial Asahi U-type TCO. With an enhanced back reflector comprising a 100 nm thick RF magnetron sputtered ZnO:Al layer in combination with a 300 nm thick thermally evaporated silver contact, efficiencies exceeding 10% have been achieved recently. In the ASTER system, the uniformity of a-Si pin solar cells over the 10x10 cm² substrate holder is sufficient to compare 3 TCOs on 2 cm wide glass strips.

2.2 Layer Characterization

2.2.1 UV VIS Spectroscopy

Perkin Elmer

Specular (T_S) and total transmittance (T_T) spectra of the TCO layers on glass substrates have been recorded using a Perkin- Elmer Lambda 2S double beam spectrophotometer equipped with an integrating sphere. This allowed to calculate spectrally resolved haze spectra as the ratio of diffuse (T_D) and total transmittance spectra

$$H_T = \frac{T_D}{T_T} = \frac{T_T - T_S}{T_T}, \quad (2.1)$$

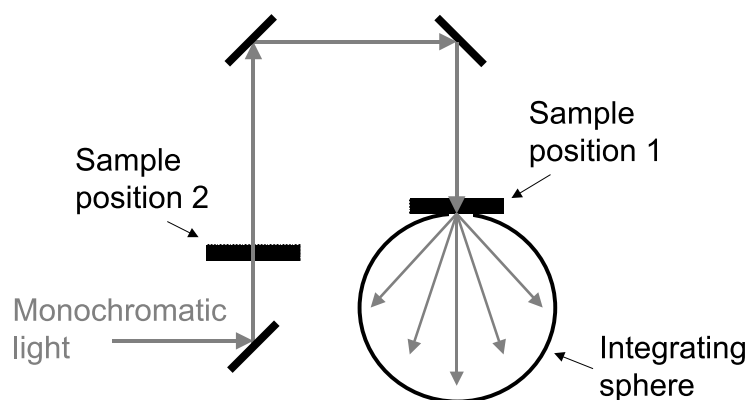


Figure 2.5: The sample compartment of the Perkin Elmer spectrophotometer with integrating sphere, visualizing the sample positions 1 and 2 for total and specular transmittance measurements, respectively.

characterizing the ability of a TCO to scatter the light. The measurements are done with the light incident from the glass side of the sample as it is the case in the actual solar cell structure. The sample compartment of the set-up with the integrating sphere mounted is depicted in Figure 2.5. The total transmittance is measured with the sample mounted in position 1 at the entrance to the integrating sphere, thus allowing all scattered light to enter the sphere and being detected by the detector which is mounted inside the sphere. Measurements with the sphere are made with reference to a 100% signal obtained without a sample mounted. The specular transmittance is measured in position 2, approximately 10 cm of optical path length before the entrance of the integrating sphere, or with an accessory for specular transmittance making use of the detector implemented in the system for measurements without the integrating sphere. Both measurements for specular transmittance practically coincide within less than 0.5%. For the measurement of the total transmittance with the integrating sphere, three sources of errors have been described [60,61]

- Imperfection of the integrating sphere, i.e. deviation from the ideally Lambertian character of the scattering surface.
- light escaping through the edges of the samples due to the wave guiding effect of the TCO / glass stack in the plane of the glass.
- Errors due to the entrance opening of the integrating sphere allowing light to leave the sphere without being detected.

In our experiments, the last mentioned effect seems to be dominating. While errors due to imperfections of the sphere have been calculated to be below 1% [60] and light escaping from highly scattering samples in lateral direction would lead to a decrease of the total transmittance signal [61], we observe an approximately 2% too high total transmittance signal when measuring TCO samples on glass. This is attributed to the fact that during the reference measurement the entrance of the integrating sphere is open so that part of the light can exit the sphere without being detected, while during the actual measurement of the total transmittance of the sample part of this light reaching the entrance opening of the sphere is reflected back from the sample surface into the sphere. Thus, this error will be highest for highly reflecting samples. This has actually been observed for specular a-Si samples on glass which show pronounced interference fringes. Compared to specular measurements, the total transmittance was between 2.5 and 4 % higher, with the largest deviations at the wavelengths corresponding to maxima in the reflectance spectra. Also for a bare flat glass sample which should not scatter at all and thus have a diffuse transmittance of zero, measurements of T_T in position 1 and T_S in position 2 revealed a 2% lower result in the latter case. This T_S is also in agreement with results from the RT mini set-up described below, thus confirming that indeed the measured total transmittance is about 2% too high. As an exact correction for this error depends on the reflectance of the sample, it is a complex procedure practically demanding a specular sample with identical optical constants. Then the measured total transmittance has to be corrected by multiplication with the correction factor CF

$$CF = \frac{T_S}{T_T}. \quad (2.2)$$

As such samples were not available for all TCOs, the haze spectra presented in this thesis have not been corrected, with exception of the spectra in Section 4.2.1, where a correction was essential for the correct quantitative simulation of the measured haze spectra.

RT mini

The RT mini set-up is a compact system for a fast measurement of the specular transmittance and reflectance spectra of a sample at exactly the same position on the sample with a spot size of approximately 1 mm². White light from a halogen lamp is focused on the sample via fiber optics, and the transmitted and reflected spectra are recorded by photodiode arrays. The spectral range for reliable analysis with measurement errors < 1% ranges from 420 nm to 1000 nm. For reflectance

measurements a crystalline silicon wafer is used as reference sample, while the transmittance measurements are calibrated to the 100% signal obtained without a sample.

The measurement and analysis software FIRST! [62] allows the simulation of the measured spectra of a layer or layer stack on a substrate. A variety of models for the dielectric function of the optical media can be applied, ranging from empirical functions given in the data base to models making use of the Kramers-Kronig relations to calculate the real part of the dielectric function from the modelled imaginary part resulting from absorptions by oscillators, by a given density-of-states distribution of a solid, etc.

2.2.2 Angular Resolved Scattering

The angular resolved scattering of TCO samples has been measured with a set-up built at Utrecht University. A HeNe Laser (632.8 nm) beam is directed under normal incidence onto the sample, that is mounted vertically in a dark box with non-reflecting walls. A disc can rotate under the sample holder, which is fixed above the center of the disc. A photodiode is mounted on the circumference of the disc at the same height as the sample. By rotating the disc, and thus the photodiode, to a certain angle with respect to the normal to the substrate, the relative angular resolved scattering (ARS) intensity is measured by the photocurrent generated in the diode. The angular distribution function (ADF) representing the intensity per solid angle of light scattered into a certain solid angle, can be obtained by integrating the ARS intensity over this solid angle.

2.2.3 Raman Spectroscopy

Raman spectroscopy is based on the Raman effect which describes the elastic scattering of light at phonons in a solid. The set-up at Utrecht University used for this research makes use of an Ar laser at an emission wavelength of 514.5 nm. The light scattered from the film surface is spectrally resolved by a triple monochromator, and the resulting spectrum is recorded by a CCD camera. The measurements presented in this thesis have been performed without a polarizing filter in the path of the scattered beam between the sample and the monochromator.

Only the excitation of phonons by the incoming light is observed, resulting in scattered photons with a lower energy than the incoming photons (Stokes peak), in contrast to the anti-Stokes peaks in a Raman spectrum corresponding to annihilation of phonons. While crystalline silicon as a result of the k -conservation has

only one Stokes peak at 520 cm^{-1} for the transverse optical mode, amorphous silicon has a transverse acoustic (TA) peak around 140 cm^{-1} , a longitudinal acoustic peak (LA) around 300 cm^{-1} , a longitudinal optical (LO) shoulder at 400 cm^{-1} , and a transverse optical (TO) peak around 480 cm^{-1} .

2.2.4 Activation Energy of Dark Conductivity

The activation energy of the dark conductivity of thin-film silicon layers has been measured by a set-up built at Utrecht University. The silicon samples on glass are coated with 300 nm thick Ag contacts consisting of two parallel electrodes with a length of 2 cm separated by a distance of 0.5 mm. The samples are placed in a vacuum chamber and heated to 160°C at a rate of $3^\circ\text{C}/\text{min}$. After an annealing time of 45 minutes at 160°C to eliminate water absorbed at the film surface which might induce a surface band bending in the investigated films [63], the sample is cooled down to room temperature at a rate of $0.5^\circ\text{C}/\text{min}$. The conductivity of the samples is measured in intervals of approximately 2 minutes. From the Arrhenius plot of the temperature dependent dark conductivity, the activation energy is deduced by a linear fit to the branch corresponding to the cooling of the sample. If the Arrhenius plot is not linear in the entire measured temperature interval, the line is fitted to the linear part in the vicinity of room temperature.

2.3 Device Characterization

The completed solar cells have been characterized by current- voltage (I-V) measurements in the dark and under simulated sunlight, as well as spectral response measurements.

2.3.1 Solar simulator

The Wacom WX140s dual beam solar simulator has two light sources, a filtered xenon lamp and a halogen lamp. The superposition of these light sources with adequate calibration results in an excellent simulation of the so-called AM 1.5 Global spectrum, which is the solar spectrum of direct and diffused light on earth with bright skies at a geographical width of 45° . The measurements are performed at a cell temperature of 25°C , which is stabilized by ventilation with cooled air while minimizing the exposure of the cell to the light source. The I-V measurement assembly is placed in a dark box equipped with a shutter, and the solar cell sam-

ples can be mounted on an x-y table for automated measurement of the individual cells on one TCO stripe. The measurement is computer controlled and performed actively by a two-probe technique making use of a Keithley 238 source-measure unit.

A solar cell is in principle a diode, so that the I-V characteristics in the dark can be described by the diode equation

$$J = J_0 \left(e^{\frac{-qV}{nkT}} - 1 \right), \quad (2.3)$$

where J is the current density, J_0 the diode saturation current in reverse bias direction, q the electron charge, V the voltage, n the so-called diode ideality factor, k the Boltzmann constant, and T the temperature. Assuming a voltage independent photocurrent J_{ph} , a simple approximation of a photovoltaic solar cell under illumination is obtained:

$$J = -J_{ph} + J_0 \left(e^{\frac{-qV}{nkT}} - 1 \right) \quad (2.4)$$

This model is applicable for diffusion type solar cells with high charge carrier lifetimes and thus long diffusion lengths like in crystalline silicon wafer type cells. A refined model for the amorphous silicon cells treated in this thesis is given in Section 4.3. The solar cell parameters which are commonly used to characterize the I-V curves are explained in the following based on the simplified model. Figure 2.6 visualizes the meaning of the defined parameters. From equation 2.4 the open circuit voltage, defined as the voltage where the current density becomes zero, can be deduced as

$$V_{oc} = \frac{nkT}{q} \ln \left(\frac{J_{ph}}{J_0} \right) \quad (2.5)$$

The so-called short-circuit current J_{sc} is the current at zero voltage, which is obtained when the front and rear contacts of the device are short-circuited under illumination. The maximum power point MPP is the point on the I-V curve where the power generated by the solar cell, given by the product of current and voltage, is maximum. An important parameter characterizing the I-V generation characteristics of a solar cell under illumination is the fill factor FF , representing the ratio of the current density J_{mpp} multiplied with the voltage V_{mpp} at the maximum power point, divided by the short-circuit current density multiplied with the open circuit voltage.

This ratio is visualized in Figure 2.6 by the ratio of the areas of the shaded area to the area of the blank rectangle.

$$FF = \frac{J_{mpp} \cdot V_{mpp}}{J_{sc} \cdot V_{oc}} \quad (2.6)$$

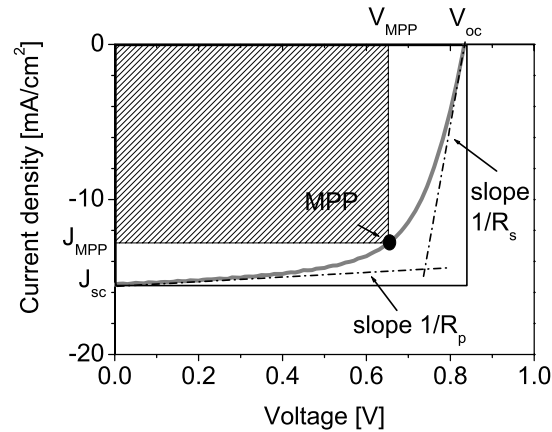


Figure 2.6: A typical I-V curve of a solar cell under illumination, visualizing the solar cell parameters defined in the text.

The inverse of the slopes of the I-V curve at J_{sc} and V_{oc} have the dimension of an (areal) resistance and are denominated R_p and R_s . These values are often related to the actual series and parallel resistances occurring in a solar cell circuit. However, R_p and R_s should not be confused with these resistances, as explained in Section 4.3.

2.3.2 Spectral Response

A custom made spectral response set-up from MACAM (Scotland) has been used for this research. Via a lock-in technique, the additional photocurrent of a solar cell generated upon monochromatic illumination is measured. Usually, the cell is exposed to a stabilized white bias light in order to simulate operation conditions. Also a bias voltage can be applied in order to analyze the origin of current losses. The calibrated result of such a spectral response measurement is plotted for the present research as the external collection efficiency (ECE) spectra, representing the average number of photoexcited charge carriers contributing to the photocurrent generation per incident photon with a given wavelength. Recently the set-up has been upgraded by means of a new calibrated reference photodetector, a highly stable current source, and a new computer software to allow automated batch wise measurements of a solar cell under different bias conditions.

3 Properties of Undoped and Aluminum Doped Zinc Oxide Layers

3.1 Introduction

In this chapter the structural, electronic, and optical properties of undoped zinc oxide (ZnO) and aluminum doped zinc oxide (ZnO:Al) layers deposited by Expanding Thermal Plasma Chemical Vapor Deposition (ETP CVD) are described. The goal has been to develop ZnO and ZnO:Al materials with similar or even better optoelectronic properties as compared to the reference TCOs.

The correlation between deposition parameters and obtained film properties is investigated. Focus is laid on film properties which are relevant for their application as TCO material for thin-film silicon solar cells. As explained in 1.2, a front TCO for amorphous silicon pin solar cells on the one hand has to exhibit a high enough electrical conductivity in lateral direction, on the other hand a high optical transmittance and effective light scattering are demanded. In 3.3 the optoelectronic properties of two types of reference TCOs examined for this research are described. In respectively 3.4 and 3.5 the undoped and aluminum doped zinc oxide layers deposited by ETP CVD under variation of various deposition parameters are presented.

During the course of this research, a number of adjustments have been made to the hardware of the deposition system resulting in changes of film properties obtained under the same deposition conditions. Therefore, the chapter is organized following individual series of layers deposited under constant hardware settings.

3.2 Experimental

Sample Preparation

Textured ZnO and ZnO:Al layers have been deposited on Corning 1737 F glass substrates by ETP CVD at TNO-TPD, Eindhoven, the Netherlands. The glass substrates were cleaned using subsequently acetone, alcohol and water. Various sample series were prepared with varying parameters starting from the *standard* settings used to obtain sub-stoichiometric undoped ZnO layers, see Table 3.1. In

| Parameter | Value |
|-----------------------|-----------|
| substrate temperature | 200 °C |
| diethylzinc flow | 5.15 sccm |
| oxygen flow | 50 sccm |
| Ar flow through arc | 980 sccm |
| arc power | 3.1 kW |
| chamber pressure | 2.5 mbar |

Table 3.1: Standard settings for undoped ZnO layers

the following, only the parameters *layer thickness*, *substrate temperature*, *oxygen flow* and *argon flow through the plasma arc*, which were varied and therefore are deviating from these standard settings, will be mentioned in the text. Table 3.2 summarizes the investigated sample series. During the course of this research, as well the cascaded arc plasma source as the gas injection has been exchanged, which also influenced the film properties. In Table 3.2 the cascaded arc and gas injection used for each sample series is mentioned.

For aluminum doped ZnO:Al layers, trimethylaluminum (TMA) was added to the precursor gas mixture. It has to be mentioned that the recipe for aluminum doped samples is chosen such that stoichiometric layers are obtained which are highly resistive in the absence of TMA. This was done because an increased oxygen flow of 100 sccm compared to the 50 sccm in the standard recipe for undoped layers, allowed better process stability and reproducibility. The parameters varied in the experimental series on ZnO:Al layers are summarized in Table 3.3. The TMA flow for the substrate temperature and Ar flow series was 0.15 sccm.

| Undoped ZnO sample series (results section 3.4) | Range | Unit | cascaded arc | gas injection |
|--|------------|------|-----------------|------------------|
| thickness | 610 -1310 | nm | #1 | #1 |
| substrate temperature 1 | 150 - 350 | °C | #1 | #1 |
| substrate temperature 2 | 150 - 300 | °C | #2 | #1 |
| oxygen flow | 50 - 120 | sccm | #2 | #2 |
| Ar flow through arc | 980 - 1400 | sccm | #2 | #2 |

Table 3.2: Investigated series of undoped ZnO layers

| Doped ZnO:Al sample series (results section 3.5) | Range | Unit | cascaded arc | gas injection |
|---|------------|------|--------------|---------------|
| trimethylaluminum flow | 0 - 0.45 | sccm | #2 | #2 |
| substrate temperature | 150 - 300 | °C | #2 | #1 |
| Ar flow through arc | 840 - 1400 | sccm | #2 | #2 |

Table 3.3: Investigated series of doped ZnO:Al layers

Sample Characterization

Layer thickness and sheet resistance were determined by a stylus profiler and four-probe measurements, respectively. XRD diffractograms were recorded in a Philips X-pert SR 5068 powder diffractometer equipped with a thin-film accessory. A JEOL JSM - 6330 F Field Emission Scanning Electron Microscope (SEM) has been used to visualize the surface and the cross section of the layers. In the same apparatus, EDX analysis of the films was performed. Root mean square roughness of the film surface has been determined by Atomic Force Microscopy (AFM) measurements by a Park Scientific Instruments Autoprobe 100 μm tool. Total and specular transmittance of the films were measured to obtain information about absorption and haze of the films. In order to get information on the spatial distribution of the scattered light in the most relevant regime of wavelengths longer than 600 nm, angular resolved scattering measurements were performed with a HeNe laser (632.8 nm).

3.3 Reference TCOs

In this section the optoelectronic properties of the two TCOs examined as reference material are described: Asahi U-type TCO from the Asahi Glass Company (Japan) [64], which is the best commercially available fluorinated tin oxide ($\text{SnO}_2\text{:F}$) [65] widely used in research laboratories for highly efficient thin-film silicon solar cells [47,66], and texture etched magnetron sputtered ZnO:Al developed [50] and successfully applied especially in microcrystalline silicon solar cells [66] at Forschungszentrum Jülich (FZJ), Germany. Two batches of Asahi U-type $\text{SnO}_2\text{:F}$ were used during this research, representing the reference TCO in the Utrecht Solar Energy Laboratory (USEL) during different periods: First a 980 nm thick TCO (type I) with a sheet resistance of $6 \Omega/\square$, and later a 780 nm thick one (type II) with a sheet resistance of $11 \Omega/\square$. It has to be noted that also

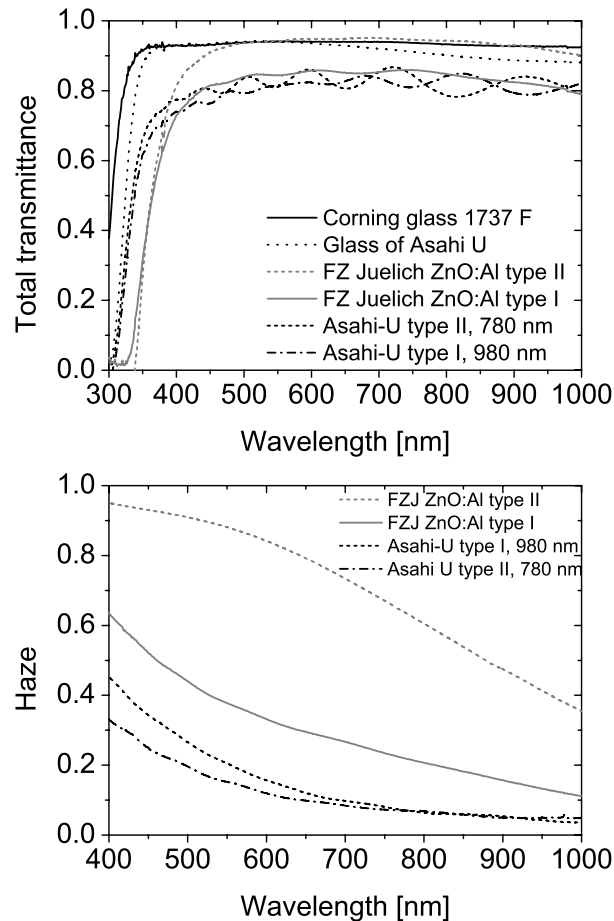


Figure 3.1: Total transmittance(top) and haze (bottom) spectra of the examined reference TCOs. In the transmittance plot, also the glass substrates are included.

within one batch of TCO variations in thickness and haze occur, so that small differences between reference TCOs used in the solar cells (see chapter 4) could not be avoided. Also from FZJ two types of ZnO:Al, deposited on Corning 1737F glass, were supplied. Type I is the TCO that we used for comparison during the research on ETP zinc oxide, type II shows the optimized ZnO:Al currently used as standard TCO at FZJ for microcrystalline silicon based solar cells.

In Figure 3.1 the total transmittance of the TCOs including the substrates and of the bare substrates, as well as the corresponding haze spectra are shown. In the upper graph, it can be seen that for wavelengths longer than 600 nm the Corn-

ing 1737 F glass substrate has a slightly higher transmittance than the glass substrate used by the Asahi company. This is probably due to parasitic absorption by metallic impurities in the Asahi glass. Both substrates, however, have a far higher transmittance than the substrates commonly used in PV industry [33].

The 980 nm thick Asahi U-type TCO has a slightly lower transmittance in the blue part of the spectrum than the 780 nm thick Asahi TCO. The main difference with respect to the thinner layer is however the less pronounced appearance of interference fringes. In addition to this, the fringes of the 980 nm thick TCO are not periodic and disappear in the wavelength range between 500 nm and 650 nm. For the ZnO:Al samples from FZJ no fringes are observed in the transmittance spectrum. The disappearance of the fringes is explained by a loss of coherence of the light while travelling multiple paths through the TCO film due to reflectance at the TCO/glass and TCO/air interfaces. At each reflectance at the TCO/air interface, a certain chance of light scattering exists, which leads to a loss of (spatial) coherence. This chance is in first approximation equal to the measured haze, which explains the disappearance of fringes with higher haze. Wallinga [26] showed that a mere superposition of transmittance spectra of films with different thickness, with the thickness distribution related to the roughness of the films, leads to a partial disappearance of interference fringes as observed for the 980 nm thick Asahi U-type TCO. While the type I ZnO:Al exhibits comparable transmittance to the two Asahi substrates, the type II ZnO:Al shows a high transmittance indicating virtually no absorption losses in the ZnO:Al layer in the wavelength range between 500 nm and 900 nm.

As can be seen from the lower graph in Figure 3.1, the thicker Asahi-U type-I TCO has also a higher haze (16% at 600 nm) than the 780 nm type II sample (12%). The ZnO:Al samples from FZJ exhibit even higher haze, 33% at 600 nm for the type I, and 84% for the type II sample, indicating that for the latter the majority of visible light is scattered already after one path through the TCO/air interface. More importantly for solar cells with microcrystalline silicon absorber layers, near infrared light is still efficiently scattered by this TCO. As the goal of the present research was the development of TCOs for amorphous silicon pin solar cells, the main focus is laid on comparison with the Asahi U-type TCOs and the type I ZnO:Al from FZJ.

3.4 Undoped Zinc Oxide

In this section the properties of undoped ZnO samples deposited by ETP CVD are presented in comparison to the reference TCOs presented in section 3.3. The type

of Asahi samples (type I: 980 nm thick or type II: 780 nm thick) appearing in the following transmittance and haze spectra are of the type that was at the time of layer fabrication used as standard TCO in the Utrecht Solar Energy Laboratory. They were also used as reference substrates when the ZnO layers were tested in solar cells, see chapter 4.

Many process parameters have been varied for the deposition of ZnO layers by ETP CVD with the goal to achieve a front TCO material with comparable optoelectronic properties to the above mentioned reference TCOs.

3.4.1 Layer Thickness

Starting from the standard settings for conductive, undoped ZnO which had resulted from preliminary tests [67,68], a layer thickness series has been deposited by varying the deposition time. Figure 3.2 shows the haze spectra of three ZnO layers deposited by ETP CVD with different thickness, compared to two reference TCOs.

The fringes in the spectra, seen most clearly for the 980 nm sample, are artifacts due to the measurement procedure: The haze values are calculated as the difference of the total transmittance and its specular part, divided by the total transmittance. Both measured spectra show interference fringes. As they are not taken at the same sample position in the spectrophotometer setup, and thus not exactly at the same spot on the sample, non-uniformities in deposition may cause

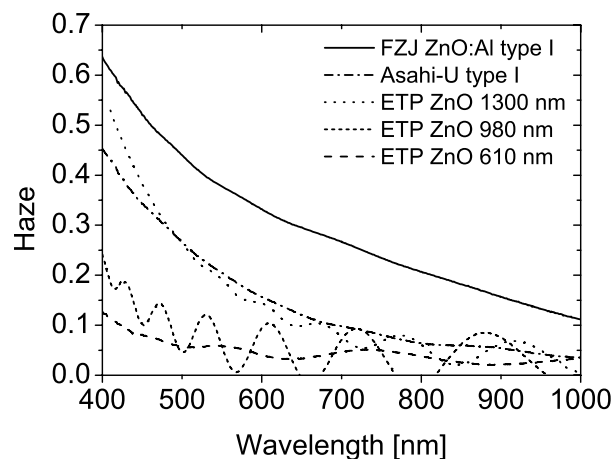


Figure 3.2: Haze spectra in transmittance for ZnO layers of different thickness and two reference TCOs

small variations in layer thickness between the probed spots for total and specular transmittance. This leads to slightly different positions of the fringes in the corresponding transmittance spectra, which can introduce considerable fringes in the haze spectra.

With increasing layer thickness the haze increases over the whole investigated wavelength region, indicating more efficient light scattering at the ZnO/air interface due to a larger surface roughness of the film. Thus, the ETP CVD method indeed allows to grow natively textured ZnO. An evolution of film roughness during growth is observed. At around 1300 nm film thickness the haze value at a wavelength of 600 nm reaches 14 %, a value close to the Asahi U-type TCO used as reference material here. Therefore, in the succeeding series of experiments, the layer thickness was aimed at 1100 to 1300 nm. At this thickness, also reasonable sheet resistances in the order of $10 \Omega/\square$ were obtained for the ZnO deposited under these standard deposition parameters, making it already a TCO material comparable to the Asahi U-type reference.

3.4.2 Substrate Temperature

Two deposition temperature series of undoped ZnO samples are presented here. In series 2 a new cascaded arc was mounted (#2) to the system, leading to a two to three times lower deposition rate with respect to series 1, see Figure 3.3. SEM micrographs of the cross section and surface of these films are shown in Figures 3.4 and 3.8, for series 1 and 2, respectively.

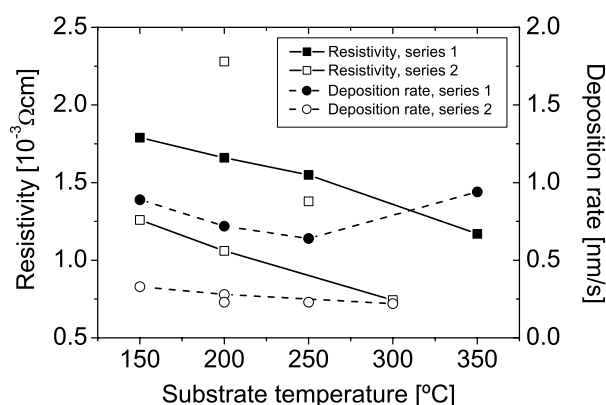


Figure 3.3: Resistivity and deposition rate of undoped ZnO layers as function of the deposition temperature

Temperature Series 1

From Figure 3.4 it can be seen that up to a substrate temperature of 250°C the polycrystalline layers grow in columnar structure with a transition to granular growth at higher substrate temperature. Granular growth dominates for the film deposited at 350°C. In Figure 3.4 the surface of the layers with columnar structure appears to be textured. This texture is formed by the pyramidal tips of the columns. This sharp texture is also observed for the film grown at 150°C (see [69], not shown here). However, the feature size decreases considerably with decreasing deposition temperature.

At higher temperature, with the transition from columnar to granular growth, also the surface structure changes to more rounded features. It has to be noted that the layer deposited at 250°C is slightly thinner than the other layers. This can explain why the feature size is smaller than for the 200°C sample and comparable to the layer deposited at 150°C. The sample deposited at the highest temperature of 350°C exhibits the roughest surface with features up to 1 μm in size. Also in AFM scans an increase in feature size and root mean square roughness is found, from 0.2 μm to 1 μm , and from 34 nm via 48 nm to 64 nm, respectively, with the substrate temperature increasing from 200°C via 250°C to 350°C. The values for the root mean square (rms) roughness calculated from AFM area and line scans generally exhibit a considerable variation depending on the size of the scanned surface area, the scanning direction, and the spot on the sample where the measurement is performed. This is due to the roughness of the sheet glass substrates on a lateral scale of several micrometers up to millimeters, possible inhomogeneity in the thickness of the deposited films, and the statistical effect that with larger scanning areas fewer roughness features are only partially situated within this area. The values presented here have been deduced as the averaged result from area scans of 5 x 5 μm^2 and 15 x 15 μm^2 , which are also in good agreement with the averaged results obtained from several line scans of 5 and 15 μm length.

XRD diffractograms (Figure 3.5) show that the columns observed in the SEM micrographs correspond to hexagonal ZnO crystallites oriented with the [002] direction (*c*-axis) perpendicular to the substrate plane. All layers deposited between 200 and 350°C show predominantly this orientation. However, in contrast to the layers deposited up to 250°C which exclusively show the first and second order of the [002] diffraction peak, the 350°C sample exhibits additional peaks corresponding to mainly [101], [102], and [103] faces with their growth direction oriented perpendicular to the substrate, and minor contributions from [100], [110], and [112]. This is in accordance with the observed transition from columnar to granular growth. A detailed analysis of the [002] diffraction (lower graph in Fig-

Temperature series 1, cascaded arc 1, gas injection 1

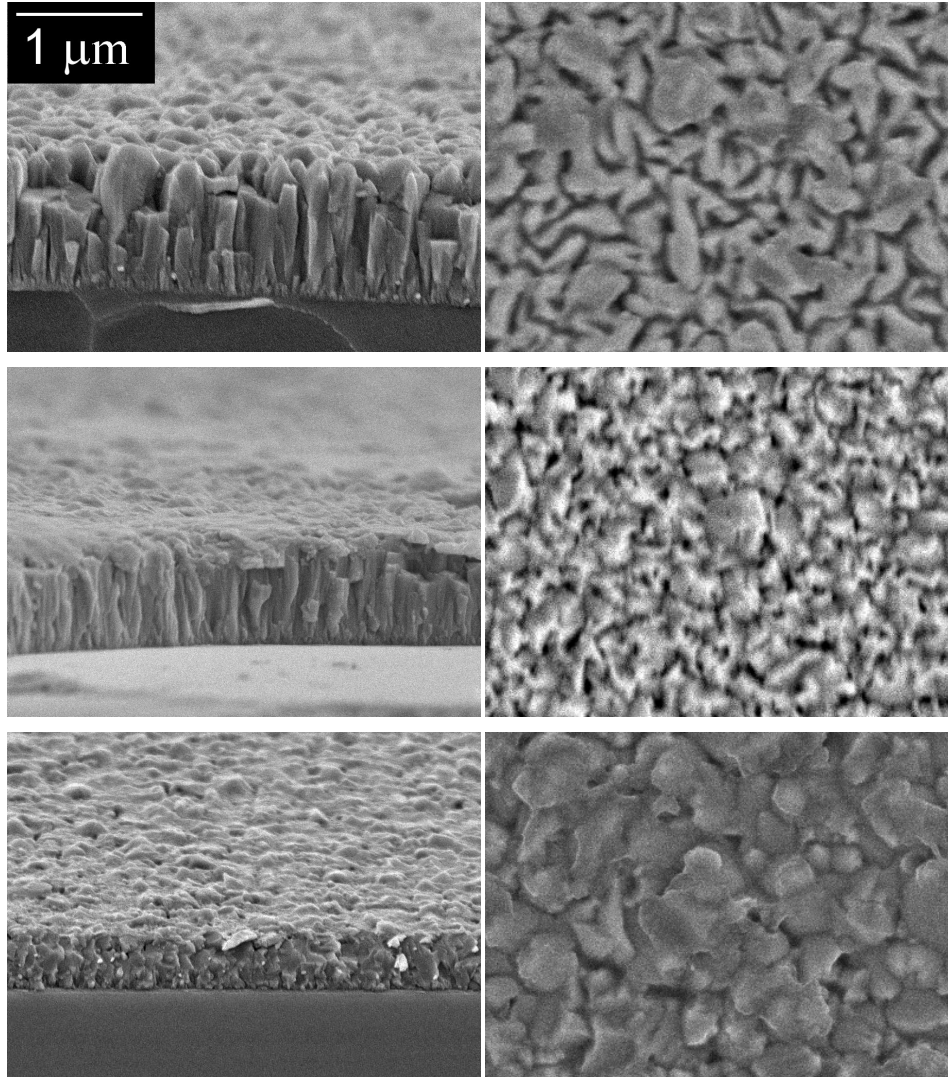


Figure 3.4: Cross sectional and surface SEM micrographs of series 1 of undoped ZnO layers deposited at 200°C, 250°C, and 350°C (from top to bottom).

ure 3.5) reveals an approximately 50 % narrower peak for the 350°C sample than for the other layers. From the full width at half maximum (FWHM) B of the XRD signal the size of the crystallites in the direction of growth t can be calculated via

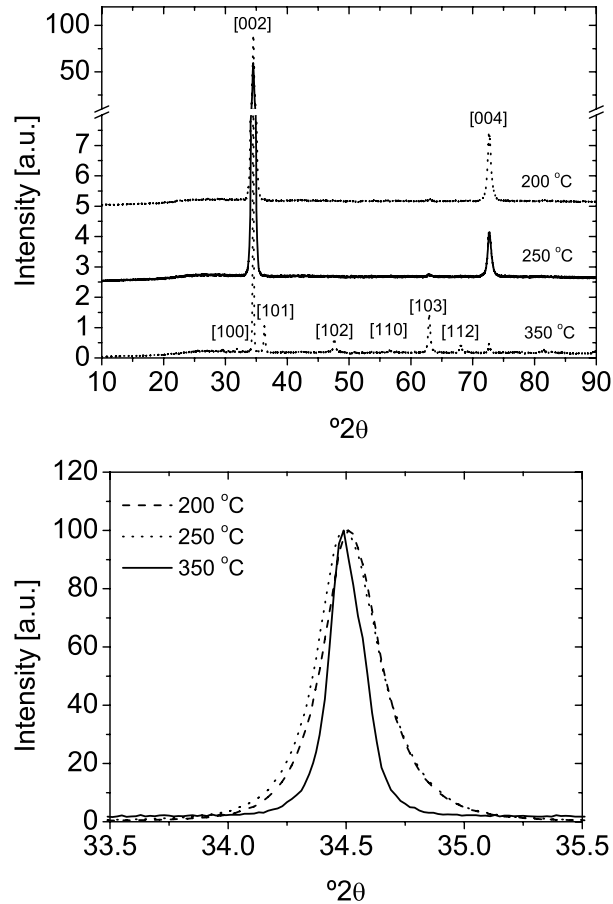


Figure 3.5: XRD diffractograms of ZnO layers deposited at different substrate temperatures (series 1). The lower Figure shows an enlargement of the normalized [002] peak.

the Scherrer formula [70]

$$t = \frac{0.9\lambda}{B \cos\theta}, \quad (3.1)$$

where λ is the wavelength of the X-ray (here 0.54 \AA for Cu $K\alpha$). From the above XRD spectra, one would calculate crystallite sizes in the order of only 50 to 100 nm, while from the SEM micrographs the crystallite columns appear continuous from the substrate to the film surface, which is more than $1 \mu\text{m}$. For the granular sample, the crystallite size in vertical direction is smaller, between 200 and 500

nm. The virtual discrepancy between SEM and XRD analysis is explained by the fact that there is a distribution of crystallites with different sizes and forms present in the film. The XRD peak is broadened by all crystallites present in the film that have a smaller size in vertical direction. This can be for example tiny crystallites in the nucleation part of the film. Also the fact that what appears in SEM as one crystallite column is often composed of several grains with identical orientation, separated only by a stacking fault, may lead to a broadening of the XRD peak. These crystallites composing the columns, however, are not small enough to explain the sizes determined by the Scherrer formula. This can clearly be seen in chapter 4, where cross sectional transmission electron micrographs (TEM) of solar cells on top of ZnO layers are presented.

For the columnar samples, the width of the XRD peak therefore seems to be most significantly broadened by the small crystallites growing in the initial stage of the film deposition. In the granular growth regime, less of these small crystallites are present. The granular growth rather allows more nucleated crystallites to grow as large round grains with different orientations, resulting in narrower XRD diffraction peaks. From this discussion it becomes clear that size estimations of crystallites from XRD diffractograms are heavily influenced by small crystallites from the initial growth phase. The size of the columns and grains forming the bulk of the layer and determining the shape of the film surface are only accessible from TEM, and to a certain extent by SEM.

A similar transition in growth mechanism from columnar to granular growth has been reported for ZnO layers deposited by sputtering in the presence of water vapor [49,43]. Also for CVD layers deposited in the presence of water vapor transitions between different preferential orientations [44] and towards mixed-phase materials corresponding to granular growth [43,44,71] have been observed. The origin of the textured surface in the columnar growth regime is explained by preferential growth in the crystal direction with lowest surface energy due to high surface mobility of adatoms during growth. This leads to an enhanced growth of these columns with crystal facets forming the surface texture. Also etching of the growing surface is reported to result in such facets. The granular growth regime is attributed to a low surface mobility of adatoms during growth. The observed transition to granular growth is however in contrast to the higher mobility expected at higher substrate temperature. The presence of OH species bonded to the surface may play a role here. This has earlier been reported to result in a lowering of the surface mobility [43].

Although some insight has been gained in the species present in the gas phase during ZnO deposition by ETP CVD [72], their role in the growth of the polycrystalline film needs further study. It is clear however that water is formed during the

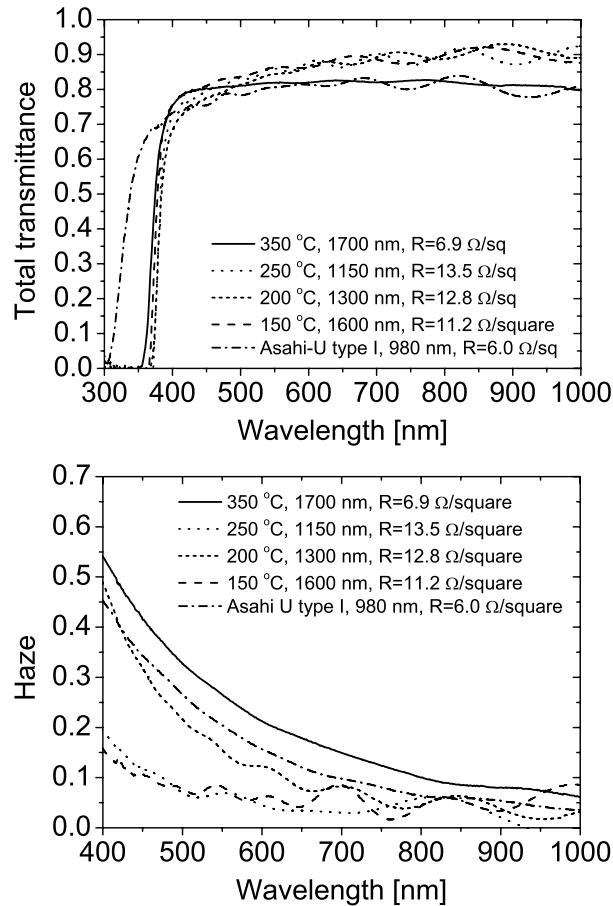


Figure 3.6: Total transmittance(top) and haze (bottom) spectra of series 1 of undoped ZnO layers deposited at different substrate temperatures.

dissociation of Diethylzinc in the plasma in the presence of oxygen, so that OH species may play a similar role here as reported for sputtered films [43].

Figure 3.6 shows the corresponding transmittance and haze spectra of these ZnO films. In the legend of the graphs the sheet resistance and thickness of the layers are given.

These ZnO films with the adequate thickness necessary for sufficient sheet conductivity for application as front TCO in solar cells show still high transmittance (> 80 %) at wavelengths above 400 nm, nearly independent of the substrate temperature during deposition. Only the sample deposited at the highest temperature

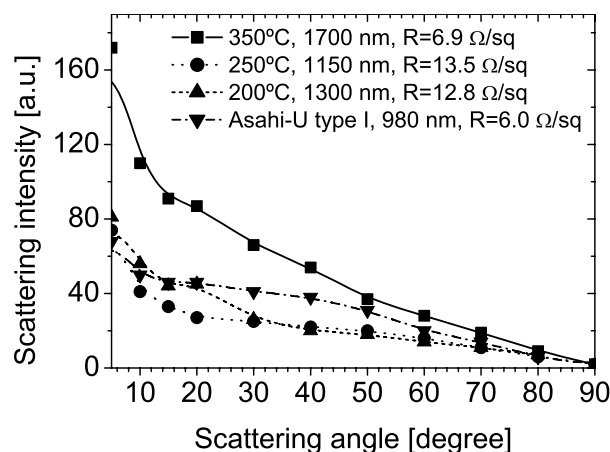


Figure 3.7: Angular resolved scattering at 632.8 nm of series 1 of undoped ZnO layers deposited at different substrate temperatures.

(350°C) has somewhat lower transmittance, although still above 80 % and comparable to Asahi U-type TCO. This sample also exhibits a slightly wider optical band gap. Both observations can be explained by a larger free carrier concentration. The higher absorption at longer wavelength is due to absorption of light by the free carriers, while the shift in optical bandgap of degenerate semiconductors is well known as Moss-Burstein-shift as explained in 1.3. This conclusion is also in accordance with the resistivity of the samples, see Figure 3.3. These sub-stoichiometric layers all show low electrical resistivity around $1 \times 10^{-3} \Omega\text{cm}$ due to oxygen vacancies and interstitial zinc [35,36]. Apparently, the crystallite quality is high enough to allow these sites to be indeed active as dopants, as well as to enable a sufficiently high mobility of the resulting free charge carriers. The resistivity of the films decreases slightly with increasing deposition temperature, which can be ascribed to both, a higher charge carrier concentration, as well as a higher effective charge carrier mobility. Such a higher mobility is observed in polycrystalline material with larger grains in lateral direction because charge carriers are less exposed to grain boundary scattering.

The observed trend in surface roughness with increasing substrate temperature and layer thickness is also found in the haze spectra, see the lower graph in Figure 3.6. The 350°C sample exhibits the highest haze values of the ZnO samples for all wavelengths measured (400 - 1000 nm), even higher than Asahi U-type $\text{SnO}_2:\text{F}$. The haze of the 200°C sample is somewhat lower, and the 150°C and 250°C samples exhibiting lower surface roughness and smaller feature size show the smallest

haze.

The angular resolved scattering intensity (ARS) at a wavelength of 632.8 nm plotted in Figure 3.7 shows the same trend as the haze spectra. ZnO layers deposited at higher substrate temperature scatter more light into all directions. Also here, the 350°C sample shows higher values than the Asahi U-type TCO. A special feature of the Asahi-U TCO (type I) is a shoulder in the scatter curve between 15 and 50 degrees, representing a very uniform spatial distribution of the scattered light, in contrast to the ZnO samples where most of the light is scattered under smaller angles with a strongly decaying function towards larger angles. No qualitative difference between the scatter curves for granular ZnO deposited at 350°C and the columnar ZnO obtained between 150°C and 250°C are observed.

Temperature Series 2

Similar results have been obtained for the temperature series 2. As seen in Figure 3.8, at higher substrate temperature a transition from columnar to granular growth takes place at 300°C and a rough surface is obtained due to the pyramidal and granular shape of the different grains, respectively. The corresponding rms roughness as determined by AFM increases from 36 to 63 nm for films deposited between 150°C and 300°C, very similar to the first series. XRD analysis showed that the layers are all preferentially oriented with the c-axis orthogonal to the substrate. However, in this series all layers except for the one deposited at 200°C show also additional crystallite orientations, see Figure 3.9. It is striking that the [101] and [103] orientations most prominently characterizing the transition to granular growth in series 1, are in series 2 already occurring at a lower substrate temperature of 250°C.

Faj [44] reports on the necessity of low pressures around 0.5 mbar in LPCVD to avoid gas phase reactions and attain high crystalline quality. The occurrence of differently oriented grains at higher pressures is ascribed to unwanted gas phase reactions. It is speculated that here the exchanged plasma arc in series 2 has a comparable effect.

The optical properties of the layers in comparison to Asahi U-type TCO are shown in Figure 3.10. Again, all films exhibit high transmittance above 80 % for visible light and in the near infrared. Note the slightly higher transmittance at short wavelengths for the layer deposited at 300°C as compared to the ZnO layers deposited at lower substrate temperature. The optical haze, as in series 1, increases with increasing deposition temperature. This trend is more clearly visible than in series 1 as the thickness variation between the four ZnO layers from series 2 is much smaller. All ZnO layers from this series show higher haze than the Asahi

Temperature series 2, cascaded arc 2, gas injection 1

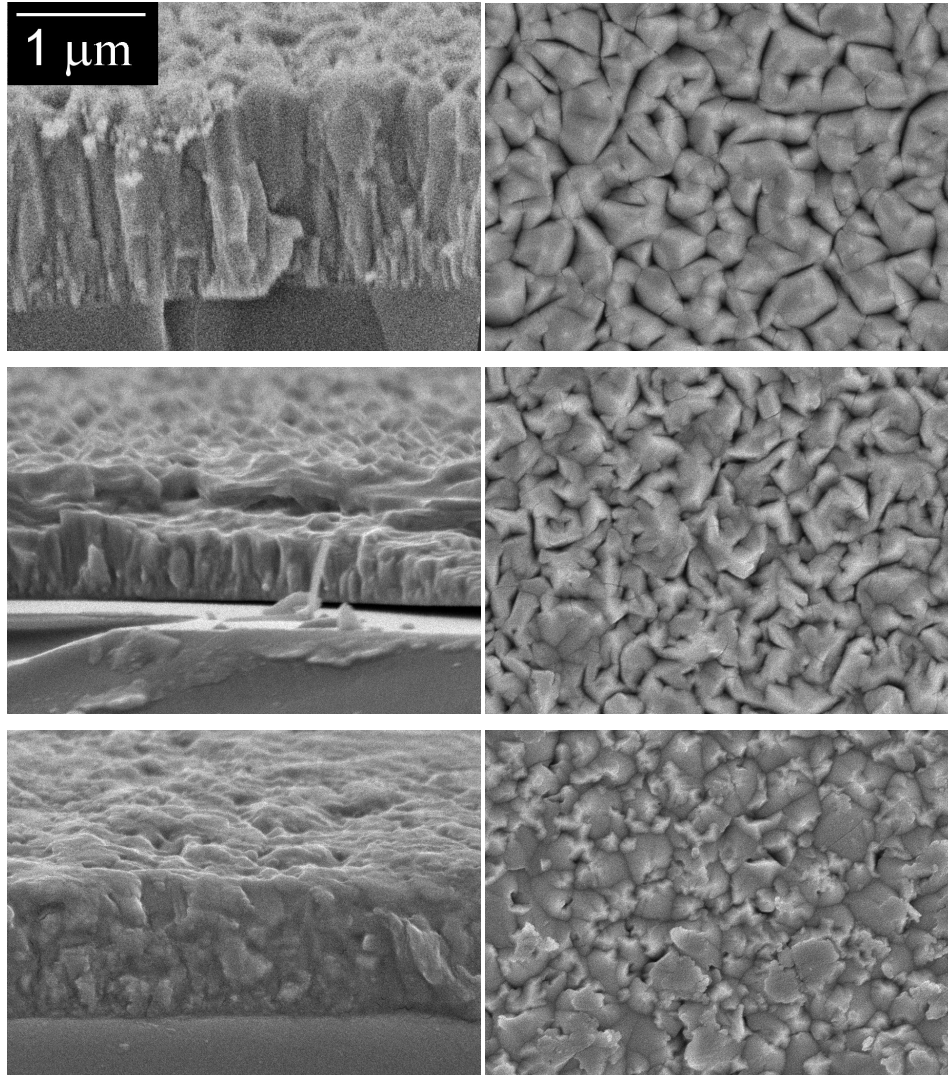


Figure 3.8: Cross sectional and surface SEM micrographs of series 2 of undoped ZnO layers deposited at 150°C, 200°C, and 300°C (from top to bottom).

U-type SnO₂:F.

The variations in deposition rate with increasing substrate temperature in Figure 3.3 are within the run-to-run deviations so that no significant trend can be deduced. The points excluded from the lines connecting the data points in the

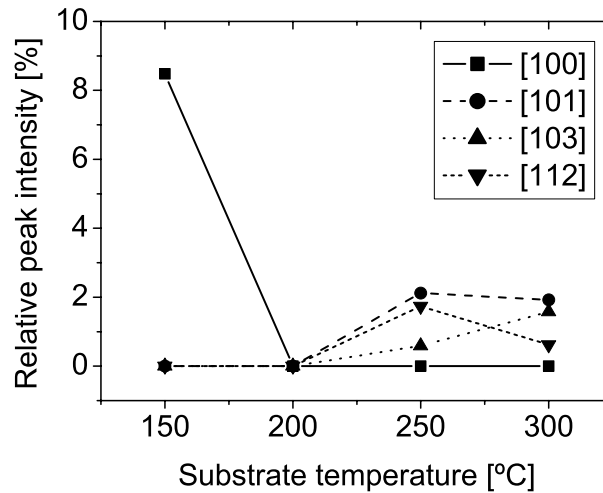


Figure 3.9: XRD peak intensities relative to the [002] peak for different crystallite orientations as function of the substrate temperature (for series 2).

plot are from layers deposited from an aged batch of diethylzinc. As can be seen for the two samples deposited at 200°C, the resistivity then increases by more than a factor of 2, while the deposition rate is not significantly affected. Certainly no trend of increasing deposition rate with increasing substrate temperature is seen here, indicating that the deposition rate limiting processes are occurring in the gas phase, and not at the growing surface. Obviously, the resistivity of the layers deposited in series 2 is around 50% lower than for series 1. This is considered only a small variation here and can be attributed to the different growth conditions as a result of the exchanged plasma arc. Thus, in series 2 layers with slightly better electrical properties and comparable optical properties as in series 1 are obtained. As a result of the exchange of the cascaded arc plasma source, the structural properties of the layers as deduced from XRD have slightly changed which was unnoticed from the SEM analysis (Figures 3.4 and 3.8).

Summary

All ZnO layers deposited in these two series have optoelectronic properties comparable to Asahi U-type TCO. With increasing substrate temperature, the surface roughness increases, and a transition from columnar to granular growth is observed. The layers become slightly more conductive, and suffer from slightly higher free carrier absorption. The influence of this on the solar cell properties is

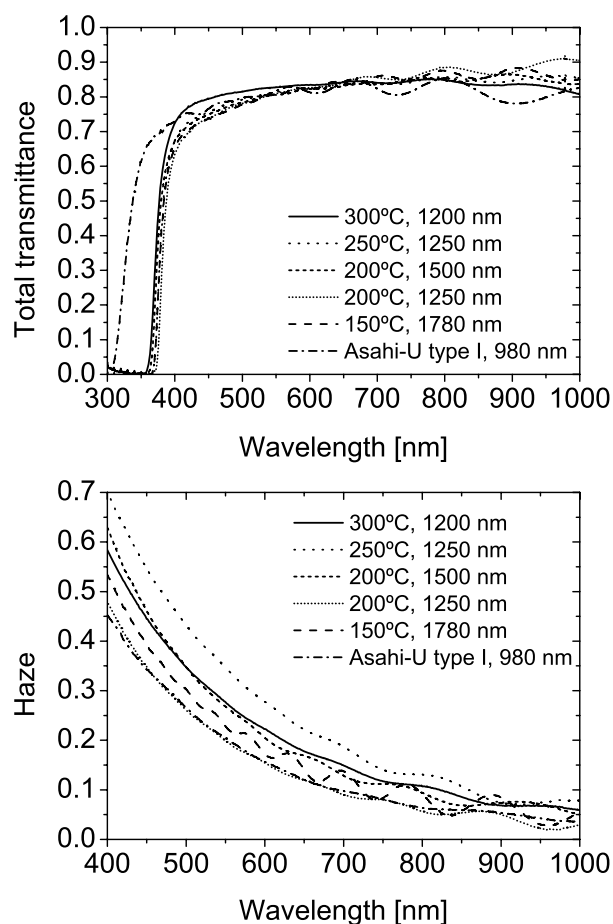


Figure 3.10: Total transmittance(top) and haze (bottom) spectra of series 2 of undoped ZnO layers deposited at different substrate temperatures.

described in chapter 4.

3.4.3 Oxygen Flow

Variation of the oxygen flow injected into the reaction chamber during deposition is expected to result directly in a variation of the stoichiometry of the films. The higher the oxygen flow, the higher becomes the expected oxygen/zinc ratio, and thus the lower the expected density of oxygen vacancies and interstitial zinc atoms

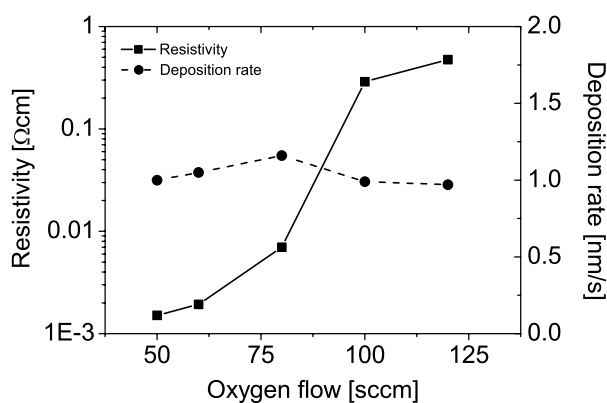


Figure 3.11: Resistivity and deposition rate of undoped ZnO layers as function of the oxygen precursor flow

which are responsible for the n-type conductivity of sub stoichiometric undoped ZnO films [36,35].

As a result of this the resistivity of the films increases by more than two orders of magnitude when the oxygen precursor flow is increased from 50 sccm to 125 sccm (Figure 3.11).

We also observed an increase in resistivity by one to two orders of magnitude when annealing substoichiometric undoped ZnO samples in ambient air at temperatures well below their deposition temperature. Heating in nitrogen ambient up to the deposition temperature of the ZnO films did not change their resistivity. This is in agreement with the findings of Sang *et al.* [46] who found for MOCVD grown undoped zinc oxide an increase in resistivity by two orders of magnitude upon annealing in air at room temperature. They follow the argumentation by Major *et al.* [73] and Caporaletti [74] that oxygen is chemisorbed at the grain boundaries of the polycrystalline ZnO leading to an increase in the potential barrier height and trap density at the grain boundaries. This reduces both, the charge carrier density and their effective mobility, which directly results in a lower macroscopic conductivity of the material. It is stated here that also filling of oxygen vacancies by post deposition oxidation [31] can explain the lower conductivity as a result of a decreasing charge carrier concentration. While Major *et al.* observed a large decrease in carrier mobility upon post oxidation, it has to be taken into account that their films had small crystallite sizes of only 20 to 40 nm. In such layers, the grain boundary effects are expected to be far more pronounced than in our films with 10 to 50 times larger grains, so that the macroscopic electrical properties approach

Oxygen flow series, cascaded arc 2, gas injection 2

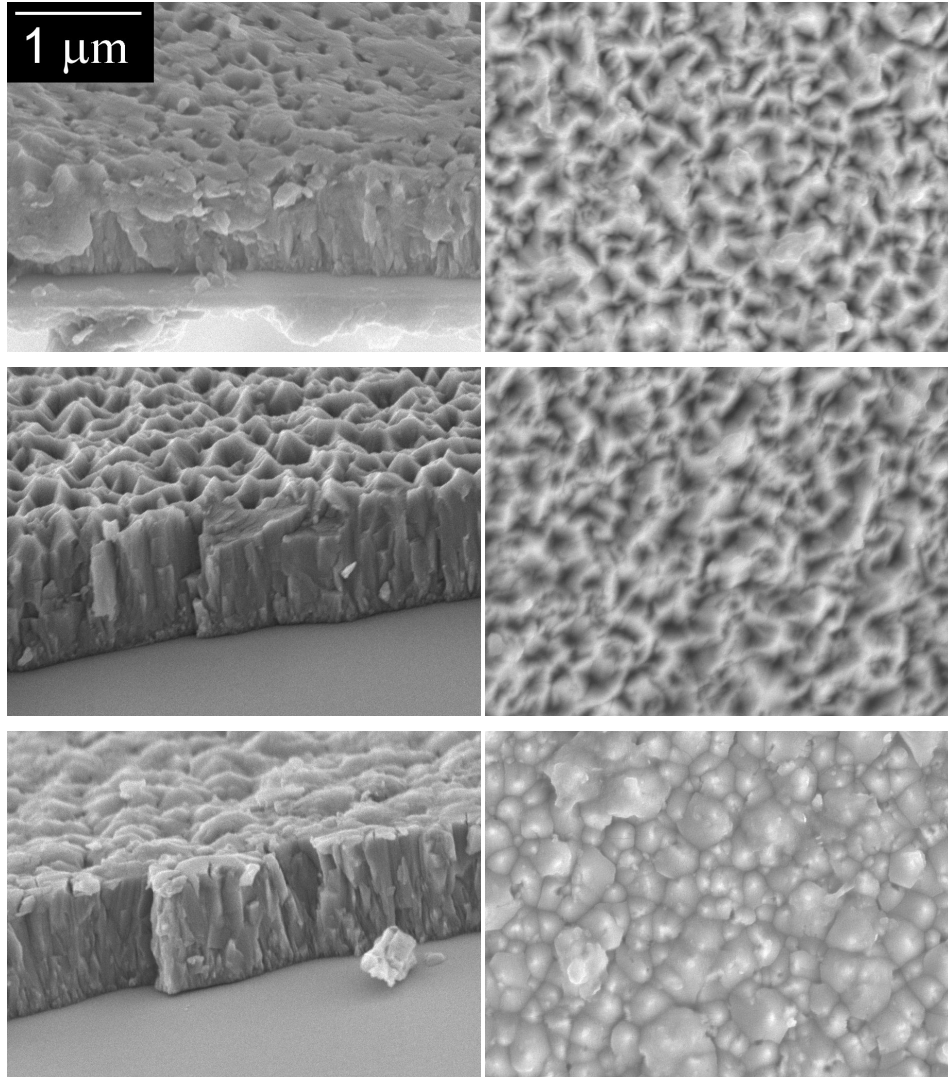


Figure 3.12: Cross sectional and surface SEM micrographs of undoped ZnO layers deposited with oxygen flows of 60 sccm, 80 sccm, and 100 sccm (from top to bottom).

the properties of the bulk material [75].

The deposition rate in Figure 3.11 is constant within the run-to-run repro-

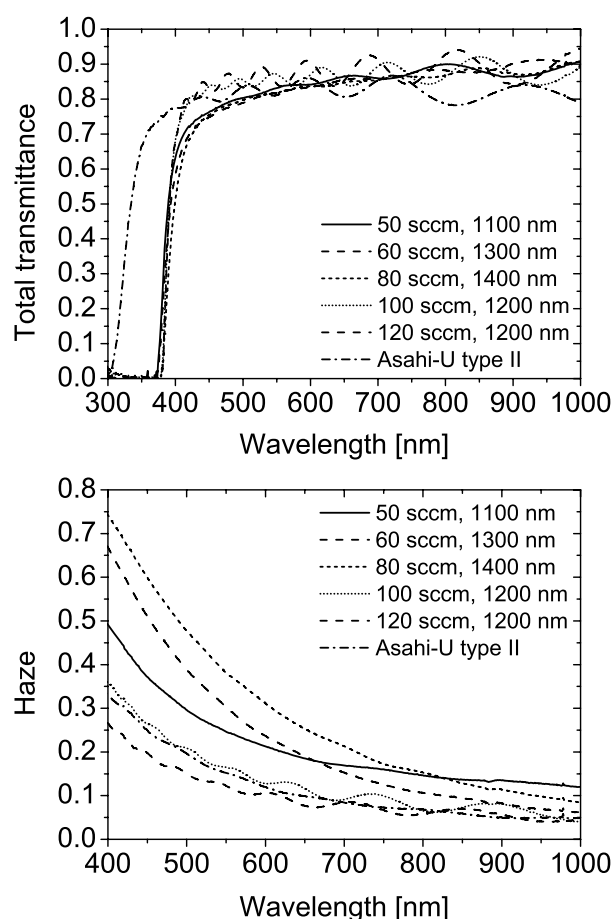


Figure 3.13: Total transmittance(top) and haze (bottom) spectra of undoped ZnO layers deposited with different oxygen flows.

ducibility for all samples from this series. These samples have been deposited after considerable changes to the gas injection, including the position of the gas injection ring within the reactor. Compared to the previous series, this resulted in higher deposition rates around 1 nm/s, also for the standard process with 50 sccm O_2 flow. While the surface structure changes considerably from pyramid-like to dome- and cone-shaped with increasing oxygen incorporation (Figure 3.12), the crystal growth is purely columnar and with the [002] direction perpendicular to the substrate. From Figure 3.13 it can be seen that the total transmittance between 400 nm and 600 nm is higher for the samples deposited with higher oxygen flow,

indicating less absorption losses, probably due to a lower concentration of defects. These defects are also referred to as color centers as they lead to a colored appearance of the film. In ZnO these color centers can be associated with the same states responsible for the electrical conductivity: oxygen vacancies and Zn interstitials lying a few tens of an eV below the conduction band. The absorption of blue light is ascribed to electronic transitions from the valence band into these states [43,76], resulting in a characteristic yellow appearance of the films in transmittance. The haze of the samples (lower graph in Figure 3.13) increases when the oxygen flow is increased from 50 sccm up to 80 sccm, but is far lower again for the more stoichiometric samples. This can be related to the observed change in surface structure from small sharp pyramids via larger pyramids efficiently scattering the light, to even larger cones forming a smoother surface.

Thus, the 50 sccm O₂ chosen for the standard ZnO recipe is the best compromise of still low resistivity combined with acceptable haze and transmittance. The layers deposited with higher O₂ flow exhibit better transmittance in the blue as a result of a lower concentration of color centers, but this makes them far less conductive and therefore unsuitable as front TCO for amorphous silicon pin solar cells.

3.4.4 Argon Flow through the Cascaded Arc

With increasing argon flow through the plasma arc the density of excited species in the plasma increases. This has a strong influence on the growth of the ZnO films, as can be seen in Figure 3.15. The films all grow in a columnar structure

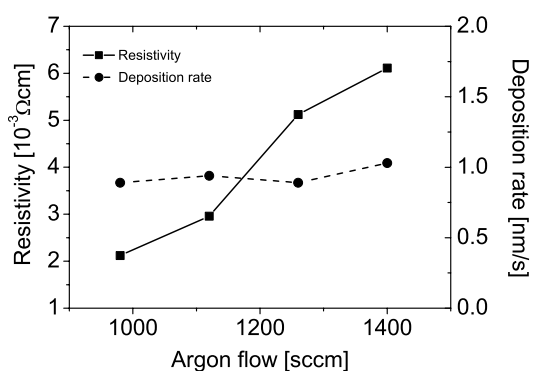


Figure 3.14: Resistivity and deposition rate of undoped ZnO layers as function of the Ar flow through the plasma arc

Argon flow through cascaded arc series, cascaded arc 2, gas injection 2

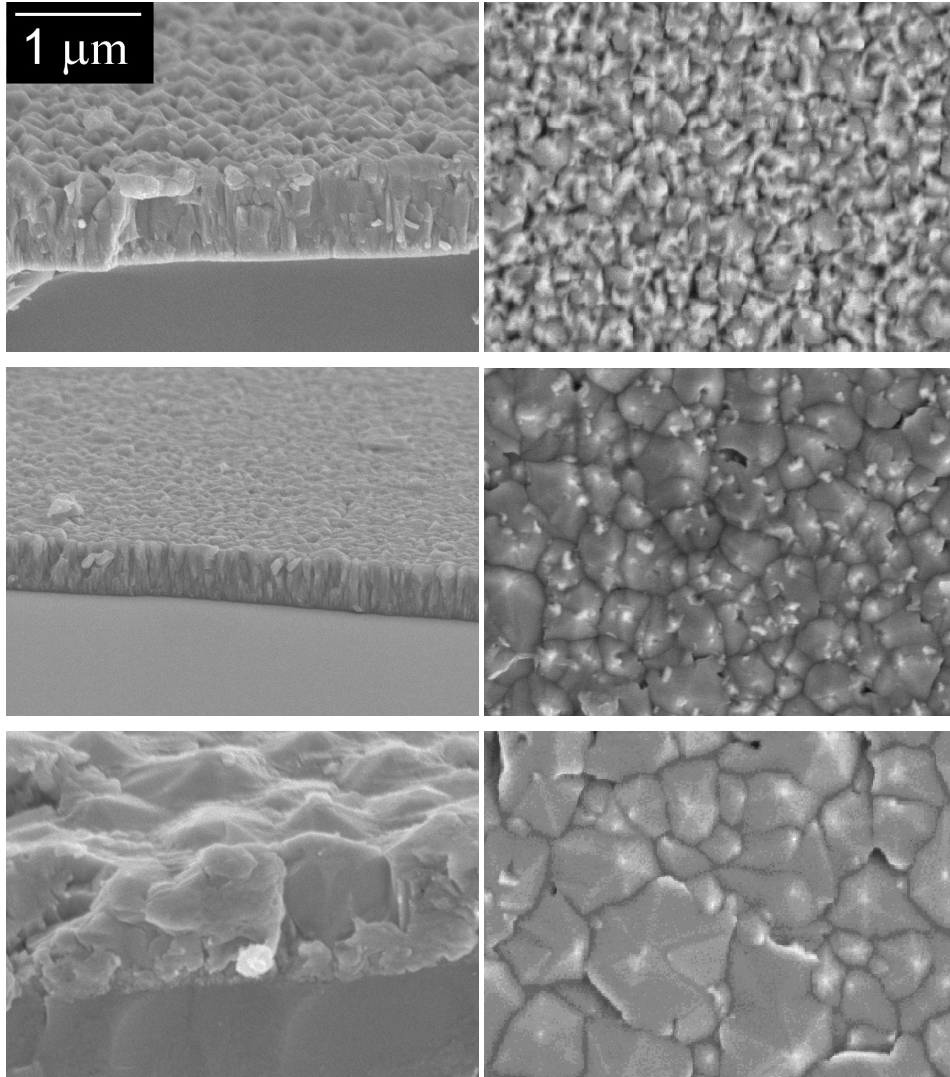


Figure 3.15: Cross sectional and surface SEM micrographs of undoped ZnO layers deposited with argon flows through the plasma arc of 980 sccm, 1260 sccm, and 1400 sccm (from top to bottom).

with exclusively [002] reflection peaks in the XRD spectra, but the crystal size increases drastically with higher Ar flow. This also leads to an increase in rms

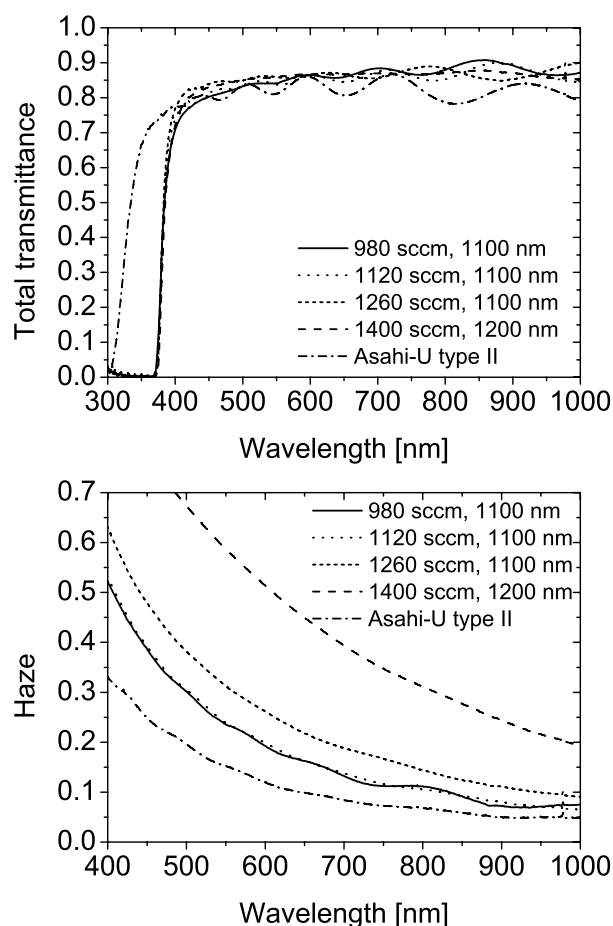


Figure 3.16: Total transmittance(top) and haze (bottom) spectra of undoped ZnO layers deposited with different argon flows through the plasma arc.

surface roughness determined by AFM from 39 nm via 59 nm to 76 nm when the Ar flow is increased from 980 sccm via 1260 sccm to 1400 sccm.

As shown in Figure 3.14, also the resistivity of the films increases with increasing Ar flow. The optical transmittance of the samples is higher than for Asahi U-type. For the samples deposited at higher Ar flow, a higher blue transmittance as in the case of higher O_2 flows is observed. It is therefore speculated that the density of oxygen vacancies is lower at higher Ar flows, which can explain the lower absorption losses in the blue, and the higher resistance as a result of a lower free carrier density in spite of the larger crystallites. The lower density of oxygen

vacancies in the film can be a result of the more efficient excitation of oxygen in the plasma at higher Ar flows through the plasma arc [72].

Also the haze of all samples deposited in this series is higher than for the reference TCO, see Figure 3.16. As expected, the increase in surface roughness with higher Ar flow also leads to an increase in haze up to a value as high as 50% at 600 nm wavelength for the sample deposited with the highest Ar flow of 1400 sccm.

The increased Ar flow leads to ZnO layers with remarkably high haze and high transmittance. At the same time, however, the resistivity of the films decreases, making them less suitable as front TCO for amorphous silicon pin solar cells.

3.5 Aluminum Doped Zinc Oxide

The motivation to dope the ZnO films was twofold. On the one hand it is expected that films have more stable electronic properties. As a result of the doping, additional free charge carriers are injected from the donor states into the conduction band. The activated donors cannot be compensated by post oxidation as easily as oxygen vacancies, so that films with more stable electric properties are expected. Also the decrease in mobility as a result of oxygen chemisorption at the grain boundaries [73,74] is absent for sufficiently doped layers. A high carrier concentration within the grains decreases the width of the grain boundary barrier to only 1 to 3 nm [73] which can easily be passed by tunneling.

On the other hand, a lower resistivity is expected than in the undoped case due to the additional free charge carriers. This might allow to take advantage of layers with preferred optical properties obtained in the previous section, which otherwise suffer from a too high resistivity.

The doped layers investigated in this section were deposited starting from deposition parameters leading to nearly stoichiometric layers, i.e. with an O₂ flow of 100 sccm. Three sample series are presented, with variation of TMA flow into the deposition chamber and thus doping concentration of the film, substrate temperature, and argon flow through the plasma arc, consecutively.

3.5.1 TMA Flow

The addition of TMA into the deposition chamber leads to the incorporation of aluminum as an active n-type dopant into the film. In Figure 3.17 the Al content of the films as a function of the TMA flow is shown. As expected, the Al content increases with higher TMA dosing.

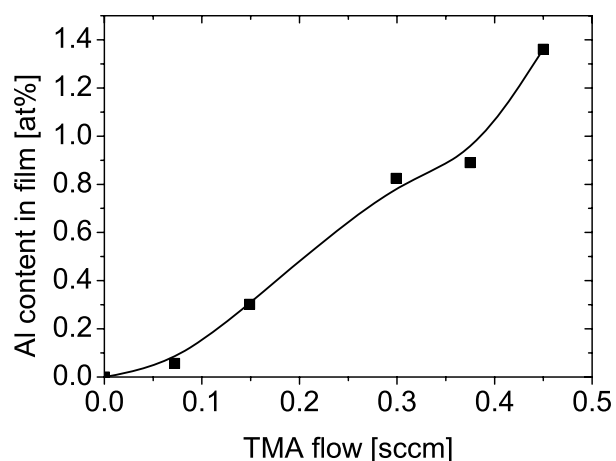


Figure 3.17: Al content in the ZnO:Al film determined by EDX as a function of TMA precursor flow.

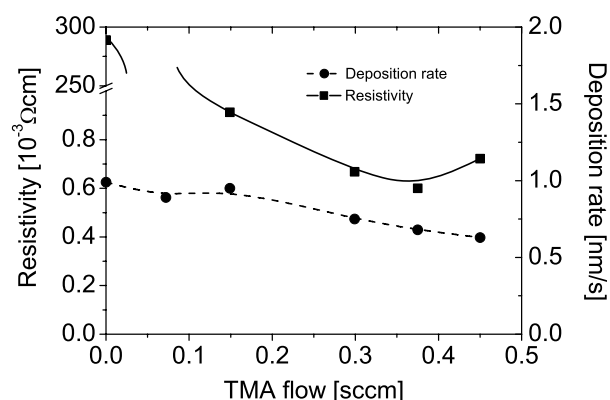


Figure 3.18: Resistivity and deposition rate of doped ZnO:Al layers as function of the TMA precursor flow.

The resistivity (see Figure 3.18) changes from $0.3 \Omega \text{cm}$ for an undoped film to $1.1 \times 10^{-3} \Omega \text{cm}$ already with a low TMA flow of 0.07 sccm. Further increase in TMA flow up to 0.38 sccm leads to a slight decrease in resistivity down to $6.0 \times 10^{-4} \Omega \text{cm}$. Only for the highest TMA flow in this series a slightly higher resistivity is observed, indicating a saturation of the beneficial effect of doping. Probably too much Al is incorporated into these films so that the creation of charged impurities leads to a decrease in charge carrier mobility overcompensat-

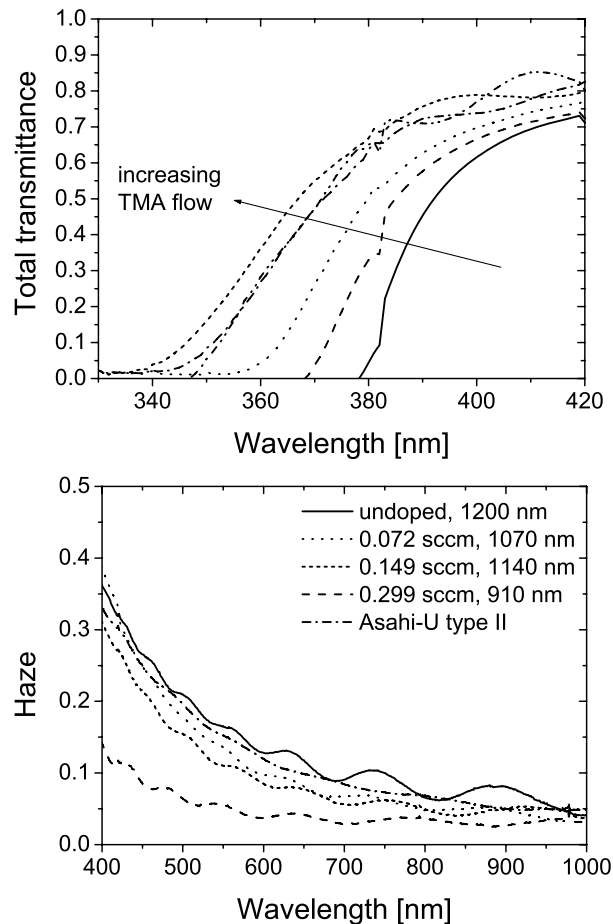


Figure 3.19: Total transmittance(top) and haze (bottom) spectra of doped ZnO:Al layers deposited with different TMA precursor flows.

ing the higher charge carrier density [31]. Also the formation of Al_2O_3 could play a role here, which leads to the incorporation of insulating clusters into the ZnO:Al film [45]. For APCVD deposited ZnO:Al, Hu [45] reports on saturation of the conductivity at Al contents as low as 0.45 at-%, which is in quite good agreement with our findings. The total transmittance spectra in Figure 3.19 show the widening of the absorption band gap with increasing TMA flow, also indicating a higher charge carrier concentration in the film.

Taking the lowest SEM micrograph from Figure 3.12 as undoped reference,

TMA flow series, cascaded arc 2, gas injection 2

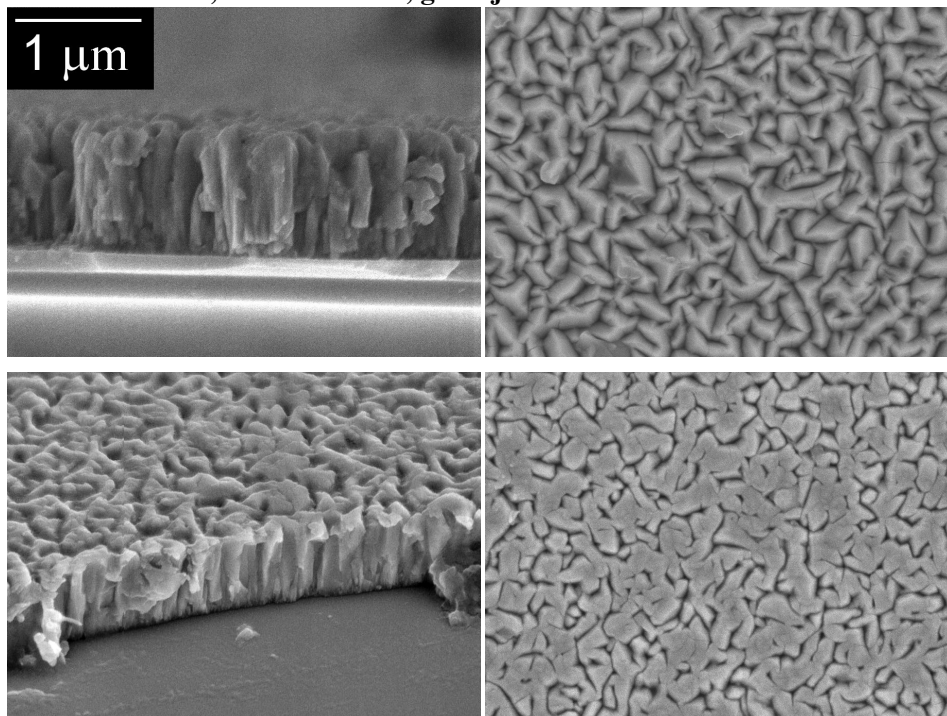


Figure 3.20: Cross sectional and surface SEM micrographs of doped ZnO:Al layers deposited with TMA flows of 0.149 sccm (top) and 0.375 sccm (bottom).

from Figure 3.20 it becomes obvious that the addition of TMA into the deposition chamber has a significant influence on the film structure. At low TMA flows, the textured surface as observed for the undoped film is maintained, while the size of the columns and the surface texture decreases. At higher TMA flows, the surface of the columns becomes flat, with sharp facets forming steep trenches between the columns. Also from the haze spectra in Figure 3.19 it is deduced that the film surface becomes smoother with Al incorporation. Unfortunately the thickness of the films is not identical, but the decrease in haze with higher TMA flow cannot solely be explained by the decreasing thickness of the films. It is speculated that an increase in the density of nucleation sites as observed in the presence of triethylaluminum (TEA) [45], can also explain the smaller crystallites when TMA is used as precursor for Al doping. The smaller crystallites give rise to a decrease in film roughness. Thus, the wanted decrease in resistivity as a consequence of Al doping of the film, results also in a decrease in film roughness

and optical haze. Further parameter variations have been performed with the goal to obtain efficiently doped and at the same time sufficiently rough ZnO:Al films.

3.5.2 Substrate Temperature

As seen in the previous section, the addition of TMA into the deposition chamber as a dopant apparently results in changes of the film growth. The layers deposited in this temperature series with a constant TMA flow of 0.15 sccm were prepared with the same hardware settings as the undoped temperature series 2. Comparing

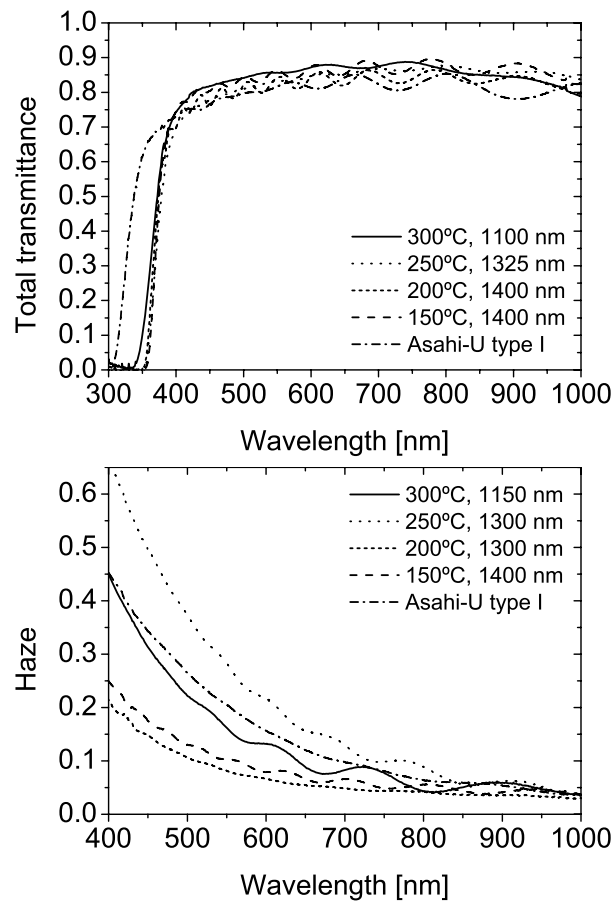


Figure 3.21: Total transmittance(top) and haze (bottom) spectra of doped ZnO:Al layers deposited at different substrate temperatures.

Temperature series, cascaded arc 2, gas injection 1

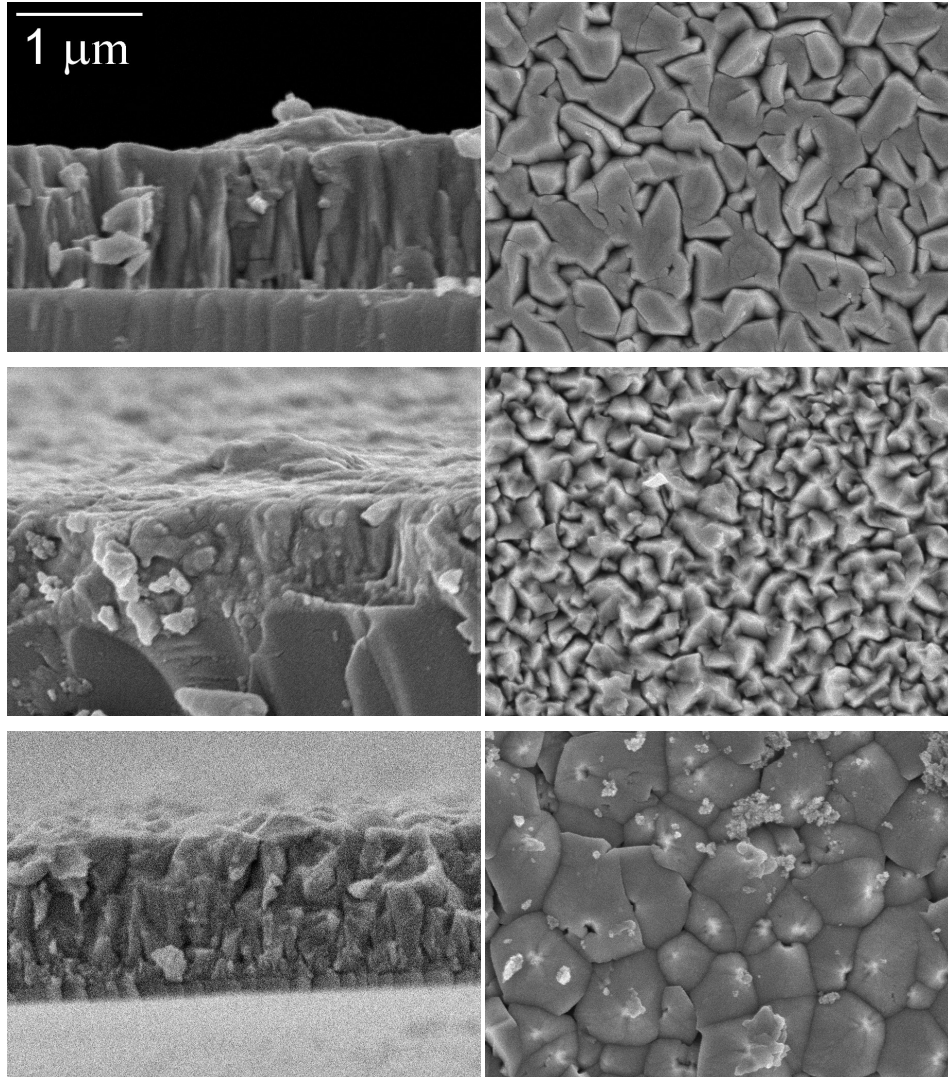


Figure 3.22: Cross sectional and surface SEM micrographs of doped ZnO:Al layers deposited at 200°C, and 300°C, and a layer deposited at 200°C with higher Ar flow through the plasma arc (from top to bottom).

the doped ZnO:Al layers deposited at 200°C and 300°C in 3.22, with their undoped counterparts in Figure 3.8 it can be seen that the transition from columnar

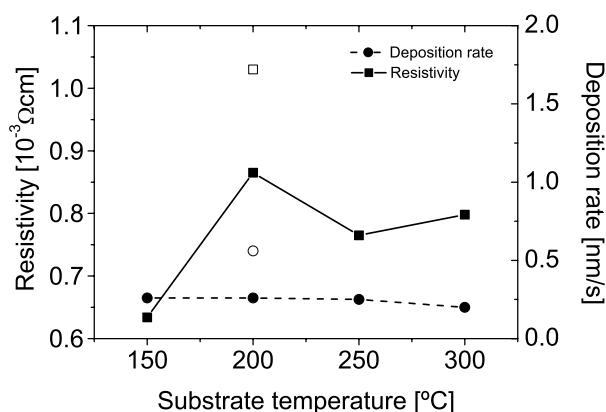


Figure 3.23: Deposition rate and resistivity of doped ZnO:Al layers as function of the substrate temperature. The open symbols depict the sample deposited with higher Ar flow through the plasma arc.

to granular growth observed for undoped layers is absent in the case of doped layers in the investigated temperature regime up to 300°C. In the presence of TMA, within the investigated substrate temperature regime, the growth stays obviously columnar.

The top of the crystallite columns for the ZnO:Al layer deposited at 200°C appears flat in contrast to the pyramid-like tips in the case of undoped layers. The surface texture of the doped layers also exhibits some vertical steps and sharp peaks. The surface of the ZnO:Al layer deposited at 300°C exhibits some pyramidal shapes, but also steep trenches and sharp edges can be seen. It has to be taken into account that in addition to the presence of TMA, also the higher oxygen flow for the deposition of the doped films compared to the undoped films plays a role here.

All doped ZnO:Al layers deposited at substrate temperatures ranging from 150°C to 300°C show high optical transmittance above 80% for visible light (Figure 3.21, comparable with the undoped layers). The absorption gap is widened with respect to the undoped layers, indicating a higher carrier concentration and thus efficient doping. With increasing deposition temperature, a higher haze is found, as in the case of undoped layers. It has to be noted that the doped ZnO:Al layers show lower haze than the Asahi U-type TCO and the undoped ZnO layers. This is in accordance with the observed flat features at the film surface seen in Figure 3.22. The layers are around 1200 nm thick and have resistivities below $10^{-3} \Omega\text{cm}$ (Figure 3.23), practically independent of the deposition temperature.

This is in accordance with the findings of Hu for APCVD deposited ZnO:Al [45], that the Al incorporation into the film is virtually independent of the substrate temperature. The increase in substrate temperature therefore led to slightly rougher samples with still low resistivity, but the haze for these doped ZnO:Al layers is still lower than for the undoped ZnO films.

3.5.3 Ar Flow through the Cascaded Arc

In the substrate temperature series shown above, one sample was deposited at 200°C, but with a higher Ar flow through the plasma arc. In the lowest SEM micrographs in Figure 3.22 it can be seen that this leads to a transition from columnar to granular growth, and a rough film surface formed by the rounded surface of the grains is obtained. This is confirmed by XRD, where reflection peaks of the [100] and [103] directions are observed. As this ZnO:Al layer was successfully applied in a solar cell (see chapter 4), a complete series of ZnO:Al layers with a variation of the Ar flow was deposited. In this series the gas injection was identical as in the TMA series, and thus different from the temperature series. Surface and cross sectional SEM micrographs of these films are shown in Figure 3.25. As in the case of undoped layers, the argon flow through the plasma arc has a huge effect on the growth of the polycrystalline film. With increasing Ar flow a transition from columnar to granular growth is observed, with the surface changing from a more pyramidal shape via cone shaped to a surface formed by the differently

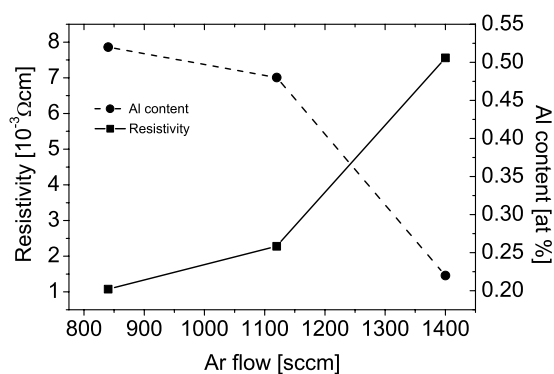


Figure 3.24: Resistivity and Al content of doped ZnO:Al layers as function of the Ar flow through the plasma arc.

Argon flow through cascaded arc series, cascaded arc 2, gas injection 2

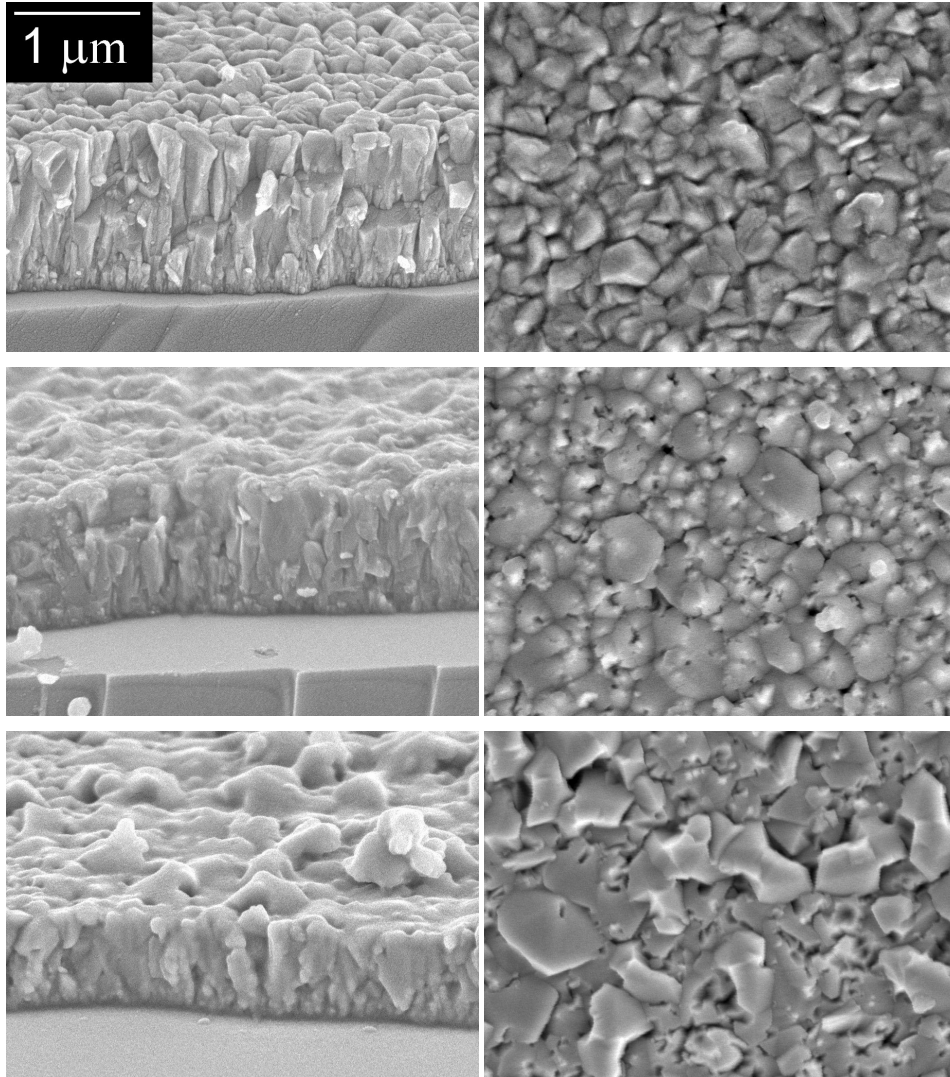


Figure 3.25: Cross sectional and surface SEM micrographs of doped ZnO:Al layers deposited with argon flows through the plasma arc of 840 sccm, 1120 sccm, and 1400 sccm (from top to bottom).

shaped grains resulting from granular growth. This transition is accompanied by an increase in Rms surface roughness from 23 nm to 57 nm. At the same time,

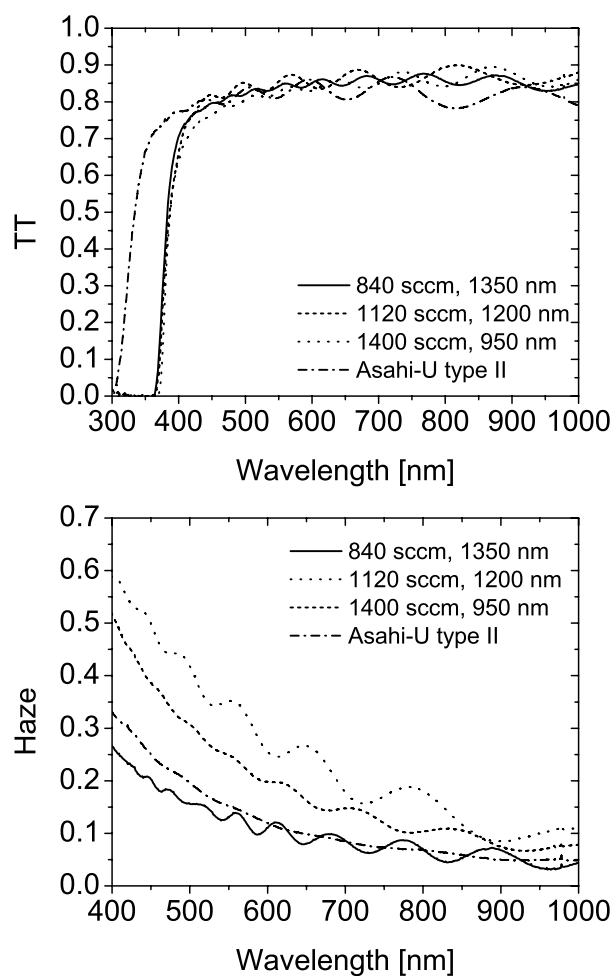


Figure 3.26: Total transmittance(top) and haze (bottom) spectra of doped ZnO:Al layers deposited with different Ar flows through the plasma arc.

interestingly, the amount of Al incorporated into the film drops considerably as presented in Figure 3.24. Certainly for the layer deposited with the highest Ar flow of 1400 sccm the observed difference in Al content is significant. This can also explain the electrical properties of the films. With increasing Ar flow, the resistivity increases as the Al content and therefore the concentration of free charge carriers decreases. This is also reflected in a slight shift of the effective optical absorption band edge and lower free carrier absorption at long wavelengths, see

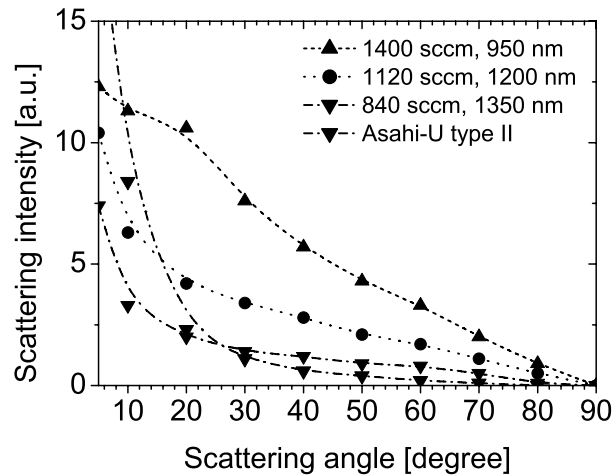


Figure 3.27: Angular resolved scattering of doped ZnO:Al layers deposited with different Ar flows through the plasma arc.

Figure 3.26. With higher Ar flow through the cascaded arc plasma source, the excitation of oxygen is enhanced [72] which might lead to the formation of Al_2O_3 in the gas phase and thus lower doping efficiency of the films. Concerning the light scattering properties, the increase in surface roughness with higher Ar flow also leads to a higher haze. All samples presented here show higher haze than the Asahi U-type reference. The angular resolved scattering curves in Figure 3.27 exhibit interesting features. The layers deposited at the two highest Ar flows have clearly better scattering properties than the Asahi U-type. Note that also for large angles $>60^\circ$ higher scattering intensities than for the reference TCO are observed. The sample deposited with 1120 sccm Ar flow has a relatively slowly decaying scattering intensity curve comparable to the type I Asahi-U TCO as discussed in 3.3. The ZnO:Al layer deposited at the highest Ar flow of 1400 sccm exhibits a characteristic scattering intensity curve with a shoulder which is similar to the type I Asahi U, but shifted towards the specular light peak.

This last series of ZnO:Al samples is very promising as front TCO for a-Si pin solar cells, mainly due to their optical properties. Unfortunately, also here the electrical properties deteriorate with increasing haze. With respect to the Ar flow series on undoped ZnO, in spite of the efficient Al doping no significant improvement in conductivity is obtained.

3.6 Conclusions

Natively textured undoped ZnO and doped ZnO:Al layers have been deposited by the expanding thermal plasma CVD technique between 150° and 350°C at a deposition rate between 0.2 and 1.3 nm/s. Films exhibiting native texture, electrical (sheet resistance < 10 Ωcm) and optical (transmittance > 80 %) properties comparable to Asahi U-type SnO₂:F have been obtained.

The influence of several deposition parameters on the structural, morphological, and optoelectrical properties of the films have been studied. The surface roughness of the ZnO layers increases with growing film thickness indicating the successive evolution of native roughness during growth of the ZnO film. Crystallite size and surface roughness of the films also increase with increasing substrate temperature. For undoped ZnO, a transition is observed between 250°C and 350°C from columnar growth with the c-axis of the hexagonal crystal ([002] direction) perpendicular to the substrate, to granular growth exhibiting additional grains with [103], [101], and [102] orientation. This transition comes along with a change in surface structure from a sharp texture stemming from the tips of the crystallite columns to more rounded features due to the granular structure. All these layers show, regardless of their morphology, comparable optoelectronic properties to the Asahi U-type reference SnO₂:F TCO.

By the addition of trimethylaluminum into the reaction chamber highly conductive Al doped ZnO layers with high optical transmittance above 80% for visible light have been obtained at substrate temperatures ranging from 150°C to 300°C. However, film growth and structure are significantly different than for the presented undoped layers, resulting in films with a flatter surface exhibiting lower haze. An increase of the Ar flow through the cascaded arc plasma source leads to an increase in surface roughness, but at the same time the conductivity of the aluminum doped ZnO layers decreases, comparable to the case of undoped ZnO films deposited at increased Ar flow.

Outlook

A better understanding of the gas phase and film surface reactions during the growth of ZnO and ZnO:Al layers by ETP CVD is desirable. Future research could be directed towards further optimizing the electrical and optical properties simultaneously by combining results from the presented series. For example, higher doping concentrations in combination with high Ar flows through the plasma arc might result in more conductive layers with optical properties superior to Asahi U-type. Also the approach to use less conductive layers with high

transmittance, and deposit them to a larger thickness around 2 μm as done successfully by the Neuchâtel group for LPCVD ZnO [44] may lead a path to further improvement of the ETP CVD deposited ZnO and ZnO:Al layers as front TCO for amorphous silicon solar cells. Also the full potential of high rate deposition by ETP CVD still has to be proven for the deposition of zinc oxide. Current deposition rates for ETP CVD around 1 nm/s are still below the rates for conventional CVD, where the deposition rate is actually limited by the substrate temperature, and a value of 3.7 nm/s has been reported for an LPCVD process at 180° [44].

The performance of the thus far developed undoped ZnO and Al doped ZnO:Al layers in amorphous silicon pin solar cells is presented in the next chapter. For this purpose, the most interesting and promising samples combining high haze and reasonable conductivity have been selected, namely the two temperature series of undoped ZnO, and the temperature as well as the Ar flow series of doped ZnO:Al layers.

4 Solar Cells on Zinc Oxide Superstrates

4.1 Introduction

In this chapter the results of solar cells deposited on the Expanding Thermal Plasma (ETP) CVD grown ZnO and ZnO:Al layers that were presented in chapter 3 are reported. As described, the ETP CVD technique enables to grow natively textured ZnO and ZnO:Al layers with optoelectronic properties comparable to those of Asahi U-type SnO₂:F, thus making them promising candidates as front TCO for thin-film silicon pin solar cells.

From literature it is known that a non optimum morphology of the TCO can lead to a decrease in V_{oc} and FF of the solar cell [77,78]. In addition to this, indications were found recently that the haze of the TCO alone is not the most adequate parameter to predict the short circuit current density one can expect from a solar cell. Rather the angular distribution of the scattered light has to be taken into account [79–81].

Consequently, the first question was whether the promising TCO properties obtained for zinc oxide deposited by ETP CVD as described in the previous chapter can indeed translate high solar cell efficiencies. In addition to this, from the results reported in Chapter 3 the questions arose whether a columnar or granular morphology of the zinc oxide is preferred for the solar cells, and whether there is an optimum in roughness of the TCO to achieve highest solar cell efficiencies. Also the advantages and disadvantages of aluminum doped zinc oxide (ZnO:Al) compared to undoped ZnO in the application as front TCO for thin-film silicon pin solar cells have been investigated.

In Section 4.2 an introduction to the relation between light scattering properties of a TCO and the expected spectral response of the solar cell is given based on optical device simulations. An important issue for these simulations is, amongst others, the modelling of the light scattering mechanism and its dependence on the TCO morphology. In the succeeding section 4.3 the loss mechanisms in solar cells which are known to originate from electrical, optical and morphological TCO properties, are reviewed. After an overview of the experimental techniques applied, amorphous silicon (a-Si) pin solar cells on the reference TCOs are described. Section 4.6 is dedicated to the interface between TCO and p-layer of the solar cell, which has been reported to be problematic when zinc oxide is combined

with an amorphous p-layer [82]. Solar cells on undoped and aluminum doped zinc oxide deposited by ETP CVD as front TCO are presented in the sections 4.7 and 4.8, respectively. First results on microcrystalline silicon solar cells deposited on ZnO made by ETP CVD are reported in section 4.9. Finally, ZnO and ZnO:Al films deposited by the ETP CVD technique are compared to zinc oxide obtained by other techniques with respect to their suitability as front TCO material for thin-film silicon pin solar cells.

4.2 Light trapping in Solar Cells

In thin-film solar cells, it is a challenge to achieve high photocurrents in spite of the small thickness of the absorber material. For long wavelength light with absorption lengths larger than the thickness of the absorber layer, the effective optical path length through the material has to be increased. For pin thin-film silicon solar cells, the combination of rough front TCOs resulting in light scattering interfaces, and highly reflecting back contacts, allows the trapping of light within the solar cell structure as a result of multiple (total) internal reflections. The theoretical limit of the enhancement of the pathlength is $4n^2$ [83], with n being the refractive index of the optical medium. While this would predict a value around 50 with $n \simeq 3.5$ for silicon, in practice far lower values around 5 have been reported for amorphous silicon solar cells [84]. This large gap indicates the importance of a better understanding of the involved light trapping processes.

For the understanding of light trapping processes in a thin-film solar cell, both the scattering at rough interfaces and the propagation of specular and scattered light through the solar cell structure have to be taken into account. A concise overview on optical device modelling is given in [12], where a full chapter is dedicated to the topic. Here, a brief introduction to scattering theories and solar cell device simulations is given with focus on the validity of the Mie scattering theory applied to simulate the haze spectra of Asahi U-type TCOs, and the *Sunshine* software developed at the University of Ljubljana, Slovenia, that was used to simulate the influence of the i-layer and the TCO thickness, as well as the TCO surface roughness on the spectral response of amorphous silicon pin type solar cells.

4.2.1 Scattering at Rough Interfaces

A better understanding of the optical scattering mechanism especially at the TCO/silicon interface may help to develop TCOs with improved surface roughness resulting in optimally scattering interfaces in the solar cell device. Also for the

optical modelling of thin-film silicon solar cells, the assumption of a scattering model is necessary. Generally, the scattering of light at an interface depends at least on three factors, namely the dimensions of the roughness, the wavelength of the light, and the optical constants on either side of the interface. While haze and angular resolved measurements in transmittance can only be performed on TCO samples on glass, in the real cell structure the scattering occurs mainly at the TCO/ silicon and silicon/ back contact interfaces. In practice, measurements at the TCO/ air interface are used to predict the scattering at the TCO/ silicon interface by replacing in the applied scattering theory the dielectric function of air with the function for silicon.

Modelling of Haze Spectra

The difficulty in modelling the measured haze spectra (haze = ratio of diffuse to total part of transmittance or reflectance, see Section 2.2.1) of front TCOs of thin-film silicon solar cells with a physical model arise from the fact that the features creating the surface roughness and thus the light scattering at the TCO surface have approximately the size of the wavelength of the visible light in the TCO material. Thus, neither Rayleigh scattering, predicting a λ^{-4} dependence of the haze for scattering at particles smaller than the wavelength, nor geometrical optics for features larger than the wavelength can be applied. An example for the latter case are the micrometer sized pyramids etched in monocrystalline silicon wafers used for solar cells.

Often the scalar theory is applied [85] which describes scattering from a surface with spatially correlated roughness. The haze is then only dependent on the rms roughness σ and the refractive indices n_1 and n_0 of the media forming the interface [86]. In order to get better agreement with experimental data, Zeman *et al.* [85] proposed the empirically modified formula for the haze in transmittance H_T

$$H_T = 1 - \exp[-(4\pi\sigma_r C |n_0 - n_1|/\lambda)^3], \quad (4.1)$$

where C is a correction factor which can be adjusted to fit the experimental data.

Another approach is to consider the light scattering features at the TCO surface as independent particles emersed in air. Then Mie theory [87] can be applied, which describes the scattering of electromagnetic waves by a spherical particle. Though the physical problem of an electromagnetic field around a spherical object is simple, its mathematical treatment is intricate. In [88] the lengthy formalism in which the incoming plane wave is expanded into spherical harmonics, is described. Figure 4.1 shows the scattering efficiency Q of a tin oxide sphere in air as a function of the wavelength, for spheres with different radii, as calculated by

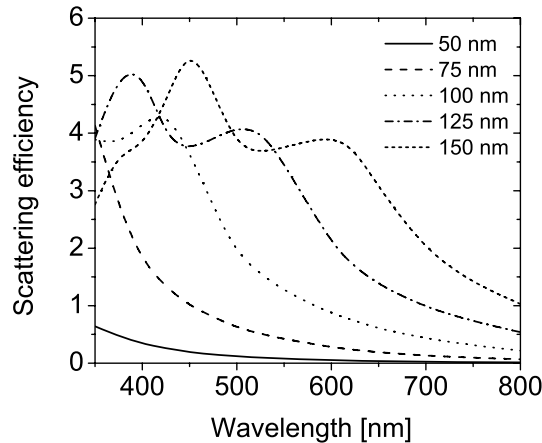


Figure 4.1: Scattering efficiency Q of tin oxide spheres in air as a function of the wavelength, for spheres with different radii.

the computer program *BHMIE* [88]. $Q(m, a)$ is a function of the ratio m of the refractive indices of the sphere and of the medium, and of the radius a of the sphere. Characteristic for Mie scattering is the occurrence of a resonance which moves to longer wavelengths with increasing particle size.

We have tried to relate results from Atomic Force Microscopy (AFM) measurements on the two types of Asahi U-type TCOs (see Section 3.3) with the measured haze spectra in transmittance making use of Mie theory. It is not straightforward to describe the textured TCO surface by a collection of spheres. As suggested by Schade and Smith [89], the pyramids of height h and width b have been replaced by spheres with radius $r = h/2$ arranged in a square array of spacing b . It was found that an ensemble of spheres with a gaussian size distribution resulted in excellent agreement between simulated and measured haze spectra, see Figure 4.2. Interestingly, we found that the width of the gaussian distribution corresponds to the rms value, and the center of the distribution coincides with the mean height value $\langle h \rangle$ as determined by AFM. Only one fitting parameter was used, the parameter C_0 which relates the haze, or fraction of scattered light S to the scattering efficiency $Q(m, a)$ by $S = C_0 \cdot Q(m, a)$ [89]. For each radius a , the same fixed C_0 was used. The superposition of spheres with different sizes leads to the disappearance of the resonances in the haze spectra, and results in the λ^{-3} dependence found experimentally. It is striking that such a superposition of individual

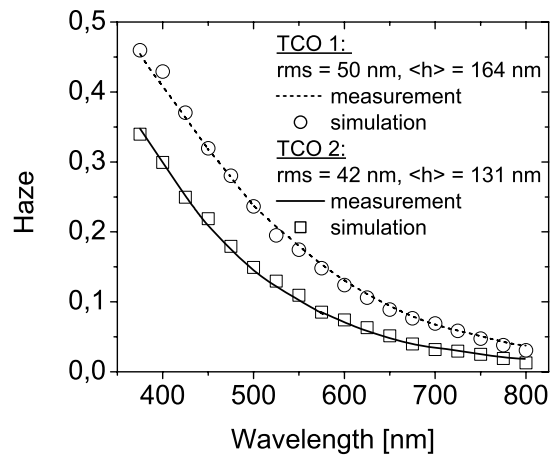


Figure 4.2: Measured and simulated haze spectra of two types of Asahi-U TCO (see Section 3.3).

spherical scattering particles can indeed describe the entire ensemble of scattering centers. O'Dowd [90] speculated that at the TCO surface pairs of conjugated particles can be found for which the scattering matrix can be replaced by the matrix for a single spherical particle [91].

Most of the investigated ZnO and ZnO:Al layers deposited by ETP CVD as described in Chapter 3 exhibit haze spectra with a λ^{-x} dependence with x varying between 2.5 and 3 indicating that the Mie scattering might be applicable here. However, the height distribution deduced from AFM measurements is not gaussian, making it more difficult to assume an appropriate size distribution of scattering particles. More research is necessary here, in particular the simulation of the angular distribution of scattered light is of great importance for the light trapping in thin-film silicon solar cells.

4.2.2 Modelling of Light Propagation through the Solar Cell Structure

When modelling the light propagation through the solar cell structure, it is important to take both coherent unscattered light and incoherent scattered light into account. Each time the light hits an interface, it can be reflected or transmitted.

Scattered light will further be scattered, while the coherent light will either further contribute to the unscattered and thus coherent fraction of the light, or, if scattering occurs, it has to be treated as scattered incoherent light. Thus, a realistic model has to take all these possible events into account at each interface in the solar cell. As explained above, the scattering is strongest the larger the difference in (complex) refractive indices is for the materials forming the interface, and the rougher the interface is.

While the roughness of the formed interfaces is only slightly decreasing in the sequence of layer deposition (TCO - p - i - n - back contact) due to the nearly conformal coating of the TCO during solar cell deposition, Zeman et al. [85] have shown that the interfaces where the dominant part of the scattering occurs are the TCO/p and the n/back contact interfaces. A minor contribution stems from the p/i interface, which is in agreement with the refractive indices of the involved TCO, (p) a-SiC:H, (i) and (n) a-Si:H, and Ag respectively Al.

At Utrecht University, a computer program based on ray tracing has been developed which has successfully been applied to simulate the spectral response of amorphous silicon pin solar cells, making use of the Mie scattering formalism at the n / metal contact. However, the software code required too much time for a single cell simulation as to allow systematic studies [92].

Krč from the University of Ljubljana, Slovenia, has developed the code *Sunshine* based on a wave propagation algorithm [93] which allows the treatment of the coherent light as wave, characterized by its direction of propagation, amplitude, and phase, thus enabling to calculate the correct interference pattern resulting from the superposition of all contributions to the unscattered coherent light.

Relating the scattered and unscattered fractions of the light in reflectance and transmittance at each interface via the fresnel coefficients and (scalar) scattering formulas, a consistent model has been built up. Characteristic for this model is that not only measured haze data of the TCO/air interface in transmittance and reflectance are taken into account, e.g. by applying a wavelength dependent $C(\lambda)$ in Formula 4.1, but also empirical angular resolved scattering data. While many earlier programs assumed a simple Lambertian distribution of the scattered light [92,94], here even the dependence of the angular distribution function (ADF), i.e. the distribution of scattered light in reflectance and transmittance with respect to the incident beam, on the angle of incidence is taken into account. Interestingly, for some TCOs (e.g. the Asahi-U type I described in Section 3.3) the angle of incidence necessary to obtain the (specular) maximum of the angular resolved scattering in reflectance to be at 60° , the incident beam has to reach the surface under an angle smaller than 60° . This indicates that such a scattering surface behaves partially like a grating and thus indeed has to be treated as an ensemble of

correlated scattering centers. Also a small correction for the dependence of the ADF on the wavelength of the light is implemented. The spectral response of the solar cell is calculated from the light absorbed in the intrinsic layer, corrected by a factor accounting for recombination losses, which in first approximation is wavelength independent and has a value around 0.9. Light absorbed in the TCO, doped layers and the back contact is assumed to be lost for photocurrent collection.

Krč *et al.* have shown the successful application of this model to amorphous silicon pin solar cells on tin oxide [95] and zinc oxide [96], as well as to microcrystalline silicon and 'micromorph' tandem solar cells [97]. The importance of the form of the angular distribution function on the spectral response has been shown by this model [98], in agreement with recent experimental findings [79,81], which show that the scattering intensity at large angles between 45° and 90° is even a better measure for the light trapping in microcrystalline silicon solar cells than the haze value. Obviously these large scattering angles allow a larger fraction of the light to be totally reflected within the solar cell structure and thus result in efficient trapping of long wavelength light for photocurrent generation.

Here, the *Sunshine* software has been applied to visualize the dependence of the spectral response of an amorphous silicon pin solar cell on the i-layer and the TCO thickness, as well as on the TCO roughness when the scalar scattering theory is assumed.

Figure 4.3 shows the influence of the TCO roughness. The enhancement of the red response due to light trapping when applying a rough TCO is evident. Up to 600 nm, the maxima of the interference fringes for the cell with flat TCO coincide with the spectral response of the cell with rough TCO, because the absorption length in the silicon is for these wavelengths shorter than the cell thickness. Only for longer wavelengths the light trapping becomes visible. Note also the higher reflectance losses at short wavelengths for the cell with flat TCO at wavelengths in the vicinity of the minima of the interference fringes. An interesting effect in these simulations is found for the rear contact. Only when introducing a 1.5 nm thin interlayer of aluminum between (n) a-Si and the Ag back contact, a realistic spectral response is obtained. A pure (n) a-Si / Ag interface shows in simulations a far higher reflectance than observed in practical cell structures. Springer *et al.* attributed this to absorption losses at surface plasmons in the silver [99], which are not taken into account in the *Sunshine* software. Implementing these losses in their own simulation software, they could find good agreement with the experimental spectral response of microcrystalline silicon pin solar cells [100].

Figure 4.4 visualizes the effect of variations in TCO and intrinsic a-Si thickness. As the positions of the interference fringes for a cell with rough interfaces coincide with those of a cell with flat interfaces (see Figure 4.3), here for clarity

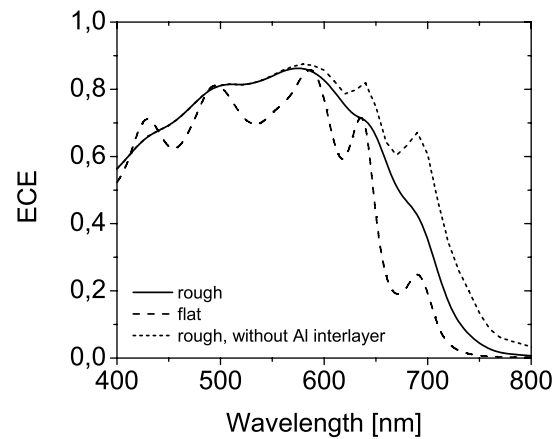


Figure 4.3: Simulation of the external collection efficiency of an a-Si pin solar cell on Asahi-U TCO with rough and flat front TCO. Also the effect of omission of the 1.5 nm thin Al interlayer in the simulation of the (n) a-Si / Ag interface is shown.

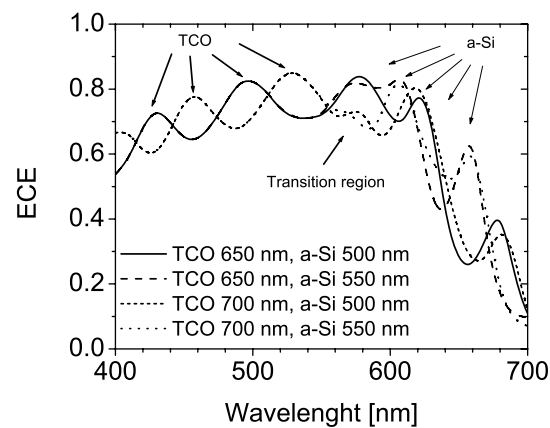


Figure 4.4: Simulation of the external collection efficiency of an a-Si pin solar cell on Asahi-U TCO with varying TCO and a-Si i-layer thickness.

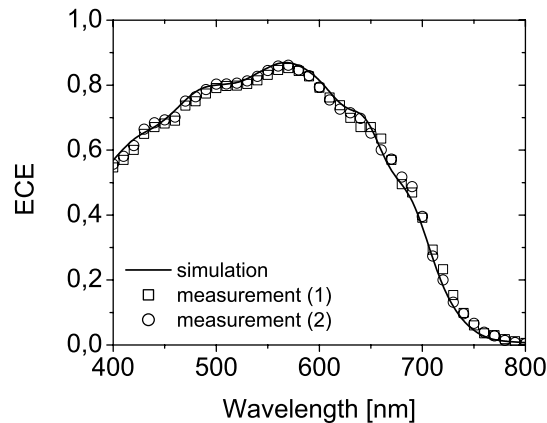


Figure 4.5: Simulation of the external collection efficiency of an a-Si pin solar cell on Asahi-U TCO compared with experimental results for two typical cells.

cells with flat interfaces are considered where the interference fringes are more pronounced. The interference fringes for short wavelengths up to 550 nm are solely due to the thickness of the TCO, which is straightforward as due to the high absorption coefficient of the a-Si, this light cannot travel multiple passes through the amorphous silicon. Between 550 nm and 600 nm, no clear correlation between the fringe position and the thickness of either TCO or a-Si can be deduced. Between 600 nm and 700 nm, the positions of the fringes coincide for cells with identical i-layer thickness, regardless of the TCO thickness. The thicker the intrinsic layer, the further is the spectral response curve shifted towards longer wavelengths. This is plausible because with increasing cell thickness, the wavelength for which the condition of a certain order of constructive interference is fulfilled also increases. The increase in absorber thickness naturally leads to a higher absorption of long wavelength light. Thus, a high red response can be achieved by a thick intrinsic absorber layer, or by an enhanced light trapping scheme, as presented in Figure 4.3. The latter is preferred as it allows to combine a high photocurrent generation in combination with a higher stability against the photoinduced Staebler-Wronski degradation for a solar cell with thinner intrinsic absorber layer. In contrast to the case of a thick absorber, the situation with a rougher TCO leads to less pronounced if not vanishing interference fringes.

After fine tuning of the input parameters for the simulations, an excellent fit to the experimental data has been obtained (see Figure 4.5) assuming an rms rough-

ness of 40 nm and 35 nm for the TCO/p and n/Ag interfaces, respectively, and thicknesses of 620 nm and 520 nm for the TCO and the intrinsic a-Si layer. The TCO roughness is very close to the experimental value of 42 nm (see Section 4.2.1, and a slight decrease in rms roughness of 7 nm after over 500 nm of a-Si deposition is realistic. The intrinsic amorphous silicon layer is aimed at a thickness between 450 nm and 500 nm when deposited on glass. An increase in layer thickness around 20% on a conductive substrate (in this case TCO) with respect to a layer on insulating glass has been reported earlier [101], and under the 50 MHz VHF conditions we find differences even up to 30%. Thus, the 520 nm found in the simulations, is a realistic value. The TCO thickness of 620 nm differs substantially from the thickness of 780 nm that we have determined with a stylus step profiler. This is attributed to the fact that the stylus is larger than the pyramidal features at the TCO surface, so that it cannot penetrate into the valleys of the texture, and the experimentally determined layer thickness is therefore the distance from the substrate to the top of the highest pyramids. The simulation data reflect the optical thickness creating the observed interference pattern, which in this case is probably close to the average thickness as found by Wallinga [26].

4.3 Non-ideal Solar Cells

A realistic a-Si pin solar cell can be described as a parallel circuit of a single-diode (equation 2.3) and a voltage dependent current generator, plus parallel and series resistance ($R_{parallel}$ and R_{series} , respectively) losses.

$$J = -J_{ph}(V) + J_0 \left(e^{\frac{-q(V - JR_{series})}{nkT}} - 1 \right) + \frac{V - JR_{series}}{R_{parallel}} \quad (4.2)$$

The current generator represents the generated photocurrent $J_{ph}(V)$. Its voltage dependency is given by the fact that due to interface and bulk recombination, not all photoexcited charge carriers can be extracted from the solar cell. At a high negative bias voltage (reverse bias), due to the high field in the device, most of the charge carriers will be extracted and thus contribute to the photocurrent, which is in the direction of the saturation current of the solar cell. With increasing bias voltage the band bending in the space charge region is reduced. When the applied voltage is positive and equal to the built-in potential, valence and conduction bands are flat throughout most of the device, and the extracted photocurrent is decreasing towards zero. At even higher positive bias, the photoexcited charge carriers are moving in the forward direction of the diode. The series and parallel resistance describe ohmic resistances which are in series with (like e.g. contact resistances) and parallel to (shunt paths) the pin diode, respectively.

In this section, an overview is given of the TCO induced electrical losses in a solar cell, and their influence on the solar cell parameters short circuit current density J_{sc} , open circuit voltage V_{oc} , and fill factor FF , as well as the areal resistance values R_s and R_p determined as the inverse of the slopes of the JV curve at V_{oc} and J_{sc} , respectively.

It is important to note that for an ideal single diode circuit with $R_{series} = 0$ and $R_{parallel} = \infty$, R_s and R_p are determined mainly by the diode quality factor n and the voltage dependence of the photocurrent, respectively. Thus, a high R_s and a low R_p do not necessarily mean that there is a large serial resistance or a low parallel resistance, respectively. Rather a low diode quality or strong dependence of the photocurrent on the applied voltage can often explain the losses found in experimental solar cells.

High sheet resistance

If the TCO of a solar cell has a too high sheet resistance, this will result in a higher series resistance R_{series} of the device. As the photocurrent has to pass this resistance, at a given current density J , the voltage of the cell will be lower by $J \cdot R_{series}$, thus decreasing the fill factor of the solar cell. The slope of the IV curve around V_{oc} will be smaller, so that a higher R_s is obtained. In a solar module, the series resistance as result of the TCO resistivity is a function of the cell width. With increasing cell width w and TCO sheet resistance R_{\square} , the power loss ΔP increases according to [102]

$$\Delta P = \frac{1}{3} R_{\square} w^3 J^2 l, \quad (4.3)$$

where l is the length of the cell. In practice, in a-Si pin solar cells with an area of $4 \times 4 \text{ mm}^2$, sheet resistances above $10 \text{ } \Omega/\square$ become visible as a higher R_s and a reduced FF .

Shunting

A pin solar cell is shunted, when there is an ohmic connection between the front electrode and the back contact parallel to the diode. If the connection between front and rear electrode has a high ohmic resistance or is non ohmic, the solar cell might still function. In this case the low parallel resistance characterizing the shunt path leads to a decrease in R_p and FF . The voltage dependent photocurrent is not affected by a shunt. When there is a direct low-ohmic electrical connection between the metal back contact and the front TCO, the device is short circuited

and has an ohmic IV curve typical for a (photo)resistor. A simple case where this is obtained is e.g. if the a-Si pin layer stack has pinholes [103], which are filled during the metallization step to form the back contact of the solar cell.

Defect Rich Growth and Electrical Barriers at Interfaces

Both chemical impurities originating from the TCO and the morphology of the TCO, can lead to the growth of defect rich amorphous silicon in the TCO/p/i region of the solar cell. Such a defective interface region can lead to enhanced recombination. This has an influence on the diode characteristic (high J_0 and low n). Also the photocurrent becomes more strongly voltage dependent, as recombination losses are strongly dependent on the electrical field in the device. As a result of this, the IV characteristics of the cell is mainly characterized by a lower R_p and FF. Also V_{oc} is affected as it decreases with increasing J_0 and decreasing n , see equation 2.5.

An electrical barrier due to band bending or a band discontinuity at an interface, or an unwanted interface layer can also give rise to enhanced recombination, because charge carriers cannot pass the barrier and thus recombine in the vicinity of the interface where they are accumulated. This recombination loss will again be voltage dependent, because the height of the barrier may be influenced by the applied voltage and thus assist the charge carriers in overcoming it. In the light IV, such a barrier can lead to a characteristic S-shape. Lower barriers result in a mere decrease in FF , as a result of an increase in R_s and a slight decrease in R_p , and are thus difficult to distinguish from defect rich interface regions.

Distinguishing between Loss Mechanisms

Dark- and illuminated IV measurements and spectral response measurements under different bias voltages usually allow to distinguish between the above listed loss mechanisms. It is important to notice that many of the parameters characterizing the solar cell circuit do change under illumination, so that a mere comparison of the dark- and light IV sometimes may lead to misinterpretations. For example, current limited shunts occur which are able to short-circuit the cell in the dark, but under illumination the photocurrent can still be collected. Often a relation between dark- and light IV is indeed found, however. A low parallel resistance observed in the dark indicating a shunting problem often results in a low FF and R_p of the solar cell under illumination, see [104].

Spectral response measurements eliminate the influence of shunt and series resistances and measure only the actual photocurrent, due to the lock-in technique

applied. Thus, a strong increase of the spectral response under a reverse bias voltage is directly linked to a voltage dependent photocurrent and thus recombination losses. On the other hand, if the voltage dependency of the photocurrent from spectral response measurements can explain a low R_p found in the light IV, then shunting problems can be excluded. Under a high reverse bias of -1 V to -2 V, in the absence of severe interface barriers or extremely high defect densities, one expects to extract virtually all photogenerated charge carriers, thus obtaining a measure of the optical quality of the solar cell.

4.4 Experimental

Amorphous silicon pin solar cells have been deposited on undoped and aluminum doped zinc oxide and Asahi U-type $\text{SnO}_2:\text{F}$. In the beginning of the project, this was done by RF (13.56 MHz) PECVD in the PASTA system, at a later stage by VHF (50 MHz) PECVD in the ASTER system. All silicon layers for the solar cells were deposited at 200°C, with exception of the p-layer in the PASTA system, which is deposited at 160°C. Prior to deposition, the substrates were cleaned ultrasonically in a soap solution, followed by rinsing in ultra pure water and cleaning in an ultrasonic ethanol bath. Microcrystalline silicon p-layers have been deposited in the ASTER system by VHF PECVD.

The pin solar cells have been deposited on a selection of the ETP zinc oxide samples as presented in chapter 3. For comparison, at the same time solar cells have been prepared on the reference TCOs presented in 3.3. The choice of reference TCO was in each series the reference TCO used in the Utrecht Solar Energy Laboratory at the time of sample preparation, as displayed in the total transmittance and haze spectra in chapter 3.

The microcrystalline p-layers were characterized by UV-VIS spectroscopy in the RT-mini set-up. The electronic states in the silicon layers are simulated by the OJL model [105]. Optical parameters and thickness of these thin layers were determined following the procedure presented in [106] and described in more detail in [107]. The crystallinity of the layers has been evaluated by Raman spectroscopy. From temperature dependent dark conductivity measurements, the dark conductivity at room temperature and its activation energy have been determined.

Light current-voltage (I/V) characteristics of the solar cells were measured under 100 mW/cm² AM 1.5 Global illumination using a Wacom dual source solar simulator. The dark IV characteristics were recorded with the same set-up, with the cells placed in a dark box. Spectral response measurements were performed in order to get more detailed information on the photocurrent generation character-

| | Asahi-U type I | Asahi-U type II | FZJ ZnO:Al type I | FZJ ZnO:Al type II |
|-------------------------------------|-------------------|--------------------|----------------------|-----------------------|
| Efficiency (IV) [%] | 9.6 | 9.3 | 8.3 | 8.1 |
| J_{sc} (IV) [mA/cm ²] | 16.2 | 15.5 | 15.7 | 15.7 |
| V_{oc} [V] | 0.82 | 0.83 | 0.83 | 0.84 |
| FF | 0.73 | 0.72 | 0.64 | 0.62 |
| R_s [Ωcm^2] | 4.3 | 4.6 | 7.0 | 8.2 |
| R_p [Ωcm^2] | 1462 | 1671 | 981 | 667 |

Table 4.1: Solar cell parameters of a-Si:H pin solar cells on two types of Asahi-U SnO₂:F and two types of ZnO:Al from Forschungszentrum Jülich (FZJ).

istics (or external collection efficiency (ECE)) of the cells. It has to be mentioned that during the course of this research the calibration of both, solar simulator and spectral response set-up have been improved substantially. The solar simulator calibration is now performed using solar cells calibrated at the National Renewable Energy Laboratory (NREL) in Golden, Colorado, USA. The calibration of the spectral response detector is made with respect to a photodetector calibrated at the Dutch national standards laboratory NMI.

Two solar cells have been prepared for transmission electron microscopy (TEM) analysis following the method described in [26], and inspected with a Tecnai 12 microscope in bright field configuration.

Microcrystalline silicon solar cells have been deposited by RF PECVD in the high power high pressure depletion regime as described elsewhere [23], and characterized, at the Forschungszentrum Jülich, Germany.

4.5 a-Si pin Cells on Reference Substrates

In this section, solar cells deposited on the the reference TCOs (see section 3.3) are described. Figures 4.6 and 4.7 show the IV and spectral response measurements, and Table 4.1 displays the corresponding solar cell parameters.

The comparison of the two Asahi TCOs shows that the type I with higher haze results in a higher short circuit current, while maintaining the high V_{oc} and FF obtained on type II. The main difference in spectral response is observed between 600 and 700 nm, where the higher haze of the type I TCO leads to more efficient light trapping manifested in the absence of interference fringes in the ECE spectra.

The cells on both ZnO:Al samples from FZJ suffer from low fill factors compared

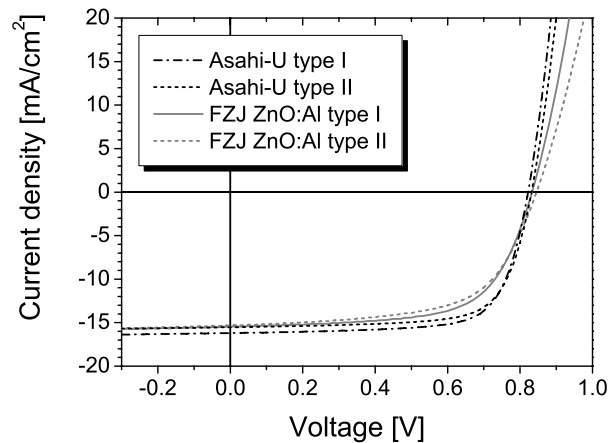


Figure 4.6: Light I-V curves of a-Si:H pin solar cells on two different types of Asahi-U $\text{SnO}_2\text{:F}$ and two types of ZnO:Al from Forschungszentrum Jülich (FZJ).

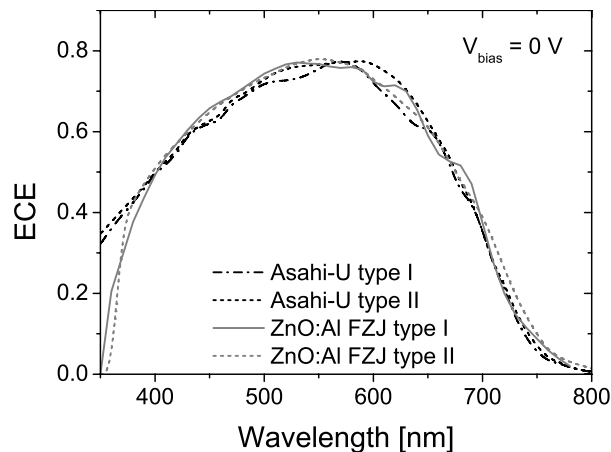


Figure 4.7: External collection efficiency curves of a-Si:H pin solar cells on two different types of Asahi-U $\text{SnO}_2\text{:F}$ and two types of ZnO:Al from Forschungszentrum Jülich (FZJ).

to cells on Asahi-U of 0.64 and 0.62 for type I and II, respectively, compared to values of 0.72 and 0.73 obtained on Asahi. This is attributed to a contact barrier at the ZnO/p interface [82] and can be overcome by the insertion of a microcrystalline silicon p-layer at the TCO/p interface [108] as will be described in section

4.6.

In spite of the substantially higher haze and comparable (type I) or even higher (type II) transmittance of the ZnO:Al samples (Figure 3.1), the solar cells do not exhibit higher short circuit currents than the cells on Asahi-U. For the type I ZnO:Al, this is attributed to the angular distribution of the scattered light, showing less efficient scattering into larger angles as compared to Asahi U-type [79,81]. The cell on type II ZnO:Al from FZJ, in addition to this effect, suffers from a severe collection problem which can be overcome by the insertion of a microcrystalline silicon p-layer at the TCO/p interface as described in 4.6. With such an optimized p-layer design, the short circuit current density for cells on the type II ZnO:Al can be increased by more than 1 mA/cm^2 (not shown), indicating the high light trapping potential of this TCO resulting from its remarkably high haze and transmittance.

4.6 The ZnO / p-Layer Interface

The reduced fill factor of a-Si pin cells on ZnO:Al has been reported before [109–111]. The Jülich group ascribed the problem to an electrical contact barrier at the TCO / a-SiC:H p-layer interface [112] and solved it by implementing a microcrystalline Si layer [109,108,113]. Others [114,110] found that the incorporation of metal and oxygen impurities originating from the TCO into the a-Si i-layer leads to a defective p / i interface region reducing the FF and V_{oc} of the solar cell. Also Hegedus *et al.* [115] found no evidence for a contact barrier between sputtered ZnO:Al and p-type a-SiC:H, and speculated that the low FF is due to an increased recombination as a result of a structurally or chemically different p/i region. As pointed out by Hegedus *et al.* [115], most publications report only on light I-V characteristics where it is difficult to distinguish between contact resistance and recombination losses. The Jülich group presented dark I-V curves for their cells [116], but in that case still a too thick, non-optimized $\mu\text{c-Si}$ p-layer was used, resulting in current and voltage losses in the solar cells.

Here, the band diagram of the TCO / p junction is described, and the influence of the work function of the TCO on this contact. After some results on the development of highly doped, thin microcrystalline p-layers by VHF PECVD, solar cells with an improved p-layer design implementing such a microcrystalline p-layer on magnetron sputtered and texture-etched ZnO:Al from FZJ are presented. Dark- and light I-V characteristics are taken into account for the case of an optimized microcrystalline p-layer inserted between ZnO:Al and a-SiC:H.

4.6.1 The TCO / p Interface

In general, due to the n-type character of all TCOs used as front electrode in thin-film silicon solar cells, at the TCO / p interface a Schottky barrier in reverse direction to the built-in field of the solar cell is established [117], see Figure 4.8. Due to the far higher density of charged states in the TCO, nearly the full depletion region is situated in the p-layer.

In the case of fluorinated tin oxide, a highly boron doped a-SiC:H p-type layer is sufficient to decrease the width of the depletion region in the p-type layer as to allow effective current transport through this barrier by tunneling [119].

As the work function ϕ_{TCO} of ZnO is generally lower than for $\text{SnO}_2\text{:F}$, the barrier ϕ_B at the ZnO / p interface is higher, and the depletion region in the p-layer becomes consequently wider [120]. This effect is enhanced, if due to the p-layer deposition conditions, the ZnO surface is chemically reduced [118]. A higher density of oxygen deficiencies in the ZnO leads to a decrease in work function and thus to an increased barrier height and depletion width at the TCO / p interface [121]. Therefore, microcrystalline p-layers with far higher concentrations of active dopants compared to amorphous p-layers [12] are often required to decrease the barrier width and allow low-resistive tunnelling transport through the TCO / p interface [108,120]. On the other hand, conductive ZnO layers with a higher work function have been obtained enabling an ohmic, low-resistive contact with a sufficiently high boron doped a-SiC:H p-layer [111]. It is concluded that the different work functions of the ZnO layers used by different groups may explain the contradictory findings on the presence of a contact barrier at the ZnO / a-SiC:H p-layer interface.

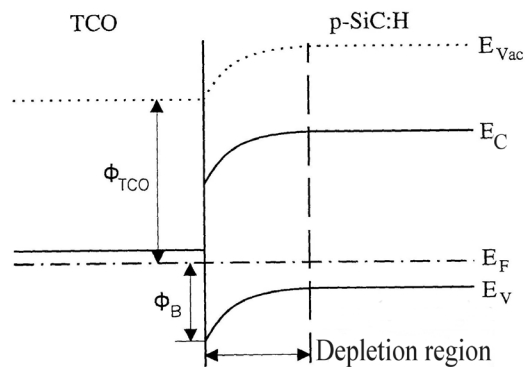


Figure 4.8: Band diagram of a TCO / a-SiC:H p-layer contact [118].

4.6.2 Development of Microcrystalline Silicon p-Layers

In this section the development of very thin (< 20 nm) microcrystalline silicon ($\mu\text{c-Si}$) p-layers by VHF (50 MHz) PECVD for the application as ZnO/p buffer layers in a-Si pin solar cells is described.

The nucleation of thin microcrystalline silicon films is very sensitive to substrate and plasma conditions [122,123], and the presence of boron as a dopant additionally inhibits the nucleation of the growth of crystallites [124]. On the other hand, a high trimethylboron (TMB) flow during deposition is needed for high effective dopant concentrations in the film. The VHF PECVD technique generally leads to an earlier nucleation with a higher density of nucleation sites compared to RF PECVD [125]. For the deposition of pin solar cells, the substrate temperature during the silicon deposition should generally be kept low to avoid damage to the TCO. Therefore, starting from deposition conditions used for reference $\mu\text{c-Si}$ p-layers at a substrate temperature of 250°C [126], the deposition temperature was lowered to 200°C to match the deposition temperature for the intrinsic and n-doped layers. Goal was the development of highly doped thin microcrystalline Si films. For a thickness of 20 nm, such films are characterized by a crystalline signature in their Raman spectrum, high dark conductivity around $0.03 \Omega^{-1}\text{cm}^{-1}$, and a low activation energy of the dark conductivity below 0.06 eV [12].

Variations in total flow, TMB flow, hydrogen dilution of the source gases, VHF power, and deposition pressure have been performed. At a given hydrogen dilution, the TMB flow has the most significant influence on the obtained layer properties. Figure 4.9 shows the Raman spectra of a series of approximately 20 nm thin $\mu\text{c-Si}$ p-layers deposited with TMB flows increasing from 0.05 to 0.20 sccm. Note that these gas flows are for the used mixture of 2% TMB diluted in H_2 . The plots are scaled to the peak around 520 cm^{-1} , representing the transverse optical (TO) vibration mode of the crystalline part of the material. Thus, a higher shoulder around 480 cm^{-1} , representing the TO vibrations of the amorphous part, in this figure indicates a lower crystalline fraction of the material. It is clear that with increasing TMB flow, the crystallinity of the material decreases. The layer deposited at the highest TMB flow in this series shows no crystalline signature at all. Due to the high amorphous background signal originating from the glass substrate, a small crystalline fraction below 10 % may still be present in this film, which cannot be resolved in the Raman spectrum. The resulting electrical properties of the layers are shown in Figure 4.10. With increasing TMB flow up to 0.15 sccm, the dark conductivity increases as a result of a higher concentration of active dopants leading to a lower activation energy of the dark conductivity. The

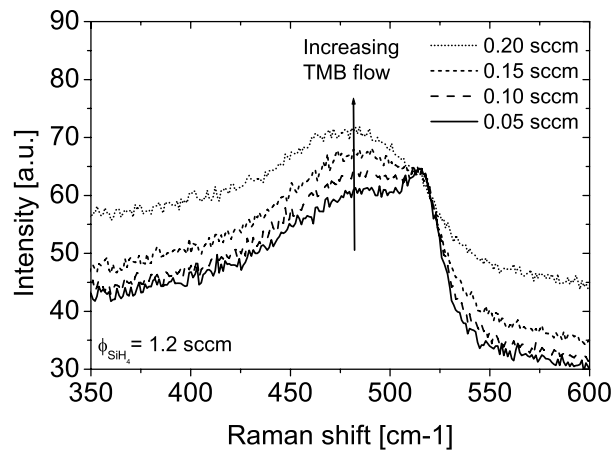


Figure 4.9: Raman spectra of thin (20 nm) microcrystalline silicon p-layers deposited with different flows of the TMB precursor (2% TMB in H_2).

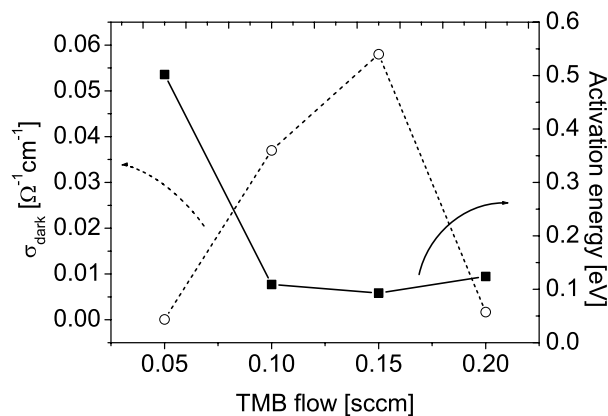


Figure 4.10: Dark conductivity and activation energy of thin (20 nm) microcrystalline silicon p-layers deposited with different flows of the TMB precursor (2% TMB in H_2).

high dark conductivity obtained for the layer deposited at 0.15 sccm TMB indicates that in spite of the decreased crystalline fraction of this material, the doping efficiency is still high, and the crystallinity is sufficient to allow transport by percolation. While theoretical considerations based on geometrical models predict that percolation takes place only in materials with crystalline fractions above

| Parameter | Value |
|-----------------------|----------|
| SiH ₄ flow | 1.2 sccm |
| TMB (2 % in He) flow | 0.2 sccm |
| H ₂ flow | 150 sccm |
| VHF power | 15 W |
| chamber pressure | 1.1 mbar |

Table 4.2: Optimized recipe for thin $\mu\text{c-Si}$ p-layers.

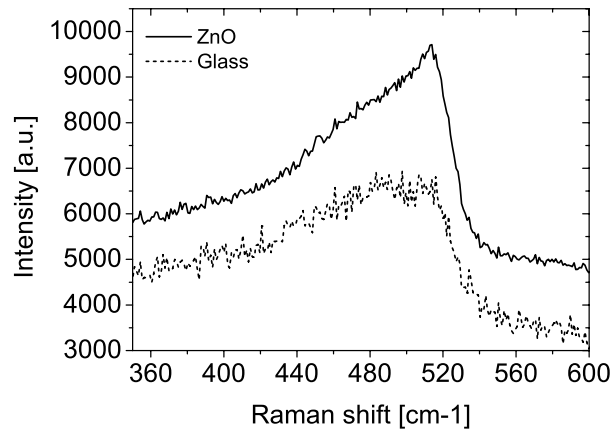


Figure 4.11: Raman spectra of thin (20 nm) microcrystalline silicon p-layers on ETP ZnO and glass substrates.

33%, Gordijn *et al.* found experimentally that the percolation threshold for thin μc p-layers can be at a Raman crystalline ratio as low as 15% [126]. At the highest TMB flow, a high activation energy and low dark conductivity are observed. This indicates that the current transport takes place through amorphous material, which is only weakly doped due to the low doping efficiency. Also from these conductivity measurements, the presence of a small crystalline fraction in the material cannot be excluded. Fine tuning of the deposition parameters lead to the optimized recipe for the deposition of thin $\mu\text{c-Si}$ p-layers at 200°C, see table 4.2.

For an 18 nm thin film, a high dark conductivity of $0.39 \Omega^{-1}\text{cm}^{-1}$ and a low activation energy of 0.065 eV have been achieved. The deposition rate for this film is 0.4 \AA/s . The influence of the substrate on the nucleation of the film is illustrated in Figure 4.11. On zinc oxide, a higher crystallinity is obtained. Bailat *et al.* similarly observed that on LPCVD deposited zinc oxide the nucleation occurs earlier than on glass [127]. Vallat-Sauvain *et al.* [128] even reported on incuba-

tion free growth of p-type microcrystalline silicon on [102] oriented zinc oxide, and attributed this to the good lattice matching with [220] oriented silicon. On the other hand, Luysberg *et al.* [129] found that the nucleation of microcrystalline n-layers on texture-etched ZnO:Al was similar to the growth on glass substrates. Apart from the lattice matching and chemical properties of the substrate surface, also the conductive character of the ZnO in contrast to the isolating glass substrates may play a role for the nucleation of the microcrystalline silicon p-layer. As the substrate surface is electrically connected to the grounded substrate holder, a conductive substrate can effectively decrease the distance between the powered electrode and the grounded substrate holder by as much as the substrate thickness (0.7 - 2 mm). This may lead to changes in the properties of the plasma such as the plasma sheath width.

In conclusion, thin microcrystalline p-layers with state-of-the-art properties have been obtained by VHF PECVD on glass. These layers are even more crystalline when deposited on zinc oxide. The implementation of such films as buffer layers at the ZnO / p⁺ contact in a-Si pin solar cells is described in the next section.

4.6.3 Microcrystalline Silicon p-Layers in pin Solar Cells on ZnO:Al

When using a microcrystalline p-layer in contact with a zinc oxide front electrode, a buffer has to be implemented at the interface between $\mu\text{c-p}$ and amorphous i-layer of the solar cell to avoid excessive recombination losses due to the high defect density and low band gap of the $\mu\text{c-p}$ layer. These properties of the p-layer would otherwise enhance the Shockley-Read-Hall recombination. To prevent electrons from reaching the μc p-layer, an intrinsic wide-gap layer like silicon carbide or wide-gap amorphous silicon deposited at low substrate temperature around 100°C have been applied [123]. In this case, the built-in field of the pin diode is formed by a 20 nm thick microcrystalline p-layer. Wieder [108] experimentally found that cells with a double p-layer consisting of an even thinner microcrystalline p-layer mainly functioning as contact buffer at the ZnO / p interface, and an a-SiC:H p-layer in contact with the intrinsic a-Si layer to built up the field, reach higher efficiencies. This has also been confirmed by simulations [130].

We therefore decided to implement such a double p-layer in a-Si pin cells on texture-etched ZnO:Al. This same double p-layer design also allowed us to achieve high open circuit voltages of 1.76 V in a-Si / a-Si tandem pin solar cells with a microcrystalline p-layer in the tunnel-recombination-junction [131]. We

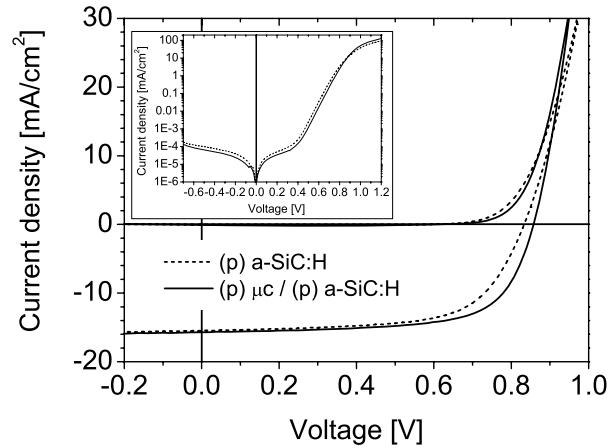


Figure 4.12: Dark and light I-V curves of a-Si:H pin solar cells on texture-etched ZnO:Al with a single 8 nm a-SiC:H p-layer, and a double p-layer consisting of 5 nm p-type μ c-Si and 6 nm (p) a-SiC:H.

found that thicknesses of 5 nm and 6 nm for the microcrystalline and amorphous SiC:H films, respectively, lead to a significant improvement in fill factor and V_{oc} of single junction a-Si pin cells on ZnO:Al, without sacrificing solar cell current due to absorption losses in the buffer layer (see Table 4.3). As it is difficult to control the physical thickness of these thin films due to the variation of the growth rate during the film nucleation, the mentioned thicknesses have to be considered as nominal values deduced from the deposition rate determined from 20 nm thick films on glass substrates. When analyzing the I-V data (Figure 4.12 and Table 4.3) it becomes clear that the improvement in FF and V_{oc} is indeed due to an improved TCO/p contact, rather than a better diode quality. The dark I-V (see also the inset in Figure 4.12 for a semi-logarithmic plot) is shifted towards higher voltages with respect to the cell with only an a-SiC:H p-layer. This indicates a higher effective built-in field, probably due to the absence of a reverse field at the ZnO:Al/ μ c-p interface. The dark I-V curve exhibits also a lower series resistance, visible by a steeper slope in the linear plot, and a less pronounced bending in the semi-logarithmic plot at high positive voltages.

The diode quality factor is identical for both cells, and the slight improvement in dark saturation current for the cell with μ c-Si p-layer cannot cause any significant difference under AM 1.5 illumination. Thus, the here observed improvement in cell performance obtained upon the insertion of a microcrystalline p-layer at the TCO / p interface cannot be explained by an improved p/i interface with lower

| | a-SiC:H | $\mu\text{c-Si} / \text{a-SiC:H}$ |
|--------------------------------|----------------------|-----------------------------------|
| Efficiency [%] | 8.3 | 9.1 |
| J_{sc} [mA/cm ²] | 15.7 | 15.7 |
| V_{oc} [V] | 0.83 | 0.86 |
| FF | 0.64 | 0.68 |
| R_s [Ωcm^2] | 7.0 | 4.7 |
| R_p [Ωcm^2] | 981 | 919 |
| n | 1.45 | 1.45 |
| J_0 [mA/cm ²] | 3.0×10^{-9} | 1.4×10^{-9} |

Table 4.3: Dark and light I-V parameters of a-Si:H pin solar cells on texture-etched ZnO:Al with a single 8 nm a-SiC:H p-layer, and a double p-layer consisting of 5 nm p-type $\mu\text{c-Si}$ and 6 nm (p) a-SiC:H.

defect density compared to the case of a single a-SiC:H p-layer, as postulated in [110,115].

We conclude, in agreement with the publications of the Jülich group [82,23,109], that on the texture-etched ZnO:Al from FZJ, a considerable improvement of V_{oc} and FF is obtained as a result of a solution of the contact barrier problem obtained with only an a-SiC:H p-layer. The higher V_{oc} is a direct result of the higher built-in field. Note that R_p is not improved as a result of the better TCO/p contact. This indicates a collection problem in the cell which may also explain the difference between the highest obtained fill factor here (0.68) and the values between 0.71 and 0.74 published by the Jülich group [112,113,116].

4.7 a-Si pin Cells on Undoped ZnO Superstrates

In this section, the performance of amorphous silicon (a-Si) pin superstrate type solar cells deposited on undoped ETP CVD ZnO layers as presented in section 3.4 are described. All solar cells had a standard a-SiC:H p-layer as described in 2.1.2.

Already the first solar cell on a ZnO layer deposited by ETP CVD at 250°C demonstrated that this TCO is indeed comparable to Asahi U-type SnO₂:F, leading to solar cell efficiencies approaching 10%. A comparable efficiency of 9.6% with respect to 10.2% for the reference cell has been obtained. The light I/V curves (Figure 4.13) show that all solar cell parameters are only slightly lower than those of the cell on Asahi U-type TCO, with the largest difference in the fill factor (see

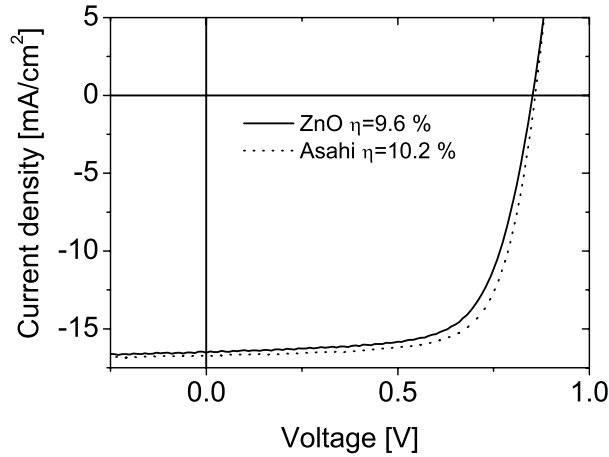


Figure 4.13: Light I-V curves of a-Si:H pin solar cells on a ZnO layer deposited by ETP CVD at 250°C, and on Asahi U-type SnO₂:F.

| | ETP ZnO | Asahi U |
|------------------------------------|---------|---------|
| Efficiency [%] | 9.6 | 10.2 |
| J_{sc} [mA/cm ²] | 16.5 | 16.7 |
| V_{oc} [V] | 0.85 | 0.86 |
| FF | 0.68 | 0.71 |
| R_s [Ω cm ²] | 5.9 | 5.1 |
| R_p [Ω cm ²] | 1180 | 1860 |

Table 4.4: Solar cell parameters of a-Si:H pin cells on a ZnO layer deposited by ETP CVD at 250°C, and on Asahi U-type SnO₂:F.

also Table 4.4). The high spectral response especially at long wavelengths (Figure 4.14) of the solar cell on ZnO, equivalent to the reference cell, indicates very effective light trapping in the device due to optical scattering at the rough ZnO/a-Si interface. To check the reproducibility of the obtained results, and to test the application of undoped ZnO films deposited in a wider substrate temperature range from 300°C down to as low as 150°C, series 2 of undoped ZnO samples deposited at different temperatures as described in section 3.4 was applied in a-Si pin solar cells. The corresponding IV data is shown in Table 4.5, and Figure 4.15 shows the external collection efficiency curves. In Table 4.5 one notes a large deviation between the short circuit current densities determined by I-V and spectral response

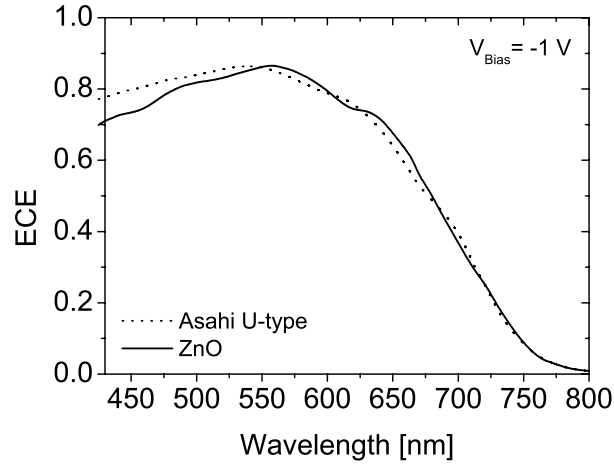


Figure 4.14: External collection efficiency curves of a-Si:H pin solar cells on a ZnO layer deposited by ETP CVD at 250°C, and on Asahi U-type SnO₂:F.

| | 150°C | 200°C | 250°C | 300°C | Asahi U |
|--------------------------------------|-------|-------|-------|-------|---------|
| Efficiency (IV) [%] | 8.9 | 9.5 | 9.5 | 9.1 | 9.6 |
| J_{sc} (IV) [mA/cm ²] | 17.9 | 18.4 | 18.5 | 17.9 | 18.9 |
| V_{oc} [V] | 0.76 | 0.79 | 0.79 | 0.79 | 0.75 |
| FF | 0.66 | 0.65 | 0.65 | 0.64 | 0.68 |
| R_s [Ω cm ²] | 5.9 | 6.4 | 6.7 | 7.4 | 4.2 |
| R_p [Ω cm ²] | 1180 | 1090 | 1150 | 830 | 1440 |
| J_{sc} (ECE) [mA/cm ²] | 14.4 | 14.3 | 14.4 | 14.5 | 14.0 |
| Efficiency (ECE) [%] | 7.2 | 7.4 | 7.4 | 7.4 | 7.1 |

Table 4.5: Solar cell parameters of a-Si:H pin cells on ZnO layers deposited by ETP CVD between 150°C and 300°C, and on Asahi U-type SnO₂:F.

(ECE) measurements. This is mainly attributed to the fact that the solar simulator was not yet calibrated properly when these measurements were done. Usually, the current density from spectral response measurements is around 10% lower than the value obtained from IV measurement. This discrepancy is attributed to several phenomena, which all have their origin in the fact that in the spectral response measurements only a small fraction in the center of the cell is illuminated, while in the I-V measurements even the area outside the solar cell is exposed to light.

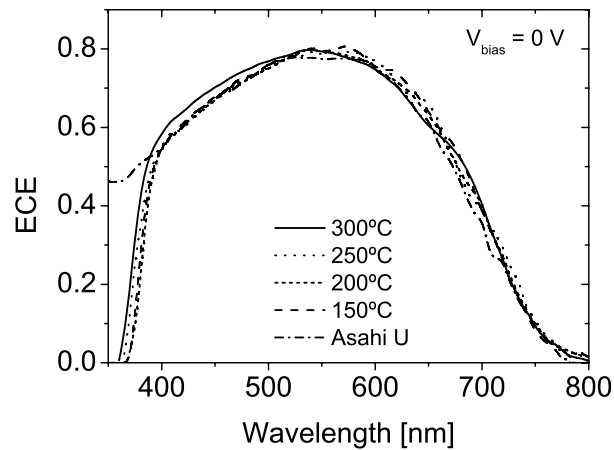


Figure 4.15: External collection efficiency curves of a-Si:H pin solar cells on ZnO layers deposited by ETP CVD between 150°C and 300°C, and on Asahi U-type SnO₂:F.

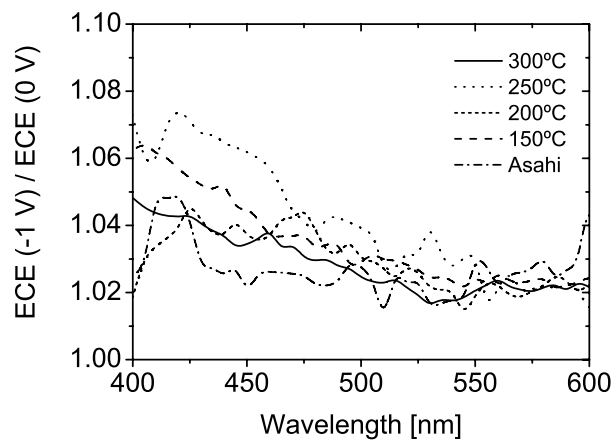


Figure 4.16: Relative change in external collection efficiency upon application of -1 V bias voltage for a-Si:H pin solar cells on ZnO layers deposited by ETP CVD between 150°C and 300°C, and on Asahi U-type SnO₂:F.

The definition of the solar cell area by the metal back electrode is not sharp. In I-V measurements, current generated in the proximity of the contact area can still be collected through lateral conduction in the n-layer. Due to the high resistance of the n-layer, in practice only current generated in distances around 100 μm con-

tribute to the measured short circuit current. Sometimes the definition of the metal back electrode itself is not sharp due to bending of the shadow masks used in the evaporation. Then the area of the cell is effectively increased, leading to a higher current generation and thus higher J_{sc} under the assumption of a sharply defined metallization. An example of this can be seen in Table 4.5. It is striking that in the I-V measurements the J_{sc} of the cell on Asahi U is higher than on the ZnO samples, while it is lower in the ECE measurements. Probably the contact area of the cells on Asahi-U is slightly larger than on the ZnO samples. In addition to this, short wavelength response below 350 nm is not taken into account in the ECE analysis, which is typically around 0.2 mA/cm² on Asahi U-type TCO. Another effect which can explain a lower current deduced from spectral response measurements than from I-V measurements is the loss of light due to scattering of the incoming light to places outside the collection length of the solar cell. In I-V measurements this loss will be compensated by the part of the light entering the sample outside the defined area of the solar cell which is subsequently scattered into the solar cell. The same holds for light which is lost due to the wave guide effect of the glass/TCO stack as a result of multiple internal reflections as described in [61].

Due to the calibration issues, we tend to assume the ECE current density increased by 10% as the value best comparable to the other measurements presented in this thesis. The following discussion is therefore based on the differences observed in the current densities determined by ECE.

The results of the first solar cells on undoped ZnO deposited at a substrate temperature of 250°C have been reproduced, yielding solar cells with efficiencies again only slightly lower than cells on Asahi U-type SnO₂:F. Also on the ZnO superstrate electrodes deposited at lower temperatures of 150°C and 200°C solar cells with comparable performance have been obtained. The high spectral response of all solar cells observed in the long wavelength regime, equivalent to that for cells on U-type SnO₂:F, indicates also here effective light trapping due to optical scattering at the rough ZnO / a-Si interface. In agreement with the transmittance spectra in Figure 3.10, the solar cell on the 300°C ZnO has a higher spectral response in the blue part of the spectrum, mainly because of a higher transmittance of the TCO and a better anti reflection effect of the rougher ZnO/a-Si interface.

For longer wavelengths around 600 - 650 nm, a slightly lower response is observed for the cell on the 300°C ZnO, which can be explained by the lower transmittance of the TCO as a result of free carrier absorption. Reverse bias voltage dependent measurements of the spectral response confirm that these are indeed mainly optical effects. As visualized in Figure 4.16, at a relatively high bias of

-1 V the increase in photo carrier collection at 400 nm as a result of the applied field is only 5 to 10 %, and decreases rapidly towards longer wavelengths. The increase in blue response for the cell on the 150°C and 250°C ZnO is slightly larger indicating that these TCOs also induce a minor collection problem due to local recombination in the TCO/p/i region of the solar cell, which can be compensated by the external field.

Remarkably, the cells on all four ZnO samples deposited between 150°C and 300°C have a higher current than the cells on Asahi U-type. The observed trend of increasing haze with increasing temperature (Figure 3.10) is not found back in the spectral response of the solar cells. Obviously, the higher absorption losses in the 300°C ZnO layer compensate for its higher haze leading to better light trapping in the cell. As a result, the red light response is comparable for the cells deposited on ZnO, regardless of the deposition temperature of the ZnO. Variations in the thickness of the a-Si pin cells on the different substrates can also lead to small differences in the spectral response. Therefore, within the accuracy of the experiment, no further conclusions can be drawn from the remaining small differences between the spectra in Figure 4.15. The comparison between the cells on Asahi U-type, and the 300°C ZnO layer, however, is very interesting. Both TCOs exhibit comparable transmittance (see Figure 3.10). In spite of the significantly higher haze, the ZnO results only in slightly higher red response of the solar cell. This demonstrates that the scattering properties of the granular ETP ZnO are such that a higher haze is needed for the same red response compared to Asahi-U, comparable to the case of texture-etched ZnO:Al from FZJ [79,81].

A slightly lower fill factor is observed for the cells on ZnO in comparison to cells on Asahi U-type TCO. This is ascribed to a minor collection problem, as the ECE curves for the cells on ZnO and Asahi U-type unexpectedly coincide between 400 and 500 nm, while the transmittance of the ZnO samples (see Figure 3.10) is slightly higher in this wavelength regime, so that one would expect a higher spectral response for the cells on ZnO. Such a collection problem can also explain the slightly lower R_p of the cells on ZnO with respect to the cells on Asahi U-type SnO₂:F. Also a contact barrier at the TCO/p interface cannot be excluded which can contribute to the series resistance and thus decrease the fill factor of the cell (see section 4.6).

From these results we cannot conclude a significant difference in cell performance when the ZnO deposition temperature is lowered from 300°C to values as low as 150°C. The solar cell performance achieved on ZnO with columnar structure is comparable to cells on granular ZnO films. In this case, the granular film had a higher haze and lower transmittance compared to columnar films, which resulted in similar long wavelength response of the solar cells. For the LPCVD

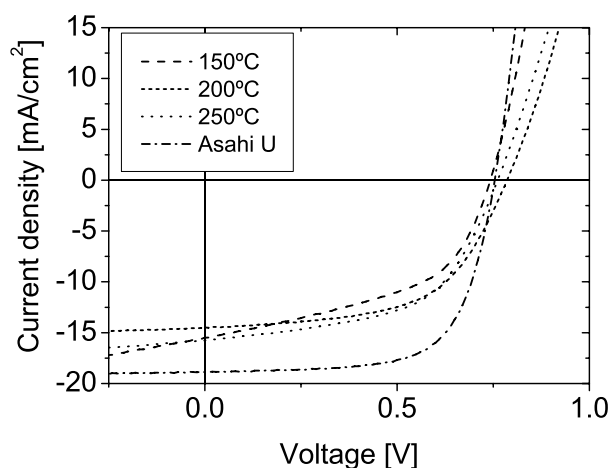


Figure 4.17: Light I-V curves of a-Si:H pin solar cells on ZnO:Al layers deposited by ETP CVD between 150°C and 250°C, and on Asahi U-type SnO₂:F.

process, purely columnar samples are preferred because there the facets of the [112] oriented grains form the textured surface [44]. The better the crystallinity of those layers, the rougher the obtained surface is, while at the same time the electrical properties improve [44]. Granular ZnO layers have the reputation to be chemically less stable due to their slightly lower density [42,43]. To our knowledge, however, no systematic studies have been performed on this topic, so that stability tests on ZnO layers and complete solar cells are necessary to finally conclude on the preferred structure of the ETP deposited ZnO layers.

In conclusion, solar cells with efficiencies comparable to Asahi U-type have been obtained reproducibly on ZnO deposited by ETP CVD. No significant difference has been observed in cell performance when increasing the deposition temperature for the ZnO, which is accompanied by a transition from columnar to granular growth. In principle, the solar cells on ETP ZnO can achieve higher current densities compared to Asahi U-type TCO as a result of higher haze and transmittance, but suffer from slightly lower fill factors as a consequence of a minor collection problem.

4.8 a-Si pin Cells on Doped ZnO:Al Superstrates

The influence of Al doping on the ZnO film properties has been evaluated in chapter 3.5. Here the performance as front TCO in amorphous silicon pin solar

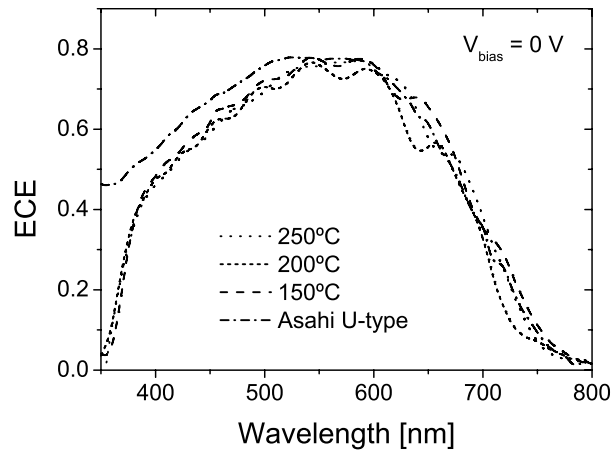


Figure 4.18: External collection efficiency curves of a-Si:H pin solar cells on ZnO:Al layers deposited by ETP CVD between 150°C and 250°C, and on Asahi U-type SnO₂:F.

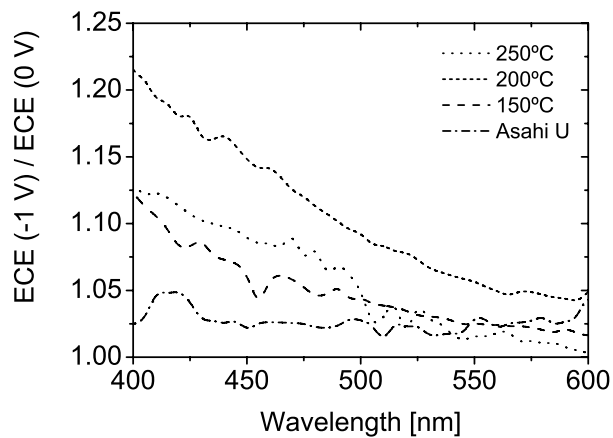


Figure 4.19: Relative change in external collection efficiency upon application of -1 V bias voltage for a-Si:H pin solar cells on ZnO:Al layers deposited by ETP CVD between 150°C and 250°C, and on Asahi U-type SnO₂:F.

cells of a selection of the described layers is investigated. In particular for the doped ZnO layers the definition of a deposition regime to achieve an optimized surface roughness and texture appeared to be important.

The first solar cells on doped ZnO:Al unexpectedly lead to considerably lower

efficiencies (around 6 %) than those on undoped ZnO and Asahi U-type. On the 300°C ZnO:Al sample all cells were even shunted. As can be seen from the I-V curves in Figure 4.17, for the working cells on ZnO:Al deposited between 150°C and 250°C the efficiency loss with respect to Asahi U-type (and thus to undoped ZnO) is due to a lower short circuit current as well as to a lower fill factor.

From spectral response measurements (Figure 4.18) one identifies two regimes of current loss with respect to the cells on undoped ZnO. The lower response of the cells on doped ZnO:Al at long wavelengths is due to the less efficient light trapping as a consequence of the lower haze of the TCOs. This is also seen in Figure 3.21. The loss in the short wavelength region needs further analysis. From voltage dependent spectral response measurements a severe photocarrier collection problem can be deduced as main loss mechanism here. In Figure 4.19 the relative increase in spectral response under a bias voltage of -1 V is shown to reach values as high as 20% at 400 nm for the cell on the 200°C ZnO:Al. Under negative bias voltage the external collection efficiency at short wavelengths comes close to the values obtained for the reference cell. Only a minor optical loss by higher reflectance from the flatter TCO/p interface can be identified, resulting from the observed interference fringes. In order to analyze these collection and shunting issues, cross sectional TEM pictures of the solar cells on the 200°C and 300°C doped ZnO:Al were taken. White areas indicating lower density of the amorphous silicon are clearly visible for the cell on the ZnO deposited at 200°C

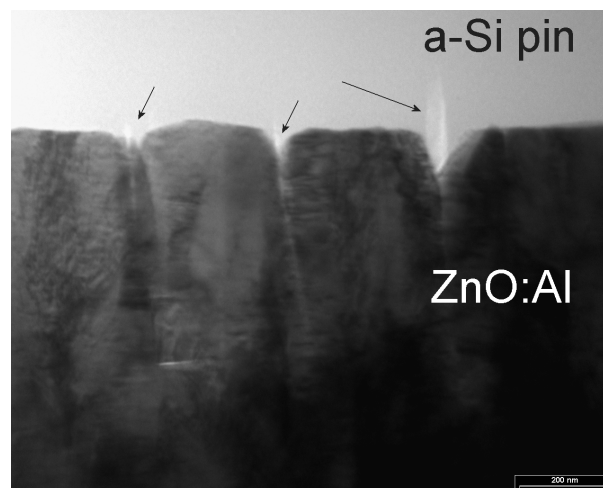


Figure 4.20: Cross sectional TEM of an a-Si pin solar cell on doped ZnO:Al deposited at 200°C.

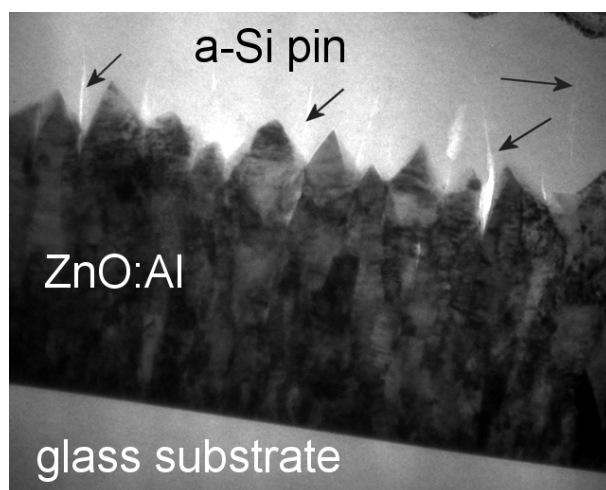


Figure 4.21: Cross sectional TEM of an a-Si pin solar cell on doped ZnO:Al deposited at 300°C.

(Figure 4.20) and even better at 300°C (Figure 4.21). It is obvious that these areas arise from steep trenches at the TCO surface. The growth of the amorphous silicon is CVD-like and thus predominantly normal to the TCO surface. This leads to collisions of growth zones starting from opposing TCO surfaces when the opening angles of the TCO roughness are small. When these opening angles are too small, the growth of dense amorphous silicon is hindered, leading to void rich regions which are characterized by a high defect density. Interestingly, as can be seen from the 200°C ZnO:Al this problem can occur also for a TCO surface which appears relatively flat in the SEM micrographs and exhibits low haze values. In TEM, this TCO is shown to have deep trenches (Figure 4.20).

The roughness of the TCO surface or the optical haze alone are thus not directly related to the observed collection and shunting issues. Rather the opening angle of the surface features and the presence of steep trenches (as in the case of the virtually flat 200°C ZnO:Al) determine the diode quality and thus the electrical properties of the solar cell, especially the fill factor and R_p .

Also a barrier at the TCO/p interface may be present here, which can explain part of the high R_s observed for the cells on doped ZnO:Al.

From the cells on ZnO:Al deposited at 300°C a relation between the observed shunting problem and the low density regions in the solar cells is proposed. In the upper right of Figure 4.21 one identifies such a white region extending through the entire thickness of the solar cells and thus connecting the ZnO:Al with the

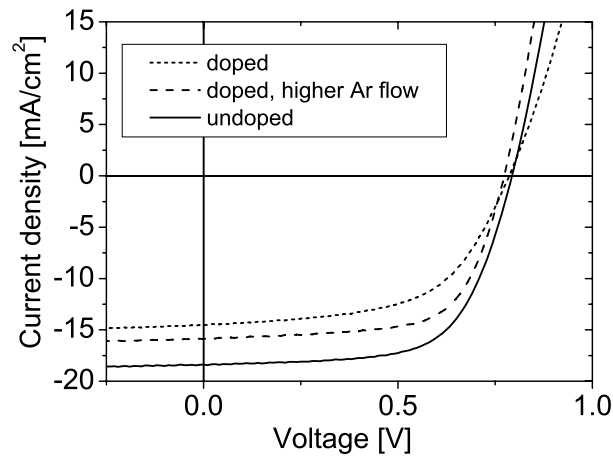


Figure 4.22: Light I-V curves of a-Si:H pin solar cells on undoped ZnO and doped ZnO:Al layers deposited by ETP CVD at 200°C.

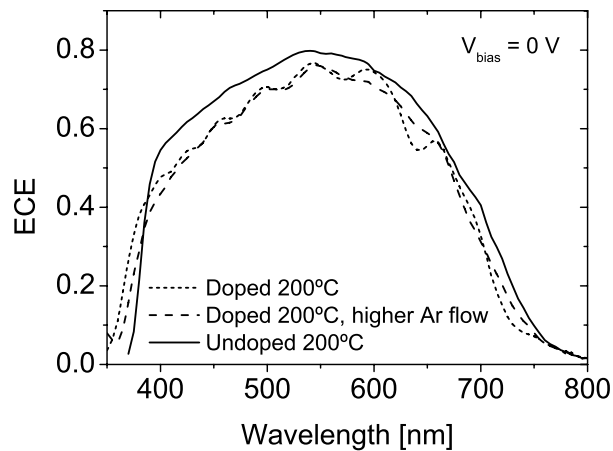


Figure 4.23: External collection efficiency curves of a-Si:H pin solar cells on undoped ZnO and doped ZnO:Al layers deposited by ETP CVD at 200°C.

back contact of the solar cell. These defect rich white regions [132] may result in shunting of the cell as a result of an ohmic current path along the defects (interdigitated voids). Also diffusion of impurities through this void-rich path might occur. Further studies are necessary here in order to get a more complete picture.

As described in section 3.5, in a next step, by increasing the Ar flow through

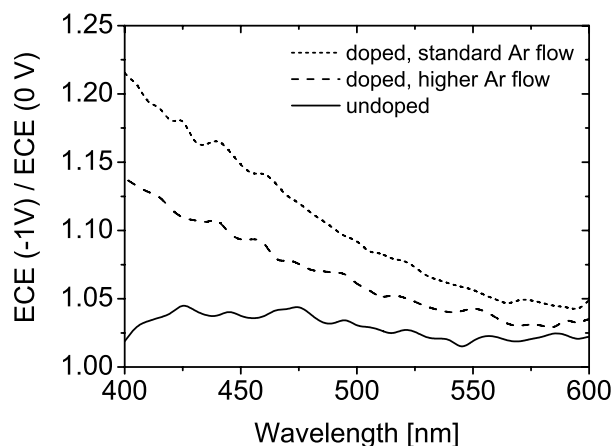


Figure 4.24: Relative change in external collection efficiency upon application of -1 V bias voltage for a-Si:H pin solar cells on undoped ZnO and doped ZnO:Al layers deposited by ETP CVD.

the cascaded arc we succeeded in adjusting the plasma conditions during the ZnO:Al deposition as to obtain doped ZnO:Al layers with granular structure, to avoid steep trenches, at a substrate temperature as low as 200°C (Figure 3.22). The obtained fill factors of the solar cells on this TCO are around 66%, comparable to those of the cells on undoped ZnO (Figure 4.22). It has to be mentioned that the light trapping in this cell is still not as efficient as in the cells on undoped ZnO, as can be seen from the slightly lower short circuit current. This is confirmed by spectral response measurements (Figure 4.23) demonstrating a lower response at longer wavelengths. The low response in the blue is attributed to both, optical and electrical losses. The bias dependent spectral response analysis (Figure 4.24) shows that the collection losses are lying in between the values found for the cells on the undoped ZnO and doped ZnO:Al deposited with the standard Ar flow. Thus, the increase in Ar flow during the ZnO:Al deposition helps to solve the collection and shunting problems encountered in the first solar cells on doped ZnO:Al deposited by ETP CVD.

Therefore, in a next series, the Ar flow through the cascaded arc for the ZnO:Al deposition was varied more systematically and up to higher values than for the previous sample. As described in 3.5.3, with increasing Ar flow the haze of the granular ZnO:Al layers increases. Note that the gas injection in the ETP deposition was different for this series.

Figure 4.25 shows the IV curves of the obtained solar cells, and in table 4.6

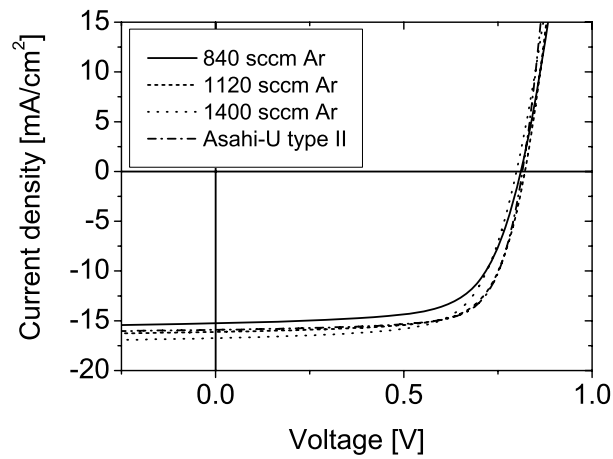


Figure 4.25: Light I-V curves of a-Si:H pin solar cells on doped ZnO:Al layers deposited by ETP CVD with different Ar flows through the cascaded arc and Asahi U-type SnO₂:F.

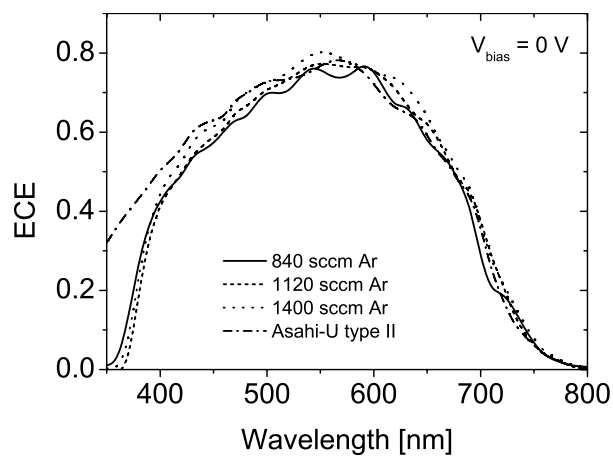


Figure 4.26: External collection efficiency curves of a-Si:H pin solar cells doped ZnO:Al layers deposited by ETP CVD with different Ar flows through the cascaded arc and Asahi U-type SnO₂:F.

the corresponding solar cell data is given. With increasing Ar flow for the ZnO:Al deposition, the short circuit current of the solar cells increases, which is explained by better light trapping as a result of the higher haze. This is confirmed by a

| | 840 sccm | 1120 sccm | 1400 sccm | Asahi-U type II |
|---|----------|-----------|-----------|-----------------|
| R_{\square} of TCO [Ω/\square] | 8 | 19 | 80 | 11 |
| Efficiency (IV) [%] | 8.1 | 9.3 | 9.1 | 9.4 |
| J_{sc} [mA/cm^2] | 15.1 | 16.1 | 16.7 | 15.9 |
| V_{oc} | 0.81 | 0.82 | 0.80 | 0.81 |
| FF | 0.67 | 0.70 | 0.68 | 0.73 |
| R_s [Ωcm^2] | 6.7 | 4.9 | 5.8 | 4.0 |
| R_p [Ωcm^2] | 1108 | 1374 | 1177 | 1860 |

Table 4.6: Solar cell parameters of a-Si:H pin cells on doped ZnO:Al layers deposited by ETP CVD with different Ar flows through the cascaded arc, and on Asahi U-type SnO₂:F.

higher red light response of the solar cells with increasing Ar flow (Figure 4.26). The blue response also increases with increasing Ar flow, which is predominantly ascribed to a better anti-reflection effect of the rougher ZnO:Al / a-Si interface. As presented in section 3.5.3, Figure 3.26, the ZnO:Al deposited at an Ar flow of 840 sccm exhibits higher total transmittance than the Asahi U-type reference and a comparable haze in the wavelength range between 600 nm and 800 nm. The solar cell on the 840 sccm Ar sample, however, shows a lower response between 630 nm and 720 nm as a result of a pronounced interference fringe. This indicates that also here the texture of the Asahi U-type TCO gives rise to better light trapping, probably due to the higher scatter intensities for large angles.

Interestingly, the optimum solar cell efficiency is not found for the cell with the highest short circuit current, but at the intermediate Ar flow. Both at the highest and at the lowest Ar flow, fill factor and open circuit voltage of the solar cells are lower. For the cell with the lowest Ar flow we suspect, as explained above for the first cells deposited on doped ZnO:Al, steep trenches at the TCO surface (see Figure 3.25) to be responsible for a defect-rich growth of the a-Si pin, at least in the interface region with the TCO. This can explain a lower fill factor as a result of recombination losses hindering charge carrier collection, mainly for the carriers generated in the vicinity of the p/i interface and thus predominantly by blue light. Generation and recombination in this defect rich interface region also leads to losses in V_{oc} . For the TCO deposited at the highest Ar flow, similar phenomena may play a role. In Figure 3.25 some vertical steps at the ZnO:Al surface stemming from protruding grains can be seen, which might induce defect-rich growth of the a-Si material. The lower fill factor, however, is mostly explained by the high resistivity of the TCO as a result of lower Al incorporation (see section

3.5.3), directly increasing the series resistance and thus the fill factor of the solar cell. Especially for the ZnO:Al deposited at the lowest Ar flow of 840 sccm, which exhibits the highest conductivity, a minor barrier at the TCO/p interface cannot be excluded.

In conclusion, optimizing the morphology of the doped ZnO:Al TCO by increasing the Ar flow through the cascaded arc enabled to surpass the initially encountered shunting and collection problems. The best solar cell on doped ZnO:Al has a comparable efficiency to the reference cell on Asahi-U, exhibiting a slightly higher current and slightly lower fill factor.

4.9 Microcrystalline Silicon Solar Cells

Due to the good performance of a-Si pin solar cells on the undoped ETP ZnO and the high transmittance at long wavelengths up to 1100 nm obtained for these TCOs, they appeared to be promising front electrode material for microcrystalline silicon solar cells, where light trapping is even more important than for amorphous silicon solar cells [66]. In this section, the results of the first solar cells with microcrystalline intrinsic absorber layers deposited on an undoped ETP ZnO superstrate are described in comparison to cells on texture-etched ZnO:Al from FZJ. Both TCO (similar to type I) and solar cell from FZJ were from standard depositions and naturally do not represent the highest achievable performance.

Figure 4.27 shows the spectral response of a microcrystalline silicon solar cell with an intrinsic absorber layer of 1.2 μm thickness deposited on ETP ZnO and texture-etched ZnO:Al from FZJ. The good light trapping properties and high transmittance of the ETP ZnO indeed lead to a high spectral response for long wavelengths, which is as high as for the cell on ZnO:Al from FZJ for the whole spectrum up to 1100 nm. Only for short wavelengths a lower response is obtained, which is attributed to the narrower band gap of the undoped ETP ZnO compared to the doped ZnO:Al from FZJ.

In Table 4.7 the I-V parameters of the solar cells are given. The cell on ZnO:Al from FZJ reaches a high efficiency of 8.5%, while the efficiency of the cell on ETP ZnO is 6.6%. As expected from the spectral response measurements, J_{sc} is only slightly lower for the cell on ETP ZnO. The main difference between the two cells lies in the low FF of only 0.61 obtained on ETP ZnO, while the cell on ZnO:Al from FZJ reaches a value as high as 0.73. This low fill factor is primarily due to the high sheet resistance of the TCO (around 15 Ω/\square), which has a higher influence here than in the case of the amorphous pin cells because of the larger size of 1 x 1 cm^2 and higher current densities of the microcrystalline silicon cells. It

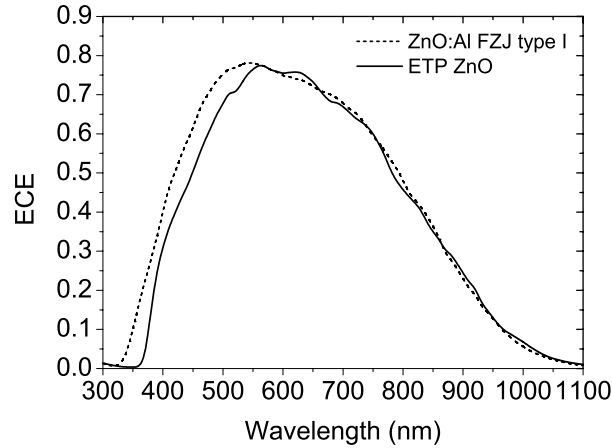


Figure 4.27: External collection efficiency curves of microcrystalline silicon pin solar cells on undoped ZnO deposited by ETP CVD at 200°C, and on texture-etched ZnO:Al type I from FZJ.

| | ETP ZnO | Texture-etched ZnO:Al |
|--------------------------------|---------|-----------------------|
| Efficiency [%] | 6.6 | 8.5 |
| J_{sc} [mA/cm ²] | 20.8 | 22.0 |
| V_{oc} [V] | 0.52 | 0.53 |
| FF | 0.61 | 0.73 |

Table 4.7: Solar cell parameters of microcrystalline silicon pin solar cells on undoped ZnO deposited by ETP CVD at 200°C, and on texture-etched ZnO:Al type I from FZJ.

is therefore difficult to judge about the suitability of the morphology of the ETP ZnO for microcrystalline silicon pin solar cells. The presence of too steep opening angles of the features at the TCO surface have been shown to be detrimental for the quality of microcrystalline silicon solar cells, because then defect rich regions originate from areas where crystalline grains growing from opposing surfaces collide [133–135]. A minor influence of the TCO / p contact region which was optimized for the ZnO:Al from FZJ in this run, may also be present. The slightly lower V_{oc} of 0.52 V in comparison to 0.53 V obtained on ZnO:Al from FZJ may be related to TCO/p contact issues as well as the morphology of the ETP ZnO.

In conclusion, microcrystalline silicon solar cells deposited on ETP ZnO benefit from the excellent light trapping properties and high transmittance of the TCO for long wavelengths up to 1100 nm. The high sheet resistance however gives rise to a low fill factor of 0.61 compared to a value of 0.73 obtained for the reference cell on texture etched ZnO:Al. Decreasing the sheet resistance by doping the ZnO or increasing the layer thickness without losing transmittance for long wavelengths as a result of free carrier absorption remains as a challenge for the development of ETP ZnO and ZnO:Al as front TCO for microcrystalline silicon solar cells.

4.10 Conclusions

The natively textured undoped ZnO films deposited by ETP CVD are highly suitable as a front electrode material for amorphous silicon pin solar cells. Solar cells with efficiencies comparable to cells on Asahi U-type reference TCO have been reproducibly obtained. No significant difference in the cell performance has been observed between cells on ZnO films with columnar and granular structure, which were obtained by an increase in the substrate temperature for the ZnO deposition from 150°C to 300°C. A higher haze is needed for the ZnO samples studied here than for Asahi U-type TCO in order to achieve comparable long wavelength response of the solar cells. This is attributed to the angular distribution of the scattered light which shows for large angles higher scattering intensities for the Asahi U-type TCO. In spite of this, the combination of higher haze and higher transmittance of the ETP ZnO resulted in slightly higher current densities than on Asahi U-type. A barrier at the TCO/p interface and minor collection problems may explain the slightly lower fill factors obtained for the cells on ETP ZnO.

Doping of the zinc oxide can improve the stability of the electrical properties of the TCO films. Initially incorporation of Al into the zinc oxide films lead to collection and shunting problems in the solar cells, probably due to steep trenches, sharp features and vertical steps at the TCO surface. By increasing the Ar flow through the cascaded arc, deposition conditions have been found as to obtain doped ZnO:Al layers with granular structure at a substrate temperature as low as 200°C, allowing for fill factors of the solar cells up to 0.70, comparable to cells on undoped ZnO. The best solar cell on doped ZnO:Al deposited by ETP CVD achieved an efficiency of 9.3% compared to 9.4% obtained on Asahi.

The potential barrier at the zinc oxide / p-layer interface for cells on ETP deposited ZnO and ZnO:Al needs further studies. As the losses due to such a contact barrier are significantly smaller than for the case of texture-etched ZnO:Al from

FZJ, dedicated experiments with optimized p-layers are necessary to separate recombination losses in the p/i interface region from TCO/p contact losses. These losses may well depend on the concentration of dopants and oxygen vacancies in the ZnO and ZnO:Al films.

Microcrystalline silicon solar cells deposited on ETP ZnO benefit from the excellent light trapping properties and high transmittance of the TCO for long wavelengths up to 1100 nm. The high sheet resistance however gives rise to a low fill factor of 0.61 compared to a value of 0.73 obtained for the reference cell on texture-etched ZnO:Al.

Comparison to Zinc Oxide Deposited by Other Techniques

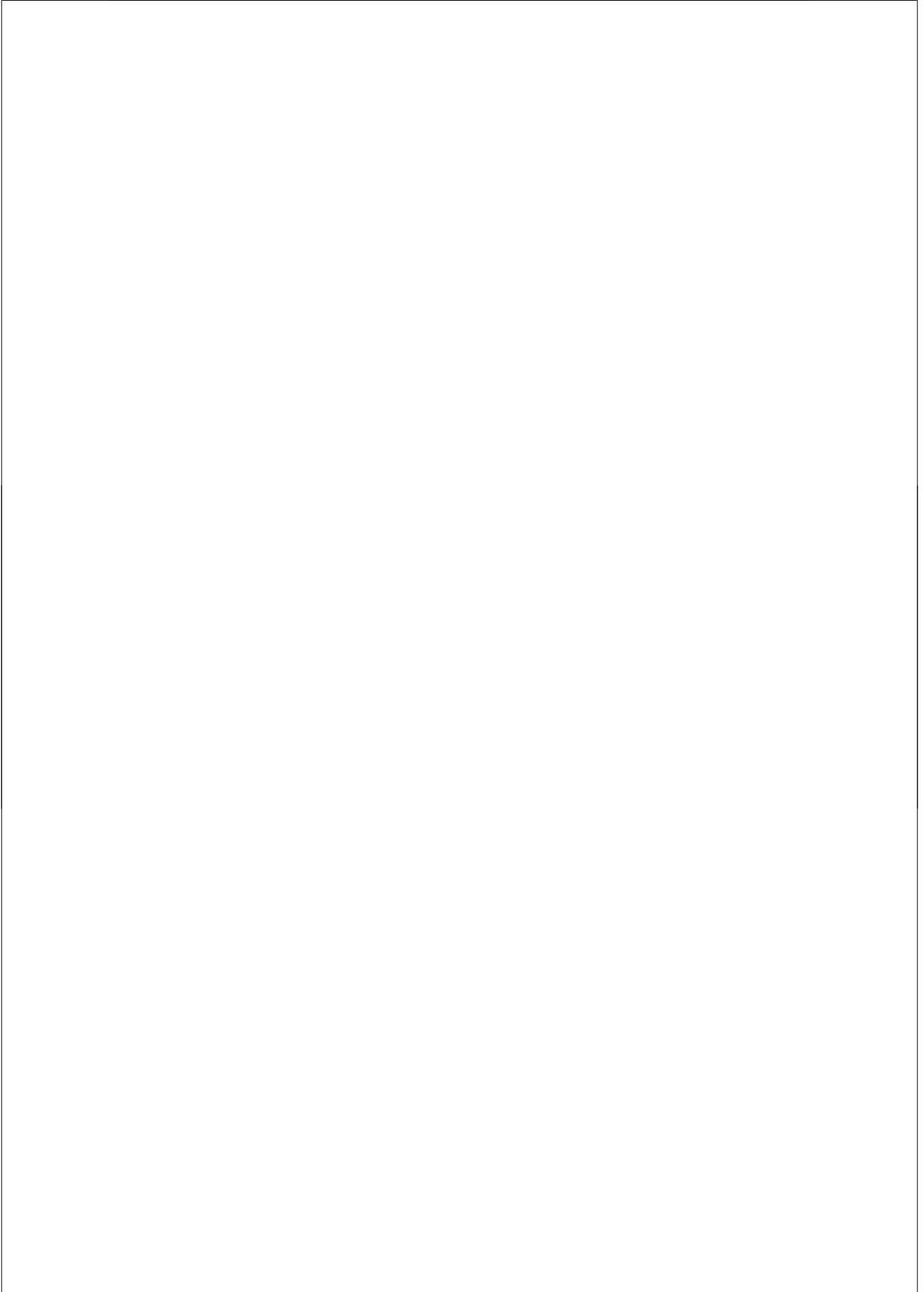
Other groups have deposited textured zinc oxide layers as front electrode for amorphous silicon pin solar cells successfully by different techniques.

The magnetron-sputtered ZnO:Al films from FZJ, that also served as reference material in this study, have to be textured by a post-deposition etch. For a-Si tandem solar cells, stable solar cell efficiencies of 9.2%, equal to cells on Asahi U-type TCO, have been achieved [136]. The sputter process allows for deposition rates of 0.4 nm/s for RF magnetron sputtering from a ceramic target [50], and up to 90 nm/s for mid-frequency reactive processes from metallic targets [137]. This TCO is, due to its high haze and transmittance in the near-infrared, especially suited for microcrystalline silicon solar cells [136].

Deposition techniques based on the metalorganic chemical vapor deposition (MOCVD) process have shown to be capable of producing natively textured zinc oxides which are highly suitable as front TCO for amorphous silicon pin solar cells. On annealed photo-assisted MOCVD deposited ZnO:B, Wenas *et al.* [138] achieved conversion efficiencies of 12.1% with cells optimized for initial efficiency and provided with an enhanced back reflector, compared to 12.6% obtained with a similar device structure on SnO₂:F. This discrepancy between performance of the cells on reference SnO₂:F and zinc oxide is comparable to the results obtained on ETP ZnO and ZnO:Al. The deposition rate of ZnO:B obtained by this MOCVD process is 0.9 nm/s, thus also comparable to the ETP technique. Improvements in the p-layer design lead to stable efficiencies of 8.7% (initial 9.7%) on small area (0.09 cm²) cells, even higher than on Asahi U-type [48]. Further development of this deposition technique to a step-wise process applying the atomic layer deposition technique enabled Sang *et al.* [46] to achieve ZnO:B layers with improved and more stable electrical properties. Decreasing the resistivity from $7 \cdot 10^{-3} \Omega\text{cm}$ to $5 \cdot 10^{-4} \Omega\text{cm}$ allowed for lower series resistance losses and thus better performance of larger cells (1 cm²) [48].

The Neuchâtel group has achieved excellent results with a-Si solar cells on MOCVD deposited ZnO:B [47]. As they use low deposition pressures of 0.5 mbar [44], the technique is often referred to as low pressure CVD (LPCVD) [65]. An a-Si single junction cell with 11.3% initial efficiency compared to 10.3% on Asahi-U has been presented [47]. Also a stable efficiency of 9% for an a-Si pin cell on LPCVD ZnO:B has been achieved, thus taking full advantage of the excellent light trapping properties of the TCO, enabling a high short circuit current density of 15.8 mA/cm² with a potentially more stable 250 nm thin intrinsic absorber layer [47]. The LPCVD process further has the advantage of high deposition rates above 2 nm/s [65]. Also this TCO is highly suited for microcrystalline silicon solar cells [44].

Thus, to compete with the currently most promising preparation techniques for zinc oxide as front TCO for thin-film silicon solar cells on industrial scale, namely sputtering with subsequent texture-etching [66], and LPCVD [65], future research on ETP zinc oxide has to be directed towards two issues. On one hand, fine tuning of the TCO properties and the solar cell device structure have to enable higher solar cell efficiencies than readily obtained on ZnO and ZnO:Al, also on more relevant cell sizes. The determination of an optimized surface texture allowing efficient light trapping in the solar cell while maintaining a high diode quality, the conductivity of the TCO, and the electrical properties of the TCO / p interface play a major role here. On the other hand, competitive deposition rates have to be achieved.



5 Fluorinated Tin Oxide by Atmospheric Pressure Chemical Vapor Deposition

5.1 Introduction

As described in chapters 2 to 4 of this thesis, zinc oxide prepared by various deposition techniques is a promising candidate as TCO material for thin-film silicon solar cells. However, efforts are still in the research stage, or at best development stage [66,65]. Currently fluorine doped tin oxide $\text{SnO}_2:\text{F}$ deposited by Atmospheric Pressure Chemical Vapor Deposition (APCVD) is still the standard superstrate electrode used for amorphous silicon pin solar cell production [33,139,140] in industry. The APCVD process has the advantage of very high deposition rates in the order of 10 nm/s, and it can be even applied during the cooling of the glass panes in a float glass production, thus saving energy cost for substrate heating [139]. Various metalorganic precursors have been used for the deposition of fluorine doped tin oxide layers for a number of applications, see [141,142,25] for an overview. Here $\text{SnO}_2:\text{F}$ layers deposited by APCVD from three different tin (Sn) precursors are compared as front TCO for amorphous silicon pin solar cells: tetramethyltin (TMT), monobutyltin trichloride (MBTC), and tin tetrachloride (TTC). Asahi U-type $\text{SnO}_2:\text{F}$, which is actually deposited from TTC [143] served as reference TCO. The influence of the Sn precursor on the electrical, optical and structural properties as well as the hydrogen plasma resistance of the resulting TCO layers have been studied. Finally, the $\text{SnO}_2:\text{F}/\text{glass}$ superstrates have been tested in amorphous silicon pin solar cells deposited by RF PECVD in order to assess their suitability as front TCO for this type of devices.

5.2 Atmospheric Pressure Chemical Vapor Deposition of Fluorinated Tin Oxide

As the main goal of this research was the characterization and testing of the TCOs in solar cells, only a short overview of the chemistry of tin oxide deposition from the precursors which were used here is given. Further details on these processes and a concise literature study covering also other precursors and their processes and chemistry can be found in [141].

The detailed reactions during APCVD in the gas phase, at the chamber walls and at the growing film surface depend very sensitively on the exact process conditions and the geometry of the deposition equipment. Therefore still most knowledge applied in industry comes from empirical testing. For TTC as precursor, there is little doubt that the reaction occurs mainly at the growing film surface:



As this reaction takes place rapidly at substrate temperatures as low as 250°C, the reactants must be mixed close to the substrate surface [142], otherwise the deposition takes mainly place at the reactor walls. It is a challenge to achieve uniform coatings at atmospheric pressure, as turbulent mixing of the reactants becomes necessary. Similar arguments hold for monobutyltin trichloride ($\text{Sn}(\text{C}_3\text{H}_7)\text{Cl}_3$, MBTC) [144].

If the tin precursor has an organic ligand, the reactants can be pre-mixed prior to dosing into the reaction chamber. For example tetramethyltin ($\text{Sn}(\text{CH}_3)_4$, TMT) does not react with oxygen below 400°C. Oxygen can be used instead of water here due to the absence of Cl in the precursor and thus no need to form HCl. The absence of Cl in the precursor makes the process also less toxic and corrosive.

5.3 Experimental

Sample Preparation

SnO_2 :F layers have been deposited on Corning 1737F glass by APCVD at TNO-TPD, Eindhoven, the Netherlands, in a Watkins Johnson WJ998 reactor from three different tin precursors: tetramethyltin (TMT), monobutyltin trichloride (MBTC),

| | TMT | MBTC | TTC |
|---------------------------------|-------|-------|-------|
| Belt speed [cm/min] | 3.5 | 2.0 | 2.5 |
| Belt temperature [°C] | 550 | 575 | 550 |
| Flow rate tin precursor [mol/s] | 0.058 | 0.038 | 0.024 |
| O ₂ / Sn | 47.3 | 18.7 | 0 |
| H ₂ O / Sn | 0 | 0 | 19.2 |
| F / Sn | 0.047 | 0.068 | 0.17 |
| CH ₃ OH / Sn | 0 | 0 | 0.13 |

Table 5.1: Experimental settings for the deposition of SnO_2 :F layers from three different Sn precursors by APCVD.

and tin tetrachloride (TTC). Additionally water, methanol, and hydrofluoric acid (HF) respectively trifluoroacetic acid (F_3CCOOH) for the MBTC sample were dosed. The exact deposition parameters are listed in Table 5.1 [145]. To determine the hydrogen plasma resistance of the TCO films, they were treated in the UHV system ATLAS, which is a replica of one of the deposition chambers of the ASTER system, equipped with a loadlock. Prior to the hydrogen treatment experiments, all chamber parts exposed to the hydrogen radicals during the treatment have been thoroughly cleaned by KOH etching or sand blasting in order to avoid deposition of species etched from the wall (chemical transport deposition [146]) onto the TCO surface. The treatment was performed for 2 minutes at 5 W VHF (50 MHz) plasma power, 40 sccm hydrogen flow, 0.15 mbar, and at a substrate temperature of 200°C. Amorphous silicon pin solar cells were deposited side-by-side on the three TCOs and Asahi U-type by RF (13.56MHz) PECVD in the UHV multichamber system PASTA.

Sample Characterization

The thickness of the deposited films was measured with a step profiler (Tencor R-10 Surface Profiler) after etching a step with HCl in the presence of Zn powder. The electronic properties of the $SnO_2:F$ samples were measured by 4 point probe and Hall (Phytech RH2010 Hall) measurements. The surface morphology was assessed by scanning electron microscopy (SEM) with a Philips SEM XL30 SFEG instrument. Optical transmittance before and after hydrogen plasma treatment and haze spectra were recorded by UV-VIS spectroscopy in a Perkin Elmer Lambda 2S spectrophotometer with integrating sphere. Angular resolved scattering experiment were performed with a HeNe laser at a wavelength of 632.8 nm. The solar cell performance was measured by dark and light IV under a Wacom dual source simulator calibrated to AM 1.5 global, and by spectral response analysis.

5.4 Results and Discussion

5.4.1 $SnO_2:F$ Layers

Three $SnO_2:F$ layers were deposited on Corning 1737F glass from the different tin precursors. Deposition parameters were chosen such that the thickness and sheet resistance were in the range of the Asahi U-type TCO. The thickness and electrical parameters of the layers are listed in Table 5.2. It can be seen that the

| | TMT | MBTC | TTC | Asahi U |
|--|------|------|------|---------|
| Thickness [nm] | 750 | 990 | 730 | 900 |
| Sheet resistance [Ω/\square] | 7.2 | 7.0 | 5.5 | 8.7 |
| Resistivity [$10^{-4} \Omega\text{cm}$] | 5.4 | 6.9 | 4.0 | 7.8 |
| Mobility [$\text{cm}^2\text{V}^{-1}\text{s}^{-1}$] | 29.7 | 18.6 | 31.6 | 37.0 |
| Carrier concentration [10^{20}cm^{-3}] | 3.9 | 4.8 | 5.0 | 2.2 |

Table 5.2: Thickness and electrical properties of the $\text{SnO}_2\text{:F}$ layers deposited from three different Sn precursors, and Asahi U-type.

MBTC sample has a significantly lower electron mobility than the other samples, and that all TCOs deposited in this study have a higher carrier concentration than the Asahi U-type $\text{SnO}_2\text{:F}$. To achieve a reasonable sheet resistance of $6.9 \Omega/\square$, the MBTC sample had to be deposited to a thickness of 990 nm comparable to the Asahi U-type (900 nm), while the TMT and TTC samples already at a thickness of 730 to 750 nm exhibit low sheet resistances of respectively 5.4 and $4.0 \Omega/\square$.

In Figure 5.1 SEM micrographs taken from the four TCO layers are displayed. While the TMT sample shows only small surface features around 100 nm in size, the MBTC and TTC samples has larger features up to $1 \mu\text{m}$, comparable to the pyramidally shaped Asahi U-type surface. When using TTC it is expected to obtain a film comparable to Asahi U-type, which is also deposited from TTC. The deposition of tin oxide from MBTC is a patented method to produce extraordinarily flat films [144]. Gordon *et al.* [78] published rough films obtained by APCVD from TMT. Both observations from literature are in contrast to our findings. It has to be mentioned that in the latter study bromotrifluoromethane was used as precursor for fluorine doping. The presence of a dopant is capable of changing the chemistry in the gas phase as well as at the growing film surface. This again shows that in addition to the precursor choice, many other parameters have a significant influence on the resulting TCO. The three tin oxide films investigated here cannot cover the full regime of deposition conditions accessible with the three precursors. The obtained TCOs are certainly interesting to study their suitability for a-Si pin solar cells.

The optical characteristics of the layers before and after a severe hydrogen plasma treatment are shown in Figure 5.2. It can be seen that the small surface roughness of the TMT sample results in nearly zero haze. The rough surfaces of the MBTC and TTC samples lead to considerable light scattering. The Asahi TCO shows the highest haze, and also the highest total transmittance. The MBTC sample has the lowest transmittance of the investigated layers, indicating high absorption losses. All $\text{SnO}_2\text{:F}$ samples deposited in this study have a higher carrier

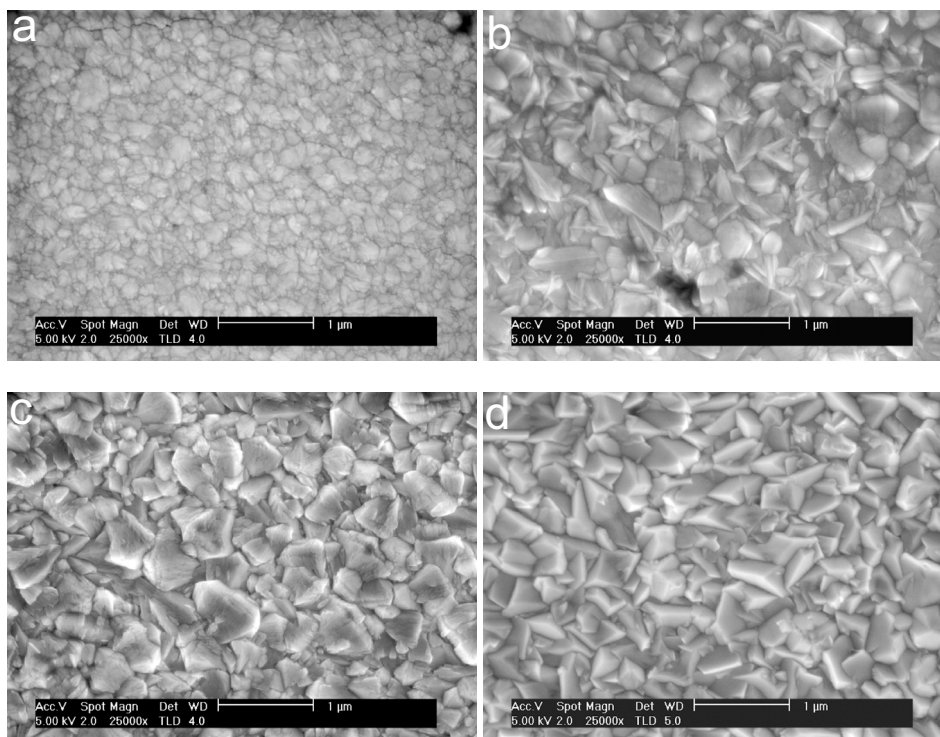


Figure 5.1: SEM micrographs of $\text{SnO}_2\text{:F}$ on glass made by APCVD (a) from TMT, (b) from MBTC, (c) from TTC, and (d) of Asahi U-type.

concentration than the Asahi U-type, which can explain a part of the absorption losses. Probably this can explain the difference in transmittance between the TTC sample deposited here and the Asahi U-type TCO. For the TMT sample, the lower transmittance in the blue is ascribed to higher reflectance as a result of the flat film surface and thus the absence of the anti-reflection effect by refractive index matching at the TCO/air interface. The abrupt transition in refractive index in combination with a low haze leads also to a high specular reflectance at the TCO/air interface, which explains the sharp interference fringes observed in the transmittance spectrum. The MBTC sample has a significantly lower transmittance than the other $\text{SnO}_2\text{:F}$ layers. As only a small fraction of these additional losses can be attributed to the larger thickness of the sample, this indicates a higher concentration of defects, possibly as a result of non-activated dopants or carbon incorporation into the film. After a severe hydrogen plasma treatment, under harsher conditions than during the actual deposition of amorphous silicon solar cells, the

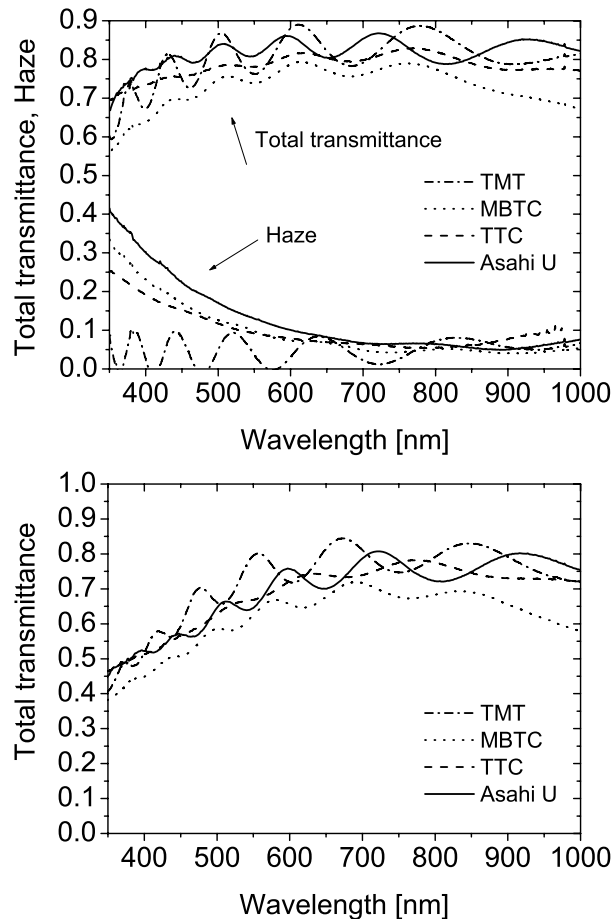


Figure 5.2: Upper graph: Total transmittance and haze spectra of $\text{SnO}_2\text{:F}$ on glass made from TMT, MBTC, TTC, and of Asahi U-type. Lower graph: Total transmittance of the samples after a severe hydrogen plasma treatment.

transmittance of all four TCO layers is lowered due to chemical reduction of the $\text{SnO}_2\text{:F}$ into SnO and possibly even metallic Sn . The differences in total transmittance among the four samples do not change, indicating a comparable resistance to the hydrogen plasma of all four TCOs, and resulting in the MBTC layer still having the lowest transmittance after the treatment. The angular resolved scattering curves in Figure 5.3 follow the trend observed in the haze value. The TTC sample scatters as much light to large angles above 50° as the Asahi U-type TCO and has an onset, though less pronounced, of the characteristic shoulder found for

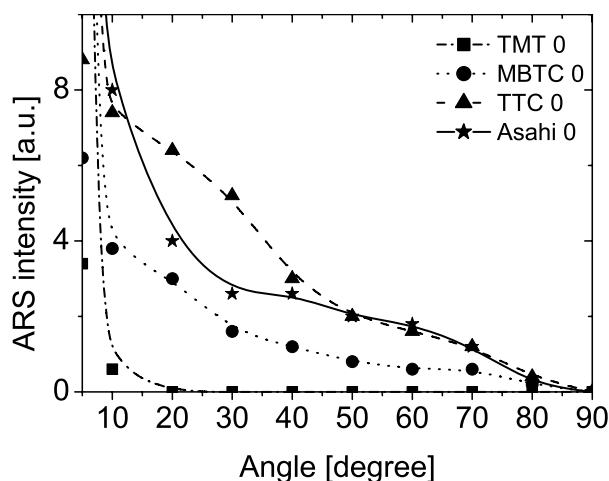


Figure 5.3: Angular resolved scattering curves of $\text{SnO}_2\text{:F}$ layers on glass made from TMT, MBTC, TTC, and of Asahi U-type.

the Asahi U-type TCO in ARS measurements.

5.4.2 Solar Cells

Amorphous silicon pin solar cells have been deposited simultaneously on the three $\text{SnO}_2\text{:F}$ layers made from different Sn precursors, and on Asahi U-type TCO.

Figure 5.4 shows the dark IV characteristics of the solar cells. The curves were fitted by a single-diode equation. The characteristic parameters dark saturation current J_0 and diode quality factor n are listed in Table 5.3. It is obvious that the best diode quality factor and J_0 are obtained on the Asahi TCO. While MBTC and TTC lead to a reasonable performance with slightly higher J_0 and n , the solar cells on the TMT sample suffer from severe shunting, which also lead to problems in fitting the characteristics with the single-diode model due to lack of a linear region in the semi-logarithmic dark IV curve. This shunting may be caused by sharp features, or more probably by steep valleys and trenches at the surface of the TCO. This is in accordance with our findings for solar cells deposited on Al doped ZnO layers with low surface roughness as described in chapter 4. The slightly lower diode quality factor and higher J_0 of the cells on the TTC and TMT samples as compared to Asahi can be ascribed to a less suitable surface morphology which can induce more defect-rich initial growth of the amorphous silicon layers. As described in chapter 4, thermal generation and recombination

| | TMT | MBTC | TTC | Asahi U |
|--------------------------------|-------------------|----------------------|----------------------|----------------------|
| Efficiency [%] | 5.66 | 6.86 | 8.24 | 8.33 |
| J_{sc} [mA/cm ²] | 12.63 | 13.48 | 15.73 | 16.24 |
| V_{oc} [V] | 0.76 | 0.76 | 0.76 | 0.76 |
| FF | 0.59 | 0.67 | 0.69 | 0.68 |
| R_s [Ωcm^2] | 8.8 | 7.0 | 4.9 | 5.3 |
| R_p [Ωcm^2] | 579 | 1498 | 1079 | 1553 |
| n | No reasonable fit | 1.82 | 1.78 | 1.48 |
| J_0 [mA/cm ²] | No reasonable fit | 3.5×10^{-7} | 3.0×10^{-7} | 3.2×10^{-8} |

Table 5.3: Dark IV and solar cell parameters of a-Si:H pin cells deposited on 4 different SnO₂:F superstrates.

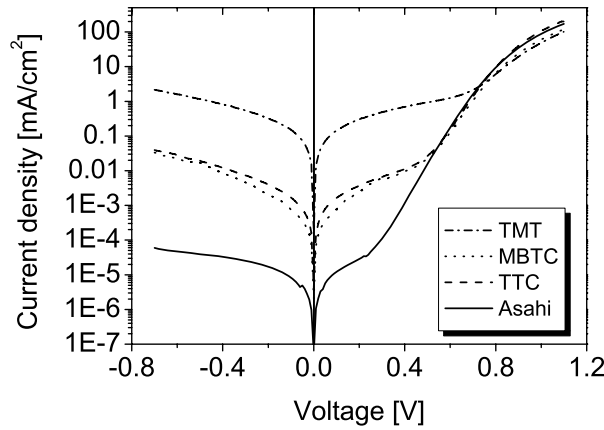


Figure 5.4: Dark IV curves of a-Si:H pin solar cells deposited on 4 different SnO₂:F superstrates.

in a defect rich p/i region in the dark due to a higher defect density directly lead to lower J_0 and higher n .

The diode quality is also reflected in the light IV measurements (see Figure 5.5 and Table 5.3). It has to be noted that the cell on the Asahi reference TCO performs slightly worse than usual, indicating unoptimized solar cell deposition conditions. As mainly the fill factor and V_{oc} are affected, and also a slightly increased R_s is observed, most probably one of the doped layers has a too high activation energy and is at the same time too resistive, leading to a lower built-in field and thus V_{oc} , and higher R_s , respectively. However, all solar cell parameters are good enough to allow a realistic comparison of the four TCOs.

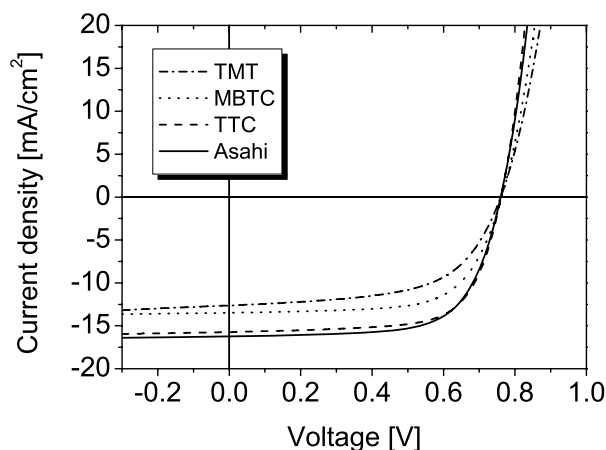


Figure 5.5: Light IV curves of a-Si:H pin solar cells deposited on 4 different $\text{SnO}_2\text{:F}$ superstrates.

The TMT cell suffers from a low fill factor, which can directly be related to the above explained shunting and low diode quality induced by the TCO morphology. Also Gordon *et al.* [78] observed a lower FF for their cells on flat TCO compared to rough TCO, and ascribed it to the geometry of the TCO. A remarkable result has been achieved here for the cell on the TTC sample, which approaches the performance of the cell on Asahi U-type. Interestingly, this was achieved with a TCO exhibiting a haze above 10%, comparable to the Asahi U type TCO. Gordon *et al.* [78] found their optimum $\text{SnO}_2\text{:F}$ with a haze of only a few percent, as with increasing haze the deterioration in V_{oc} and FF overcompensated the gain in J_{sc} . Our findings are in good agreement with the results reported by Kim *et al.* [77], who compared differently textured $\text{SnO}_2\text{:F}$ TCOs supplied by the Asahi company and realized solar cells with high V_{oc} and FF on TCOs with high haze. This again shows that a suitable morphology of the TCO is more important for the diode quality of the solar cell than the measured roughness or haze.

The cells on TCOs made from MBTC and TMT have a far lower current, while the diode quality is still sufficient to allow for reasonable V_{oc} and FF . The explanation for the differences in short circuit current of the cells can be found in the spectral response measurements shown in Figure 5.6.

All cells have a lower blue response than the cell on Asahi U-type. This can be directly related to the lower transmittance of the TCOs compared to Asahi U-type as described above. In addition to this, the absence of sufficient roughness of the TMT sample leads to a lack of antireflection effect by refractive index grading at

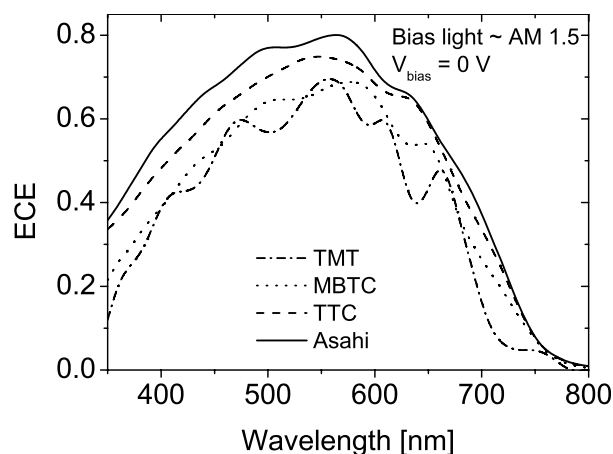


Figure 5.6: External collection efficiencies of a-Si:H pin solar cells on four different SnO₂:F superstrates..

the TCO / p-a-Si:H interface. For long wavelengths the spectral response of this rather flat cell shows pronounced interference fringes and relatively low spectral response. In contrast to this, the TTC cell exhibits efficient light trapping due to scattering at the rough TCO / p-a-Si:H interface. The high absorption losses in the MBTC layer result in far lower response over the whole spectrum, in spite of the slightly higher haze of this sample.

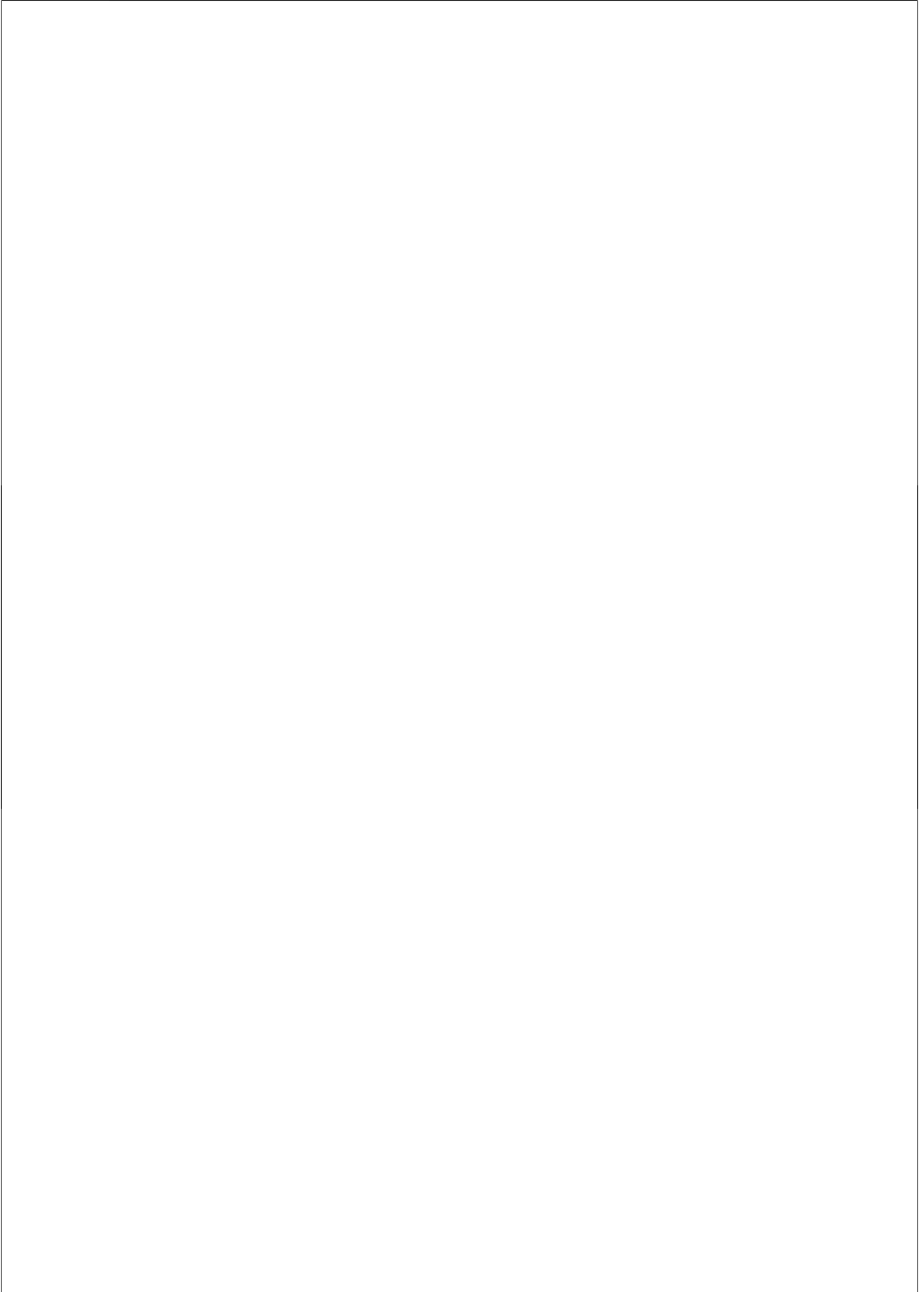
5.5 Conclusions

In conclusion, TTC is the Sn precursor which resulted in the TCO with best performance of a-Si:H pin solar cells. This can be attributed to the combination of high electron mobility and a superior surface texture, allowing for a relatively thin and highly transparent TCO with sufficient conductivity and good light scattering properties. Asahi U-type yields slightly higher current, due to an even better blue response of the solar cell. The superior morphology of the Asahi U-type is only visible in the dark diode characteristics. The TMT sample is too flat, leading to a low photocurrent due to the absence of light trapping for long wavelengths and antireflection effect for short wavelength light. Comparable to the case of Al doped ZnO deposited by ETP CVD, also for this TCO, in spite of its relatively flat surface, too steep surface features lead to a deteriorated diode quality and even shunting of the solar cells. The MBTC sample has high haze, but suffers from

low transmittance due to absorption losses, reducing the spectral response at all wavelengths and thus the short circuit current. The diode quality on this TCO is comparable to the TTC sample.

As for each precursor only preliminary studies resulting in the chosen parameter settings have been performed prior to this study, part of the accessible parameter space has not been taken into account. Further parameter variations and optimizations for each of the mentioned precursors might lead to TCOs with different morphology and thus possibly even better properties as front TCO for amorphous silicon pin solar cells than readily achieved.

In accordance with the conclusions from our experiments with solar cells on undoped and aluminum doped zinc oxide in chapter 4, a high surface roughness and haze do not necessarily lead to a lower diode quality, and vice versa. In further TCO optimization, a promising path should be the search for morphologies that efficiently scatter the light, while at the same time allow the deposition of high quality amorphous silicon. This will lead to solar cells with high fill factor and open circuit voltages, that can thus take full advantage of the high photocurrent as a result of the optimized light trapping properties.



6 Summary

In order to slow down the global warming resulting from excessive fossil energy production and consumption, the need for renewable energy sources has become evident. Several recently published studies ascribe solar energy and in particular photovoltaic systems a major role for the transition from electricity production by fossil fuels to energy conversion by renewable energy sources. Due to the huge amount of conventional power plants and the only beginning growth of the markets for photovoltaic systems, even scenarios with an annual growth rate of 30%, as needed to comply with the goals of e.g. the European Union and the German Government, it will take until 2030 before the share of energy production covered by photovoltaic systems will become significant. Following the above mentioned studies, in 2050 it will amount to 20%, and by the year 2100 solar energy will be the major energy source. Probably the most important goal, which has to be achieved in order to realize these scenarios is a substantial reduction in the price of photovoltaic systems, which can be achieved by a decrease in production costs. The actual solar module, which converts sunlight into electricity, causes about 50% of the cost of a photovoltaic system. To decrease this cost, thin-film silicon technology has several advantages with respect to the currently dominating crystalline silicon wafer technologies. Thin-film solar cells can be deposited on cheap substrates, and the necessary amount of the silicon absorber material is between 100 and 1000 times smaller. Also the demands to purity and crystallographic quality of the material can be greatly relieved. The necessary step in crystalline silicon wafer technology of interconnecting individual solar cells into modules can be replaced by monolithic series connection on a substrate during device fabrication itself in thin-film technology. Amorphous and microcrystalline silicon, having band gaps of 1.7 and 1.1 eV, respectively, form a perfect combination in stacked tandem solar cells to make more efficient use of the solar spectrum and achieve higher efficiencies than single junction cells. Record efficiencies of 14.7% have been reported for such 'micromorph' tandem cells.

This thesis describes research on single junction amorphous and microcrystalline silicon solar cells with focus on the important role of the transparent conductive oxide (TCO) for such devices. In addition to the formation of a transparent and electrically conductive front electrode for the solar cell allowing photocurrent collection with low ohmic losses, the front TCO plays an important role for the light enhancement of thin-film silicon pin type solar cells. If the TCO is rough,

light scattering at rough interfaces in the solar cell in combination with a highly reflective back contact leads to an increase in optical path length of the light. Multiple (total) internal reflectance leads to virtual 'trapping' of the light in the solar cell structure, allowing a further decrease in absorber thickness and thus thin-film silicon solar cell devices with higher and more stable efficiency. While Asahi U-type $\text{SnO}_2\text{:F}$ represents a high quality TCO available on medium size areas for research, there is an urgent need for high quality TCOs with uniform properties on large areas and in large quantities, which can be fabricated at low cost. In the research described in this thesis, the optical mechanisms involved in the light trapping in thin-film silicon solar cells have been studied. Two types of front TCO materials have been investigated with respect to their suitability as front TCO in thin-film silicon pin type solar cells.

Undoped and aluminum doped zinc oxide layers have been fabricated for the first time by the expanding thermal plasma chemical vapor deposition (ETP CVD) technique. Natively textured undoped (ZnO) and aluminum doped (ZnO:Al) layers have been deposited between 150°C and 350°C at a deposition rate between 0.2 and 1.3 nm/s. Films exhibiting native texture, electrical (sheet resistance $< 10 \Omega/\square$) and optical (transmittance $> 80\%$) properties comparable to Asahi U-type reference $\text{SnO}_2\text{:F}$ have been obtained. The influence of several deposition parameters on the structural, morphological, and optoelectrical properties of the films have been studied. The surface roughness of the ZnO layers increases with growing film thickness indicating the successive evolution of native roughness during growth of the ZnO film. Crystallite size and surface roughness of the films also increase with increasing substrate temperature. For undoped ZnO, a transition is observed between 250°C and 350°C from columnar growth with the c-axis of the hexagonal crystal ([002] direction) perpendicular to the substrate, to granular growth exhibiting additional grains with [103], [101], and [102] orientation. This transition is accompanied by a change in surface structure from a sharp texture stemming from the tips of the crystallite columns to more rounded features due to the granular structure. All these layers show, regardless of their morphology, optoelectronic properties comparable to the Asahi U-type reference $\text{SnO}_2\text{:F}$ TCO.

Doping of the zinc oxide can improve the stability of the electrical properties of the films. By the addition of trimethylaluminum into the reaction chamber, highly conductive Al doped ZnO layers with high optical transmittance above 80% for visible light have been obtained at substrate temperatures ranging from 150°C to 300°C . However, film growth characteristics and structure are significantly different from those of the presented undoped layers, resulting in films with a flatter surface exhibiting lower haze. An increase of the Ar flow through the cascaded arc plasma source leads to an increase in surface roughness, but at the same time

the conductivity of the aluminum doped ZnO layers decreases, comparable to the case of undoped ZnO films deposited at increased Ar flow.

The natively textured undoped ZnO films deposited by ETP CVD are highly suitable as a front electrode material for amorphous silicon pin solar cells. Solar cells with efficiencies comparable to cells on Asahi U-type reference TCO have been reproducibly obtained. No significant difference in the cell performance has been observed between cells on ZnO films with columnar or granular structure. A higher haze is needed for the ZnO samples studied here than for Asahi U-type TCO in order to achieve comparable long wavelength response of the solar cells. This is attributed to the different angular distribution of the scattered light, showing higher scattering intensities at large angles for the Asahi U-type TCO. In spite of this, the combination of higher haze and higher transmittance of the ETP ZnO resulted in slightly higher current densities than on Asahi U-type. A barrier at the TCO/p interface and minor collection problems may explain the slightly lower fill factors obtained for the cells on ETP ZnO. The solar cells deposited on the first doped ZnO:Al layers suffered from collection problems reducing the fill factor, and shunting. This is attributed to the steep trenches, sharp features and vertical steps that have been identified at the TCO surface. These steep features give rise to defective lower density regions during thin film silicon deposition, leading to higher recombination and leakage currents in the cell. The ZnO:Al layers with granular structure, deposited at higher argon flow through the cascaded arc plasma source, allowed for fill factors of the solar cells up to 0.70, comparable to cells on undoped ZnO. The best solar cell on doped ZnO:Al deposited by ETP CVD achieved an efficiency of 9.3% which is comparable to the 9.4% obtained on Asahi U-type SnO₂:F. Microcrystalline silicon solar cells deposited on ETP ZnO benefit from the excellent light trapping properties and high transmittance of the TCO for long wavelengths up to 1100 nm. The high sheet resistance around 20 Ω/□, however, gives rise to a low fill factor of 0.61, lower than the value of 0.73 obtained for the reference cell on texture-etched ZnO:Al from Forschungszentrum Jülich (FZJ), Germany.

Fluorinated tin oxide (SnO₂:F) has been deposited by Atmospheric Chemical Vapor Deposition (APCVD). This technique is also used for the fabrication of the SnO₂:F layers on glass currently used in industry for thin-film silicon solar cell production, as well as for the best reference SnO₂:F layers (Asahi U-type) on medium size area for research applications. In this work, SnO₂:F layers have been deposited on glass from three different tin precursors, tetramethyltin (TMT), monobutyltin trichloride (MBTC), and tin tetrachloride (TTC). TTC is the Sn precursor which resulted in the TCO with the best performance of a-Si:H pin solar cells. This can be attributed to the combination of high electron mobility and a

superior surface texture, allowing for a relatively thin and highly transparent TCO with sufficient conductivity and good light scattering properties. Asahi U-type yields slightly higher current, due to an even better blue response of the solar cell. The superior morphology of the Asahi U-type is only visible in the dark diode characteristics. The use of TMT leads to a very flat TCO surface, giving rise to a low photocurrent due to the absence of light trapping for long wavelengths and antireflection effect for short wavelength light. Comparable to the case of Al doped ZnO deposited by ETP CVD, also for this TCO, in spite of its relatively flat surface, too steep surface features lead to a deteriorated diode quality and even shunting of the solar cells. The MBTC sample has high haze, but suffers from low transmittance due to absorption losses, reducing the spectral response at all wavelengths and thus the short circuit current. The diode quality on this TCO is comparable to the TTC sample. In accordance with the conclusions from our experiments with solar cells on undoped and aluminum doped zinc oxide, a high surface roughness and haze do not necessarily lead to a lower diode quality, and vice versa.

Outlook

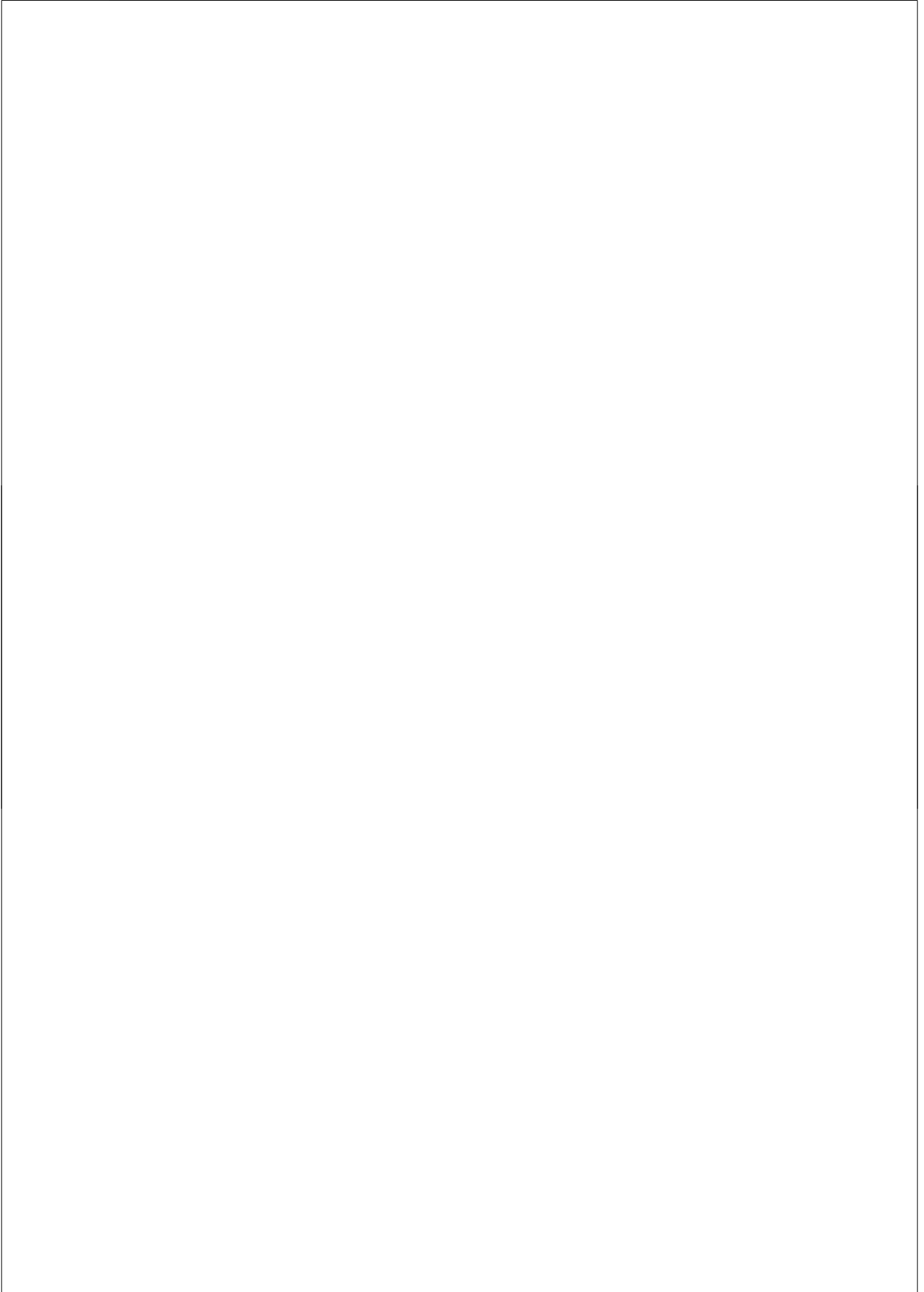
A better understanding of the gas phase and film surface reactions during the growth of ZnO and ZnO:Al layers by ETP CVD is desirable. Future research could be directed towards further optimization of the electrical and optical properties simultaneously by combining results from the presented series. Also the full potential of high rate deposition by ETP CVD still has to be proven for the deposition of zinc oxide by the demonstration of high quality TCOs deposited at rates above 2 nm/s as readily achieved for Low Pressure Chemical Vapor Deposition processes.

The potential barrier at the zinc oxide / p-layer interface for cells on ETP deposited ZnO and ZnO:Al needs further studies. As the losses due to such a contact barrier are significantly smaller than for the case of texture-etched ZnO:Al from FZJ, dedicated experiments with optimized p-layers are necessary to separate recombination losses in the p/i interface region from TCO/p contact losses. These losses may depend on the concentration of dopants and oxygen vacancies in the ZnO and ZnO:Al films.

For the SnO₂:F layers deposited by APCVD, for each precursor only preliminary studies resulting in the chosen parameter settings have been performed prior to this study, so that part of the accessible parameter space has not been taken into account yet. Further parameter variations and optimizations for each of the mentioned precursors might lead to TCOs with different morphology and thus

possibly even better properties as front TCO for amorphous silicon pin solar cells than readily achieved.

For further research on both zinc oxide and tin oxide optimization, a promising path is the search for morphologies that efficiently scatter the light, while at the same time allow the deposition of high quality amorphous and microcrystalline silicon. Especially for the understanding of the relation between TCO surface morphology and light scattering, and in particular the angular distribution of the scattered light, further research is necessary. This knowledge should allow to fabricate thin-film silicon solar cells with high fill factor and open circuit voltage, that can thus take full advantage of the high photocurrent as a result of their optimized light trapping properties.



References

- [1] S.F.B. Tett, P.A. Stott, M.R. Allen, W.J. Ingram, and J.F.B. Mitchell, *Nature* **399**, 569 (1999).
- [2] N.P. Gillett, F.W. Zwiers, A.J. Weaver, and P.A. Stott, *Nature* **422**, 292 (2003).
- [3] Energy for the Future: Renewable sources of energy. White Paper for a Community Strategy and Action Plan, European Commission COM(97)599final (1997).
- [4] T. Tamita, Proceedings of the 31st IEEE Photovoltaic Specialists Conference, Lake Buena Vista, Florida, USA, 2005 (to be published).
- [5] A. Milner, Proceedings of the 31st IEEE Photovoltaic Specialists Conference, Lake Buena Vista, Florida, USA, 2005 (to be published).
- [6] Wissenschaftlicher Beirat der Bundesregierung, *Welt im Wandel - Energiewende zur Nachhaltigkeit* (Springer, Berlin, Germany, 2003).
- [7] R.E.I. Schropp, C.H.M. van der Werf, M. Zeman, M.C.M. van de Sanden, C.I.M.A. Spee, E. Middelman, L.V. de Jonge-Meschaninova, P.M.G.M. Peters, A.A.M. van der Zijden, M.M. Besselink, R.J. Severens, J. Winkeler, and G.J. Jongerden, in *Mat. Res. Soc. Symp. Proc.* (Materials Research Society, Warrendale, USA, 1999), Vol. 557, pp. 713–718.
- [8] A. Jäger-Waldau, ed., *PVnet, European Roadmap for PV R&D* (European commission, Ispra, Italy, 2004).
- [9] R.B. Bergmann, J. Köhler, R. Dassow, C. Zaczek, and J.H. Werner, *Phys. Stat. Sol. A* **166**, 587 (1998).
- [10] M.A. Green, *Silicon Solar Cells - Advanced Principles and Practice* (Centre for Photovoltaic Devices and Systems, University of New South Wales, Sydney, Australia, 1987).
- [11] R.A. Street, *Hydrogenated amorphous silicon*, 1 ed. (Cambridge University Press, Cambridge, 1991).
- [12] R.E.I. Schropp, M. Zeman, *Amorphous and Microcrystalline Silicon Solar Cells - Modeling, Materials and Device Technology* (Kluwer Academic Publishers, Norwell, Massachusetts, USA, 1998).
- [13] D.L. Staebler, C.R. Wronski, *Appl. Phys. Lett.* **31**, 292 (1977).
- [14] D.E. Carlson, G. Lin, and G. Ganguly, in *Proceedings of the 28th IEEE Photovoltaic Specialists Conference, Anchorage, Alaska, 2000* (IEEE, Piscataway, USA, 2000), pp. 707–712.

- [15] H.M. Branz, Phys. Rev. B **59(8)**, 5498 (1999).
- [16] G. Schumm, Phys. Rev. B **49(4)**, 2427 (1994).
- [17] W.E. Spear, P.G. LeComber, Solid State Comm. **17**, 17 (1975).
- [18] K. Zweibel, Chem. Eng. News **64**, 34 (1986).
- [19] J. Meier, S. Dubail, R. Flückiger, D. Fischer, H. Keppner, and A. Shah, in *Proceedings of the 1st World Conference and Exhibition on Photovoltaic Solar Energy Conversion, Hawaii, 1994* (IEEE, Piscataway, USA, 1994), pp. 409–412.
- [20] K. Yamamoto, A. Nakajima, M. Yoshimi, T. Sawada, S. Fukuda, T. Suezaki, M. Ichikawa, Y. Koi, M. Goto, T. Meguro, T. Matsuda, M. Kondo, T. Sasaki, Y. Tawada, Solar Energy (to be published).
- [21] H.W. Deckman, Appl. Phys. Lett. **42(11)**, 968 (1983).
- [22] J. Yang, A. Banerjee, T. Glatgelder, S. Sugiyama, and S. Guha, in *Proceedings of the 26th IEEE Photovoltaic Specialists Conference, Anaheim, USA, 1997* (IEEE, Piscataway, USA, 1997), pp. 563–568.
- [23] B. Rech, T. Roschek, T. Repmann, J. Müller, R. Schmitz, W. Appenzeller, Thin Solid Films **427**, 157 (2003).
- [24] S. Guha, J. Yang, K. Hoffman, S. Sugiyama, and J. Call, in *Proceedings of the 26th IEEE Photovoltaic Specialists Conference, Anaheim, USA, 1997* (IEEE, Piscataway, USA, 1997), pp. 607–610.
- [25] H.L. Hartnagel, A.L. Dawar, A.K. Jain, and C. Jagadish, *Semiconducting Transparent Thin Films* (Institute of Physics Publishing, Bristol, UK, 1995).
- [26] J. Wallinga, Ph.D. thesis, Utrecht University, The Netherlands, 1998.
- [27] D.E. Carlson, B.F. Williams, U.S. Patent **4,442,310**, (1984).
- [28] E. Burstein, Phys. Rev. **93**, 632 (1954).
- [29] B.E. Sernelius, K.-F. Berggren, Z.-C. Jin, and C.G. Granqvist, Phys. Rev. B **37(17)**, 10244 (1988).
- [30] T. Minami, H. Nanto, and S. Takata, Jpn. J. Appl. Phys. **23(5)**, L280 (1984).
- [31] K. Ellmer, J. Phys. D **34**, 3097 (2001).
- [32] T.J. Coutts, D.L. Young, and X. Li, W.P. Mulligan, X. Wu, J. Vac. Sci. Technol. A **18(6)**, 2646 (2000).
- [33] B. Rech, C. Beneking, S. Wieder, U. Zastrow, F. Birmans, W. Appenzeller, O. Kluth, H. Stiebig, J. Fölsch, H. Wagner, W. Frammelsberger, R. Geyer, P. Lechner, H. Rübél, H. Schade, and H. Maurus, in *Proceedings of the 2nd World Conference and Exhibition on Photovoltaic Solar Energy Conversion, Vienna, 1998* (European Commission DG JRC, Ispra, Italy, 1998), pp. 391–396.
- [34] V. Srikant and D.R. Clarke, J. Appl. Phys. **83(10)**, 5447 (1998).

- [35] G. Neumann, *Phys. Stat. Sol. B* **105**, 605 (1981).
- [36] E. Ziegler, A. Heinrich, H. Oppermann, and G. Stöver, *Phys. Stat. Sol. A* **66**, 635 (1981).
- [37] H. Ohta, K. Nomura, H. Hiramatsu, K. Ueda, T. Kamiya, M. Hirano, and H. Hosono, *Sol.-Stat. Elect.* **47**, 2261 (2003).
- [38] H. Kawazoe, H. Yanagi, K. ueda, and H. Hosono, *MRS Bull.* **25(8)**, 28 (2000).
- [39] S.-C. Lin, C.-J. Huang, M.-T. Kuo, L.-C. Kuo, in *Proceedings of the 19th European Conference on Photovoltaic Solar Energy Conversion, Paris, France, 2004* (WIP and ETA, Munich, Germany, and Florence, Italy, 2004).
- [40] S.K. Hazra, S. Basu, *Solid State Comm.* (to be published).
- [41] C.G. van de Walle, *Phys. Rev. Lett.* **85**, 1012 (2000).
- [42] O. Kluth, Ph.D. thesis, RWTH Aachen, Germany, 2001.
- [43] J.A. Anna Selvan, Ph.D. thesis, Université de Neuchâtel, Switzerland, 1998.
- [44] S. Fajÿ, U. Kroll, C. Bucher, E. Vallat-Sauvain, and A. Shah, *Sol. Energy Mater. Sol. Cells* (in press).
- [45] J. Hu, and R.G. Gordon, *J. Appl. Phys.* **71(2)**, 880 (1992).
- [46] B. Sang, A. Yamada, and M. Konagai, *Jpn. J. Appl. Phys.* **37**, L1125 (1998).
- [47] J. Meier, U. Kroll, S. Dubail, S. Golay, S. Fajÿ, J. Dubail, and A. Shah, in *Proceedings of the 28th IEEE Photovoltaic Specialists Conference, Anchorage, Alaska, 2000* (IEEE, Piscataway, USA, 2000), pp. 746–749.
- [48] B. Sang, K. Dairiki, A. Yamada, and M. Konagai, *Jpn. J. Appl. Phys.* **38**, 4983 (1999).
- [49] T. Nakada, Y. Ohkubo, and A. Kunioka, *Jpn. J. Appl. Phys.* **30**, 3344 (1991).
- [50] O. Kluth, B. Rech, L. Houben, S. Wieder, G. Schöpe, C. Beneking, and H. Wagner, *Thin Solid Films* **351**, 247 (1999).
- [51] N.-P. Harder, D. Le Bellac, E. Royer, B. Rech, G. Schöpe, J. Müller, in *Proceedings of the 19th European Conference on Photovoltaic Solar Energy Conversion, Paris, France, 2004* (WIP and ETA, Munich, Germany, and Florence, Italy, 2004), pp. 1355–1358.
- [52] W.M.M. Kessels, R.J. Severens, A.H.M. Smets, B.A. Korevaar, G.J. Adriaenssens, D.C. Schram, and M.C.M. van de Sanden, *J. Appl. Phys.* **89**, 2404 (2001).
- [53] C. Smit, E.A.G. Hamers, B.A. Korevaar, R.A.C.M.M. van Swaaij, M.C.M. van de Sanden, *J. Non-Cryst. Solids* **299-302**, 98 (2002).

- [54] J. Hong, W.M.M. Kessels, F.J.H. Assche, H.C. Rieffe, W.J. Soppe, A.W. Weeber, and M.C.M. van de Sanden, *Prog. Photovolt. Res. Appl.* **11**, 125 (2003).
- [55] M.C.M. van de Sanden, J.M. de Regt, and D.C. Schram, *Phys. Rev. E* **47**, 2792 (1993).
- [56] M.C.M. van de Sanden, and J.A. Tobin, *Plasma Sources Sci. Technol.* **7**, 28 (1998).
- [57] A. Madan, P. Rava, R.E.I. Schropp, *Appl. Surf. Sci.* **70-71**, 716 (1993).
- [58] R.E.I. Schropp, U.S. Patent **6,242,687**, (2001).
- [59] C.A.M. Stap, H. Meiling, G. Landweer, J. Bezemer, and W.F. van der Weg, in *Proceedings of the 9th European Conference on Photovoltaic Solar Energy Conversion, Freiburg, Germany, 1989* (Kluwer Academic, The Netherlands, 1989).
- [60] K. Grandin, A. Roos, *Appl. Opt.* **33(25)**, 6098 (1994).
- [61] Y. Gotoh, K. Adachi, and M. Mizuhashi, *Reports of the Research Labs, Asahi Glass Co., Ltd.* **37(1)**, 13 (1987).
- [62] Wolfgang Theiss, www.mtheiss.com.
- [63] M. Tanielian, M. Chatani, H. Fritzsche, V. Smíd, and P. D. Persans, *J. Non-Cryst. Solids* **35-36**, 575 (1980).
- [64] K. Sato, Y. Gotoh, Y. Wakayama, Y. Hayashi, K. Adachi, and H. Nishimura, *Reports of the Research Labs, Asahi Glass Co., Ltd.* **42**, 129 (1992).
- [65] J. Meier, U. Kroll, E. Vallat-Sauvain, J. Spitznagel, U. Graf, and A. Shah, *Solar Energy* (to be published).
- [66] J. Müller, B. Rech, J. Springer, and M. Vanecek, *Solar Energy* **77(6)**, 917 (2004).
- [67] R. Groenen, J.L. Linden, H.R.M. van Lierop, D.C. Schram, A.D. Kuypers, and M.C.M. van de Sanden, *Appl. Surf. Sci.* **173**, 40 (2001).
- [68] J. Wienke, L. Laas, B. van Lierop, J.L. Linden, NOVEM project report HAM-RPT-98.291 (1998).
- [69] J. Löffler, R. Groenen, P.M. Sommeling, J.L. Linden, M.C.M. van de Sanden, R.E.I. Schropp, in *Solid State Phenomena - Polycrystalline Semiconductors VI - Bulk Materials, Thin Films, and Devices*, edited by O. Bonnaud, T. Mohammed-Brahim, H.P. Strunk, J.H. Werner (Scitech Publ., Uetikon am See, Switzerland, 2001).
- [70] H.P. Klug and L.E. Alexander, *X-Ray Diffraction Procedures for Polycrystalline and Amorphous Materials* (John Wiley & Sons, New York, USA, 1974).
- [71] W.W. Wenas, A. Yamada, M. Konagai, and K. Takahashi, *Jpn. J. Appl. Phys.* **30, No. 3B**, L441 (1991).

- [72] R. Groenen, E.R. Kieft, J.L. Linden, and M.C.M. van de Sanden, in *Proceedings of the PV in Europe Conference, Rome, Italy, 2002* (WIP and ETA, Munich, Germany, and Florence, Italy, 2002).
- [73] S. Major, A. Banerjee, and K.L. Chopra, *J. Mater. Res.* **1**(2), 300 (1986).
- [74] O. Caporaletti, *Solid State Comm.* **42**, 109 (1982).
- [75] R. Groenen, E.R. Kieft, J.L. Linden, and M.C.M. van de Sanden, in *Mat. Res. Soc. Symp. Proc.*, edited by R.B. Schwarz, G. ceder, and S.A. Ringel (Materials Research Society, Warrendale, USA, 2002), Vol. 730, p. 391.
- [76] J.C. Simpson and J.F. Cordero, *J. Appl. Phys.* **63**, 1781 (1988).
- [77] W.-Y. Kim, A. Shibata, Y. Kazama, M. Konagai, and K. Takahashi, *Jpn. J. Appl. Phys.* **28**(3), 311 (1989).
- [78] R.G. Gordon, J. Priscia, *Sol. Energy Mater.* **18**, 263 (1989).
- [79] O. Kluth, C. Zahren, H. Stiebig, B. Rech, and H. Schade, in *Proceedings of the 19th European Conference on Photovoltaic Solar Energy Conversion, Paris, France, 2004* (WIP and ETA, Munich, Germany, and Florence, Italy, 2004).
- [80] P. Lechner, R. Geyer, H. Schade, B. Rech, O. Kluth, H. Stiebig, in *Proceedings of the 19th European Conference on Photovoltaic Solar Energy Conversion, Paris, France, 2004* (WIP and ETA, Munich, Germany, and Florence, Italy, 2004).
- [81] H. Schade, P. Lechner, R. Geyer, H. Stiebig, B. Rech, O. Kluth, *Proceedings of the 31st IEEE Photovoltaic Specialists Conference, Lake Buena Vista, Florida, USA, 2005* (to be published).
- [82] H. Stiebig, F. Siebke, W. Beyer, C. Beneking, and H. Wagner, *Sol. Energy Mater. Sol. Cells* **48**, 351 (1997).
- [83] E. Yablanovitch and G.D. Cody, *IEEE Trans. Electron Devices* **ED-29**, 300 (1982).
- [84] C. Walker, R.E. Hollingsworth, and A. Madan, in *Mat. Res. Soc. Symp. Proc.*, edited by A. Madan, M. Thompson, D. Adler, and Y. Hamakawa (Materials Research Society, Warrendale, USA, 1987), Vol. 95, pp. 527–532.
- [85] M. Zeman, R.A.C.M.M. van Swaaij, and J.W. Metselaar, *J. Appl. Phys.* **88**(11), 6436 (2000).
- [86] C.K. Carniglia, *Opt. Eng.* **18**, 104 (1978).
- [87] G. Mie, *Ann. Phys.* **25**, 377 (1908).
- [88] C.F. Bohren, D.R. Huffman, *Absorption and Scattering of Light by Small Particles* (John Wiley & Sons, New York, USA, 1983).
- [89] H. Schade and Z. Smith, *Applied Optics* **24**(19), 3221 (1985).
- [90] J.G. O'Dowd, *Sol. Energy Mater. Sol. Cells* **16**, 388 (1987).

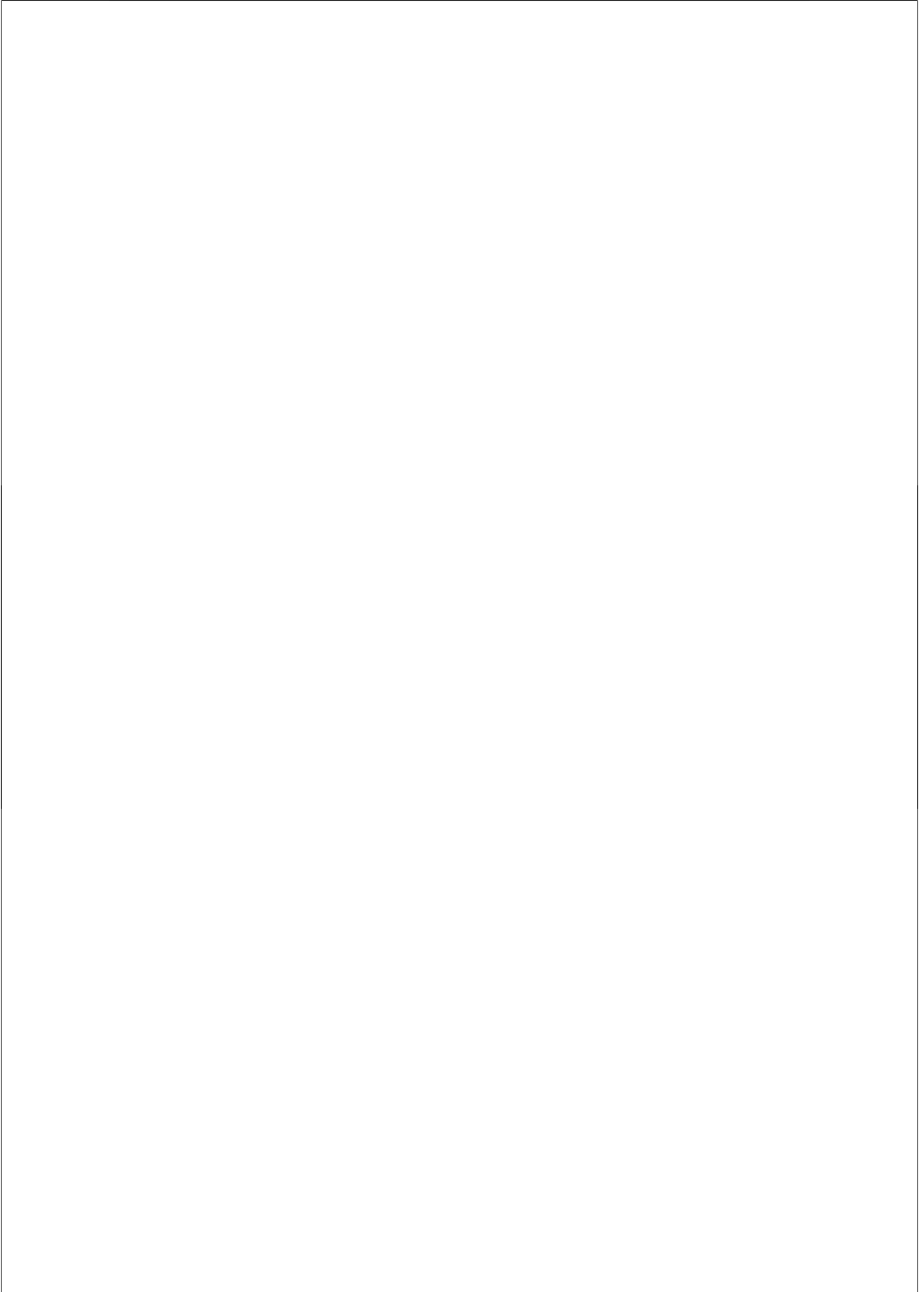
- [91] P. Chýlek, J.T. Kiehl, and A. Mugnai, *J. Opt. Soc. Am.* **69(11)**, 1550 (1979).
- [92] J. Daey Ouwens, M. Zeman, J. Loeffler and R.E.I. Schropp, in *Proceedings of the 16th European Conference on Photovoltaic Solar Energy Conversion, Glasgow, Scotland, 2000* (WIP and ETA, Munich, Germany, and Florence, Italy, 2000), pp. 405–408.
- [93] J. Krč, F. Smole, and M. Topič, *Informacije MIDEM* **32(1)**, 6 (2002).
- [94] F. Leblanc, J. Perrin, J. Schmitt, *J. Appl. Phys.* **75(2)**, 1074 (1994).
- [95] J. Krč, M. Zeman, F. Smole, and M. Topič, *J. Appl. Phys.* **92(2)**, 749 (2002).
- [96] J. Krč, M. Zeman, O. Kluth, F. Smole, and M. Topič, *Thin Solid Films* **426**, 296 (2003).
- [97] J. Krč, F. Smole, and M. Topič, *Sol. Energy Mater. Sol. Cells* (to be published).
- [98] J. Krč, F. Smole, and M. Topič, *Progr. Photovolt. Res. Appl.* **11**, 15 (2003).
- [99] J. Springer, A. Poruba, L. Müllerova, M. Vaneček, O. Kluth, and B. Rech, *J. Appl. Phys.* **95(3)**, 1427 (2004).
- [100] J. Springer, B. Rech, W. Reetz, J. Müller, and M. Vaneček, *Sol. Energy Mater. Sol. Cells* (to be published).
- [101] W.G.J.H.M. Sark, H. Meiling, J. Bezemer, M.B. von der Linden, R.E.I. Schropp, W.F. van der Weg, *Sol. Energy Mater. Sol. Cells* **45**, 57 (1997).
- [102] Y. Gupta, H. Liers, S. Woods, S. Young, R. DeBlasio, L. Mrig, in *Proceedings of the 16th IEEE Photovoltaic Specialists Conference, 1992* (IEEE, New York, USA, 1992), pp. 1092–1101.
- [103] M. Bennet, J. Newton, C. Poplawski, K. Rajan, in *Proceedings of the 23rd IEEE Photovoltaic Specialists Conference, Louisville, USA, 1993* (IEEE, Piscataway, USA, 1993), pp. 867–871.
- [104] M.K. van Veen, Ph.D. thesis, Utrecht University, The Netherlands, 2002.
- [105] S.K. O’Leary, S.R. Johnson, P.K. Lim, *J. Appl. Phys.* **82(7)**, 3334 (1997).
- [106] A. Gordijn, W.M. Arnoldbik, F.D. Tichelaar, J.K. Rath, and R.E.I. Schropp, *Appl. Phys. Lett.* **85(21)**, 5096 (2004).
- [107] A. Gordijn, J. Löffler, W.M. Arnoldbik, F.D. Tichelaar, J.K. Rath, and R.E.I. Schropp, *Sol. Energy Mater. Sol. Cells* (to be published).
- [108] S. Wieder, Ph.D. thesis, RWTH Aachen, Germany, 1999.
- [109] M. Kubon, E. Boehmer, F. Siebke, B. Rech, C. Beneking, H. Wagner, *Sol. Energy Mater. Sol. Cells* **41/42**, 485 (1996).
- [110] G. Ganguly, D.E. Carlson, S.S. Hegedus, D. Ryan, R.G. Gordon, D. Pang, R.C. Reedy, *Appl. Phys. Lett.* **85(3)**, 479 (2004).
- [111] A. Nuruddin, J.R. Abelson, *Thin Solid Films* **394**, 49 (2001).

- [112] E. Böhmer, F. Siebke, B. Rech, C. Beneking, and H. Wagner, in *Mat. Res. Soc. Symp. Proc.*, edited by D. Ginley, A. Catalano, H.W. Schock, C. Eberspacher, T.M. Peterson and T. Wada (Materials Research Society, Warrendale, USA, 1996), Vol. 426, pp. 519–524.
- [113] T. Roschek, J. Müller, S. Wieder, B. Rech, and H. Wagner, in *Proceedings of the 16th European Conference on Photovoltaic Solar Energy Conversion, Glasgow, Scotland, 2000* (WIP and ETA, Munich, Germany, and Florence, Italy, 2000).
- [114] Y. Ashida, N. Ishiguro, H. Tanaka, M. Koyama, K. Miyachi, N. Fukuda, A. Nitta, Technical Digest of the International PVSEC-5, Kyoto, Japan 367 (1990).
- [115] S.S. Hegedus, R. Kaplan, G. Ganguly, and G.S. Wood, in *Proceedings of the 28th IEEE Photovoltaic Specialists Conference, Anchorage, Alaska, 2000* (IEEE, Piscataway, USA, 2000).
- [116] K. Winz, B. Rech, T. Eickhoff, C. Beneking, C.M. Fortmann, P. Hapke, H. Wagner, in *Mat. Res. Soc. Symp. Proc.*, edited by D. Ginley, A. Catalano, H.W. Schock, C. Eberspacher, T.M. Peterson and T. Wada (Materials Research Society, Warrendale, USA, 1996), Vol. 426, pp. 819–824.
- [117] K. Itoh, H. Matsumoto, T. Kobata, A. Fujishima, O. Nakamura, K. Fukui, *Appl. Phys. Lett.* **51(21)**, 1685 (1987).
- [118] M. Kubon, Ph.D. thesis, RWTH Aachen, Germany, 1995.
- [119] S. Guhse, D. Peros, M. Wagner, M. Böhm, in *Mat. Res. Soc. Symp. Proc.*, edited by D. Ginley, A. Catalano, H.W. Schock, C. Eberspacher, T.M. Peterson and T. Wada (Materials Research Society, Warrendale, USA, 1996), Vol. 426, pp. 437–443.
- [120] F. Smole, M. Topič, J. Furlan, *J. Non-Cryst. Solids* **194**, 312 (1996).
- [121] K.B. Sundaran, A. Khan, *J. Vac. Sci. Technol. A* **15(2)**, 428 (1997).
- [122] P. Roca i Cabarocas, N. Lyadi, T. Heitz, B. Drevillon, and I. Solomon, *Appl. Phys. Lett.* **66**, 3609 (1995).
- [123] J. Rath, R.E.I. Schropp, *Sol. Energy Mater. Sol. Cells* **53**, 189 (1998).
- [124] K. Prasad, U. Kroll, F. Finger, A. Shah, J.-L. Dorier, A. Howling, J. Baumann and M. Schubert, in *Mat. Res. Soc. Symp. Proc.* (Materials Research Society, Warrendale, USA, 1991), Vol. 219, p. 383.
- [125] R. Flückinger, J. Meier, H. Keppner, M. Götz, A. Shah, in *Proceedings of the 23rd IEEE Photovoltaic Specialists Conference, Louisville, USA, 1993* (IEEE, Piscataway, USA, 1993), pp. 839–844.
- [126] A. Gordijn, J.K. Rath, and R.E.I. Schropp, *J. Appl. Phys.* **95(12)**, 8290 (2004).

- [127] J. Bailat, E. Vallat-Sauvain, L. Feitknecht, C. Droz, A. Shah, *J. Non-Cryst. Solids* **299-302**, 1219 (2002).
- [128] E. Vallat-Sauvain, S. Fäy, S. Dubail, J. Meier, J. Bailat, U. Kroll, A. Shah, in *Mat. Res. Soc. Symp. Proc.*, edited by J.B. Joyce, J.D. Cohen, R.W. Collins, J.-I. Hanna, and M. Stutzmann (Materials Research Society, Warrendale, USA, 2001), Vol. 664, p. A.15.3.1.
- [129] M. Luysberg, C. Scholten, L. Houben, R. Carius, F. Finger, O. Vetterl, in *Mat. Res. Soc. Symp. Proc.*, edited by J.B. Joyce, J.D. Cohen, R.W. Collins, J.-I. Hanna, and M. Stutzmann (Materials Research Society, Warrendale, USA, 2001), Vol. 664, p. A.15.2.1.
- [130] N. Palit and P. Chatterjee, *J. Appl. Phys.* **86(12)**, 6879 (1999).
- [131] J. Löffler, A. Gordijn, R.L. Stolk, H. Li, J.K. Rath, R.E.I. Schropp, *Sol. Energy Mater. Sol. Cells* (to be published).
- [132] H. Sakai, T. Yoshida, T. Hama, and Y. Ichikawa, *Jpn. J. Appl. Phys.* **29**, 630 (1990).
- [133] Y. Nasuno, M. Kondo, A. Matsuda, *Jpn. J. Appl. Phys.* **40**, L303 (2001).
- [134] Y. Nasuno, M. Kondo, A. Matsuda, *Jpn. J. Appl. Phys.* **41**, 3912 (2002).
- [135] A. Gordijn, J.K. Rath, R.E.I. Schropp, (to be published).
- [136] B. Rech, O. Kluth, S. Wieder, H. Siekmann, J. Müller, W. Reetz, O. Vetterl, D. Lundszen, A. Lambertz, F. Finger, H. Wagner, Technical Digest of the International PVSEC-11, Sapporo, Japan 67 (1999).
- [137] B. Szyska, *Thin Solid Films* **351**, 1641 (1999).
- [138] W. Wenas, A. De, A. Yamada, M. Konagai, K. Takahashi, *Sol. Energy Mater. Sol. Cells* **34**, 313 (1994).
- [139] P.F. Gerhardinger, R.J. McCurdy, in *Mat. Res. Soc. Symp. Proc.*, edited by D. Ginley, A. Catalano, H.W. Schock, C. Eberspacher, T.M. Peterson and T. Wada (Materials Research Society, Warrendale, USA, 1996), Vol. 426, pp. 399–410.
- [140] H. Schade and Z. Smith, *J. Appl. Phys.* **57**, 568 (1985).
- [141] A.M.B. van Mol, Ph.D. thesis, TU Eindhoven, The Netherlands, 2003.
- [142] R.G. Gordon, in *Mat. Res. Soc. Symp. Proc.*, edited by D. Ginley, A. Catalano, H.W. Schock, C. Eberspacher, T.M. Peterson and T. Wada (Materials Research Society, Warrendale, USA, 1996), Vol. 426, pp. 419–429.
- [143] K. Sato, Technical Digest of the International PVSEC-11, Sapporo, Japan 61 (1999).
- [144] Y. Kato, H. Kawahara, and M. Hyohdou, U.S. Patent **4,500,567**, (1985).
- [145] A.M.B. van Mol, F. Grob, K. Spree, C.H.M. van der Werf, R.E.I. Schropp, in *Proceedings of Chemical Vapor Deposition XVI and EuroCVD 14*, edited

by M.D. Allendorf, F. Maury, F. Teyssandier (The Electrochemical Society, Cedex, France, 2003), p. 408.

[146] A. Matsuda, *Thin Solid Films* **337**, 1 (1999).



Samenvatting

Om het broeikaseffect, dat is ontstaan door overmatige productie en gebruik van fossiele energie, af te remmen, is de behoefte aan duurzame energiebronnen steeds groter geworden. In recent gepubliceerde studies wordt hierbij een belangrijke rol toegekend aan zonne-energie, en in het bijzonder fotonvoltaïsche systemen, voor de omzetting van een elektriciteitsproductie uit fossiele brandstoffen naar het verkrijgen van energie uit duurzame bronnen. Door het grote aantal conventionele elektriciteitscentrales en de zich in de kinderschoenen bevindende groei van de markt voor fotonvoltaïsche systemen, zal zelfs voor scenario's die uitgaan van een jaarlijkse groei van 30%, zoals ten doel gesteld door o.a. de Europese Unie en de Duitse regering, het nog tot 2030 duren voordat het aandeel van fotonvoltaïsche systemen in de totale energieproductie significant wordt. Volgens boven genoemde studies, zal dit aandeel in 2050 20% zijn, en verder oplopen tot aan het jaar 2100 waarin zonne-energie de belangrijkste bron van energie zal vormen. Om een dergelijk scenario te realiseren is een substantiële reductie van de prijs van fotonvoltaïsche systemen waarschijnlijk het belangrijkste streven, wat bereikt kan worden door een vermindering van de productiekosten. Ongeveer 50% van de kosten van het fotonvoltaïsche systeem wordt veroorzaakt door de zonnemodule zelf, waarin het zonlicht wordt omgezet in elektriciteit. Om de modulekosten te doen verminderen, heeft de dunne film silicium technologie een aantal voordelen ten opzichte van de op het moment dominerende kristallijn silicium wafer technologie. Dunne film zonnecellen kunnen worden gedeponerd op goedkope substraten en de benodigde hoeveelheid silicium, het licht absorberend materiaal, is tussen de 100 en 1000 keer kleiner.

Voor hoogrendement dunne film silicium zonnecellen is het belangrijk dat zoveel mogelijk zonlicht in de cel wordt ingevangen. Ruwe oppervlakken in de zonnecel zorgen ervoor dat licht verstrooid wordt en vervolgens in de celstructuur opgesloten blijft. Hierdoor wordt meer zonlicht geabsorbeerd dat vervolgens in duurzame elektriciteit omgezet kan worden. Een manier om deze ruwe oppervlakken te verkrijgen is door gebruik te maken van getextureerde polykristallijne transparante geleidende metaaloxidelagen.

Hoewel Asahi U-type $\text{SnO}_2\text{:F}$ een voor onderzoeksdoeleinden zeer geschikt TCO (Transparante Geleidende Oxide) van goede kwaliteit is en beschikbaar is op middelgrote oppervlakken, is er een grote behoefte aan kwaliteits-TCO's met uniforme eigenschappen op grote oppervlakken die geproduceerd kunnen worden

tegen een lage kostprijs.

In dit proefschrift wordt de studie van lichtinvang in zonnecellen, de ontwikkeling van twee verschillende soorten ruwe transparante geleidende oxide lagen, en de succesvolle toepassing van deze lagen in dunne film silicium zonnecellen in het Utrecht Solar Energy Laboratory (USEL) van de Universiteit Utrecht beschreven.

De Expanding Thermal Plasma (ETP) depositietechniek, ontwikkeld aan de TU Eindhoven, is succesvol toegepast voor de vervaardiging van ruwe transparante geleidende zinkoxidelagen voor dunne film silicium zonnecellen. De eigenschappen van de zinkoxidelagen die belangrijk zijn voor de toepassing in dunne film silicium zonnecellen zijn gekarakteriseerd. De ruwheid van de films neemt tijdens de depositie toe, zodat dikkere lagen een grotere ruwheid vertonen. Verschillende proces parameters voor de vervaardiging van de zinkoxidelagen zijn gevarieerd, waarbij hun invloed op de laageigenschappen is bestudeerd. Het blijkt dat voor ongedoteerde zinkoxidelagen de kristalstructuur aanzienlijk verandert als de substraattemperatuur van 150°C naar temperaturen tussen de 250°C en 350°C verhoogd wordt. In het hele bestudeerde temperatuurgebied zijn ongedoteerde zinkoxidelagen gemaakt waarvoor de optische en elektrische eigenschappen vergelijkbaar zijn met die van conventionele tinoxidelagen. Door gericht aluminium in het zinkoxide kristalrooster in te bouwen, zijn zogenaamde gedoteerde lagen met nog betere elektrische geleiding en hoge optische transparantie verkregen. De kristalstructuur van deze lagen is echter aanzienlijk anders dan voor de ongedoteerde zinkoxidelagen. De kristalstructuur verandert ook niet bij verhoging van de substraattemperatuur tot 300°C. Een hogere argonstroom door de plasma bron kan de kristalstructuur van gedoteerde zinkoxidelagen wel beïnvloeden, de elektrische geleiding van de lagen neemt dan echter ook af.

De meestbelovende ongedoteerde en met aluminium gedoteerde zinkoxidelagen zijn getest in zonnecelstructuren van amorf silicium. Het blijkt dat voor deze toepassing specifieke eisen worden gesteld aan de ruwheid van het zinkoxide. Dunne film silicium zonnecellen op ongedoteerde zinkoxide lagen bereiken hoge rendementen, vergelijkbaar met cellen vervaardigd op conventionele tinoxidelagen. Om zonnecellen met vergelijkbare stroomgeneratie te bereiken, blijkt het vereiste lichtverstrooiend vermogen voor zinkoxide hoger te zijn dan voor tinoxide. Dit wordt toegeschreven aan het feit dat het onderzochte tinoxide meer licht onder grote hoeken verstrooit. De zonnecellen vervaardigd op de eerste gedoteerde zinkoxidelagen leverden lage rendementen op of werkten helemaal niet. De lagen die met een hogere argon stroom gemaakt zijn en dus een andere kristalstructuur hebben bleken goed geschikt te zijn voor amorf silicium zonnecellen. Het hoogst op gedoteerd zinkoxide bereikte rendement is 9.3 % en dus vergelijkbaar met de 9.4 % bereikt op conventionele tinoxidelagen. De optische

eigenschappen, zowel de transparantie als het lichtverstrooiend vermogen, van het ongedoteerde zinkoxide blijken veelbelovend, ook voor microkristallijn silicium zonnecellen. De elektrische eigenschappen moeten voor deze toepassing echter nog verbeterd worden.

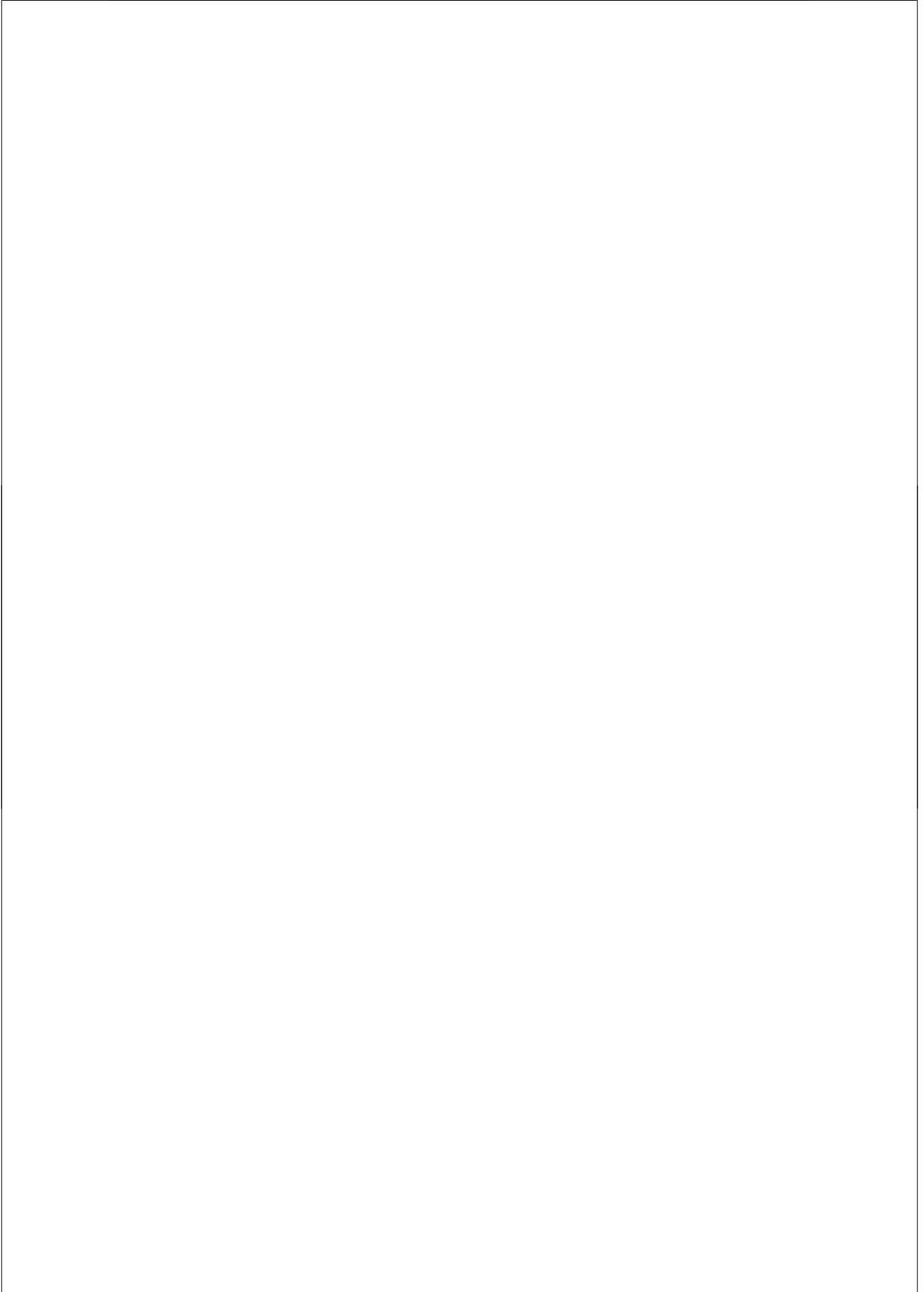
Er is ook onderzoek gedaan naar de depositie van met fluor gedoteerde tinoxidelagen met behulp van Atmospheric Pressure Chemical Vapor Deposition. Als bron voor het tin zijn in dit proces tetramethyltin (TMT), monobutylin trichloride (MBTC), en tin tetrachloride (TTC) vergeleken. Het TCO dat tot het beste rendement van amorf silicium zonnecellen leidde was vervaardigd met TTC. Dit wordt met name toegeschreven aan een hoge elektrische geleiding en hoge transparantie van het TCO, gecombineerd met een zeer geschikte oppervlakkte ruwheid. Zonnecellen die zijn gedeponeerd op het referentie Asahi U-type TCO hebben een iets hoger rendement dankzij de betere transparantie en antireflectie werking van dit TCO voor blauw licht. Het TCO gemaakt van TMT is op grond van zijn kristalstructuur niet geschikt voor amorf silicium zonnecellen, vergelijkbaar met het geval van de eerste met aluminium gedoteerde zinkoxidelagen.

Perspectief

Een nog beter begrip van de processen tijdens de depositie van zinkoxide met behulp van de ETP CVD techniek is wenselijk. Uitgaande van de resultaten van dit onderzoek zou toekomstig onderzoek gericht kunnen worden op de doelgerichte optimalisatie van de TCO lagen. Het potentieel aangaande een hoge depositiesnelheid van zinkoxidelagen van hoge kwaliteit moet voor deze techniek nog aangetoond worden.

Voor de tinoxidelagen gedeponeerd met behulp van APCVD zijn verdere depositie parameter variaties aan te bevelen om met elke tin bron de meest geschikte TCO laag te maken en hieruit te concluderen of inderdaad TTC de meest geschikte is.

In het algemeen, dus voor zowel tinoxide als voor zinkoxide, is het zoeken naar de meest geschikte oppervlakte ruwheid, die optimale licht verstrooiing veroorzaakt en tevens geschikt is voor de depositie van hoge kwaliteit amorfe en microkristallijne silicium lagen en zonnecellen, van groot belang. Met name de hoekverdeling van het verstrooide licht verdient meer onderzoek, ook bij het modelmatig beschrijven van de verstrooiing. Meer kennis op dit gebied moet goedkopere dunne film silicium zonnecellen met hoger rendement mogelijk maken.



List of publications

Publications related to this thesis

J. Löffler, R. Groenen, J.L. Linden, M.C.M. van de Sanden, R.E.I. Schropp,
Natively textured ZnO grown by PECVD as front electrode material for amorphous silicon pin solar cells

Proc. 28th IEEE Photovoltaic Specialists Conference, Anchorage, Alaska, 892-895 (2000).

R. Groenen, J. Löffler, J.L. Linden, R.E.I. Schropp, and M.C.M. van de Sanden,
Expanding Thermal Plasma CVD of Textured ZnO with Focus on Solar Cell Applications

Proc. 28th IEEE Photovoltaic Specialists Conference, Anchorage, Alaska, 822-824 (2000).

J. Daey Ouwens, J. Löffler, and R.E.I. Schropp,
Mie-Streuung in a-Si:H Solarzellen

TCO für Dünnschichtsolarzellen, FVS Workshop 2000, H. Stadermann, W. Fuhs, G. Stadermann, eds., Berlin 71-73 (2001).

J. Löffler, R. Groenen, P.M. Sommeling, J. L. Linden, M.C.M. van de Sanden, R.E.I. Schropp

Structural, optical and electrical properties of natively textured ZnO grown by PECVD for thin film solar cell applications

Polycrystalline Semiconductors VI, O. Bonnaud, T. Mohammed-Brahim, H.P. Strunk, J.H. Werner, eds., Uettikon am See, Switzerland, (2001).

J. Löffler, R. Groenen, J.L. Linden, M.C.M. van de Sanden, R.E.I. Schropp,
Amorphous Silicon Solar Cells on Natively Textured ZnO grown by PECVD

Thin Solid Films **392** 315-319 (2001).

R. Groenen, J. Löffler, J.L. Linden, R.E.I. Schropp, and M.C.M. van de Sanden,
Surface Textured ZnO Films for Thin Film Solar Cell Applications by Expanding Thermal Plasma CVD

Thin Solid Films **392** 226-230 (2001).

- J. Löffler, R. Groenen, P.M. Sommeling, J.L. Linden, E.A.G Hamers, M.C.M. van de Sanden, R.E.I. Schropp,
Undoped and aluminum doped ZnO by PECVD as natively textured superstrate TCO for amorphous silicon pin solar cells
Tech. Digest of PVSEC-12, Korea, 47-48 (2001).
- J. Löffler, R. Groenen, P.M. Sommeling, J. L. Linden, M.C.M. van de Sanden, R.E.I. Schropp,
The Influence of Front TCO Morphology on the Performance of Amorphous Silicon pin Solar Cells
Proc. PV in Europe Conference, Rome, Italy, 2002.
- J. Löffler, R. Groenen, P.M. Sommeling, J.L. Linden, M.C.M. van de Sanden, R.E.I. Schropp,
Zinkoxid-Deposition mittels expandierendem thermischen Plasma und Anwendung als TCO für Dünnschichtsolarzellen
TCO für Dünnschichtsolarzellen II, FVS Workshop 2002, Bernd Rech, H. Stadermann, eds., Berlin (2003) 98-101.
- J.L. Linden, R. Groenen, J. Löffler, P.M. Sommeling, R.E.I. Schropp, M.C.M. van de Sanden,
Property control of textured ETP CVD deposited ZnO(:Al) for application in thin film solar cells
Proc. 3rd World Conference and Exhibition on Photovoltaic Solar Energy Conversion, Osaka, Japan, 2003.
- J. Löffler, A.M.B. van Mol, F.J. Grob, J.K. Rath, R.E.I. Schropp,
Comparison of APCVD Deposited SnO₂:F Layers on Glass as TCO Superstrates for Amorphous Silicon pin Solar Cells
Proc. 19th European Photovoltaic Solar Energy Conference, Paris, France, 2004.
- R. Groenen, J. Löffler, J.L. Linden, R.E.I. Schropp, and M.C.M. van de Sanden,
Property Control of Expanding Thermal Plasma Deposited Textured Zinc Oxide with Focus on Solar Cell Applications
To be published.

Other publications

S. von Aichberger, H. Feist, J. Löffler, and M. Kunst,
In situ Monitoring of the Deposition of a-Si:H/c-Si Heterojunctions by Transient Photoconductivity Measurements
Tech. Digest of PVSEC-11, 353-354 (1999).

J. Daey Ouwens, M. Zeeman, J. Löffler, and R.E.I. Schropp,
Sensitivity of Optical Constants to the Spectral Absorption in a-Si:H Solar Cells
Proc. 16th European Photovoltaic Solar Energy Conference, Glasgow, 405-408 (2000).

R.E.I. Schropp, C.H.M. van der Werf, M.K. van Veen, P.A.T.T. Van Veenendaal, R. Jimenez Zambrano, Z. Hartman, J. Löffler, and J.K. Rath,
Thin Film a-Si/poly-Si Multibandgap Tandem Solar Cells with both Absorber Layers Deposited by Hot Wire CVD
Amorphous and Heterogeneous Silicon-Based Films, James B. Joyce, J. David Cohen, Robert W. Collins, Junichi Hanna, Martin Stutzman, eds., MRS Proceedings Volume **664** (2001).

H. de Moor, A. Jäger-Waldau, J. Herrero, M. Topič, S. Haywood, E. Özsan, M. Powalla, J. Springer, T. Schedel-Niedrig, T. Riedle, S. Siebentritt, R.E.I. Schropp, J.K. Rath, J. Löffler, J. Poortmans, J. Szlufcik, S. Pietruszko, F. Karg, P. Malbranche, B. Dimmler,
PVnet, European Roadmap for PV R&D
A. Jäger-Waldau, ed. European Commission, Ispra, Italy (2004).

R.H. Franken, M.K. van Veen, C.H.M. van der Werf, J. Löffler, J.K. Rath, and R.E.I. Schropp,
Stability of ZnO-coated SnO₂:F for High Deposition Rate Hot-Wire CVD of pin Solar Cells
Proc. 19th European Photovoltaic Solar Energy Conference, Paris, France, 2004.

R.H. Franken, C.H.M. van der Werf, J. Löffler, J.K. Rath, and R.E.I. Schropp,
Beneficial Effects of Sputtered ZnO:Al Protection Layer on SnO₂:F for High Deposition Rate Hot-Wire CVD p-i-n Solar Cells
To be published in Thin Solid Films.

C.H.M. van der Werf, H.D. Goldbach, J. Löffler, A. Scarfó, A.M.C. Kylner, B. Stannowski, W.M. ArnoldBik, A. Weeber, H. Rieffe, W.J. Soppe, J.K. Rath, and R.E.I. Schropp,

Silicon Nitride at High Deposition Rate by Hot-Wire Chemical Vapor Deposition as passivating and antireflection layer on Multicrystalline Silicon Solar Cells.

To be published in Thin Solid Films.

J. Löffler, A. Gordijn, R.L. Stolk, H. Li, J.K. Rath, R.E.I. Schropp,

Amorphous and 'micromorph' silicon tandem cells with high open circuit voltage

To be published in Solar Energy Materials and Solar Cells.

A. Gordijn, J. Löffler, W.M. Arnoldbik, F.D. Tichelaar, J.K. Rath, R.E.I. Schropp,
Thickness Determination of Thin (20 nm) Microcrystalline Silicon Layers.

To be published in Solar Energy Materials and Solar Cells.

R.E.I. Schropp, R.H. Franken, A. Gordijn, R. Jimenez Zambrano, H. Li, J. Löffler,
J.K. Rath, R.L. Stolk, M. van Veen, C.H.M. van der Werf,

Thin Film Silicon Alloys with Enhanced Stability Made by PECVD and HWCVD for Multibandgap Solar Cells

Proc. 31st IEEE Photovoltaic Specialists Conference, Lake Buena Vista, Florida, 2005 (to be published).

Nawoord

Het boekje is af. Dat was waarschijnlijk een van de eerste nederlandse zinnen die ik in het voorjaar van 1999 in een proefschrift las als voorbereiding op mijn werk in Utrecht. Inmiddels begrijp ik heel goed wat deze zin betekent ! Er is in die tijd heel veel gebeurd op mijn werk en in mijn leven, en ik wil iedereen van harte danken die er een stukje aan bijgedragen heeft.

Ten eerste natuurlijk mijn promotor Ruud Schropp. Van begin aan gaf je me de vrijheid en het vertrouwen om zelfstandig mijn onderzoek te doen, en liet je me later ook alleen naar projectvergaderingen en conferenties gaan. Tegelijk was je er altijd met advies en steun als het nodig was, en kon ik ook met dagelijkse vraagjes even je kamer binnenlopen. Een extra dank voor je ondersteuning in de drukke laatste fase tijdens het schrijven van dit boekje ! Jatin Rath wil ik bedanken voor de begeleiding van de experimenten in het ASTER systeem en de vele discussies. Het NOVEM-ZnO projectteam wil ik bedanken voor de leuke werksfeer, en de informele samenwerking. De werkbesprekingen met Roland Groenen en Paul Sommeling vond ik altijd erg vruchtbaar, en ook de projectvergaderingen met Richard van de Sanden, Hans Linden, Frank Witte, Job Swens en Jeroen Daey Ouwens waren steeds stimulerend.

Uiteraard waren de TCO monsters van TNO een basis voor dit onderzoek. Roland Groenen wil ik dan extra danken voor de zinkoxide samples - ik weet hoe veel moeite het je kostte om al mijn wensen na te komen terwijl je met de apparatuur aan het vechten was. De tinoxide samples van Ton van Mol vormden een mooie afronding van mijn onderzoek. Verder wil ik voor sample depositie en karakterisatie bij TNO Leo Toonen, Gerwin Kirchner, en Frank Grob danken. De vele SEM plaatjes die G. Hamburg (ECN) van de zinkoxide lagen gemaakt heeft, hielpen om de samenhang tussen depositieparameters, laaigeenschappen en uiteindelijk de zonnecellen beter te begrijpen.

Oliver Kluth und Bernd Rech danke ich für die gesputterten ZnO:Al Proben, die ich als Referenz für meine Experimente benutzen konnte. Auch will ich euch und den anderen Kollegen vom IPV am Forschungszentrum Jülich danken für den offenen Erfahrungsaustausch und die nette Atmosphäre, und vor allem auch die 'social events' bei den PV Konferenzen.

Marko Topič and Janez Krč from the University of Ljubljana, Slovenia, are cordially acknowledged for their kind hospitality during my stay in Ljubljana, and the possibility to use the simulation software developed at their institute. Janez,

thanks for all your efforts to introduce me to your *Sunshine* program.

In de afgelopen twee jaar heb ik heel veel geleerd en erg genoten van de goede en intense samenwerking in het Helianthos project. Iedereen uit dit grote team van harte bedankt hiervoor!

In Utrecht heeft de hele vakgroep aan het onderzoek en de uitstekende, persoonlijke werksfeer bijgedragen! Karine en Jeroen, bedankt voor alle deposities, discussies, en spontane hulp met opdampers etc. Ruurd, naast de (vooral automatiserings)technische hulp met de meetapparatuur bedankt voor uitgebreide discussies over wetenschappelijke vragen en ook de persoonlijke gesprekken - to be continued. Dirk Knoesen, bedankt voor je uitleg en training over de TEM preparatie. Pim van Maurik en Hans Meeldijk van het EMSA wil ik bedanken voor de introductie tot de transmissie-electronenmicroscop en de begeleiding met de bediening. Arja, Raul, Hanno, Andrea en Pieter - ik vond het altijd leuk en gezellig op ons kantoor. Aad, de samenwerking met jou was fantastisch - ik zal de nachtelijke activeringsenergiemetingen en de besprekingen op zondag middag niet zo snel vergeten. Sorry dat ik 'af en toe' te laat kwam. Van harte bedankt dat je de afgelopen maanden zo veel van mijn werk overnam en me daarmee de ruimte vrij maakte om aan dit boekje te schrijven.

Bernd, jij hebt een heel traject van mijn leven als studievriend, huisgenoot, collega, en projectpartner meegemaakt, en een groot deel van mijn 'inburgering' in Nederland verzorgd! Anke vulde de inburgering in het begin met haar inheemse expertenkennis deskundig aan.

Ook buiten het werk waren er veel activiteiten met de collega's, zoals de hardloopgroep met wisselende bezetting, and the international cooking conference which I enjoyed chairing, giving us the opportunity to get to know the food, drinks and of course much more of our international blend of colleagues and visitors.

Iemy, Hugo en Olaf, jullie waren de eerste vrienden die ik in Utrecht buiten het werk ontmoette. Erg leuk dat uit een apres-tennis-biertje een echte vriendschap is gegroeid. Via Hugo kwam ik bij de skibeer in Eindhoven met talloze feesten. Hier bleek ook hoe groot dit land echt is en kwam ik mijn projectpartners weer tegen. Uiteraard wil ik ook alle andere vrienden in Utrecht 'en omgeving' danken, niet te vergeten de kook- en wijn club. Eleftheria, inderdaad- no news is good news.

Natürlich will ich mich auch bei meinen 'alten' FreundInnen in Deutschland bedanken. Trotz des geographischen Abstandes wart ihr immer für mich da ! Auch meine Familie schließe ich hier ein. Vielen Dank für Eure Unterstützung.

Paula, bedankt voor de steun en rust die je me gaf, en je begrip voor mijn talloze avond- nacht- en vakantieuren achter de PC. Otto, Du wirst hoffentlich auch irgendwann verstehen was Papa tat als er mit dir auf dem Schoß am Schreibtisch saß. BEDANKT !

JOCHEN (Maart 2005)

Curriculum vitae

Jochen Löffler was born on the 17th of September 1971 in Ulm (Germany). He received the final certificate (*Abitur*) in May 1991 from the *Schulzentrum an der Bördestraße* in Bremen-Lesum, Germany. In October 1991 he started his studies of physics at the University of Bremen. In 1993, he obtained the *Vordiplom* and continued his studies at the *Rheinisch-Westfälische Technische Hochschule (RWTH)* Aachen, Germany. After a one-year stay in Barcelona, Spain, where he studied physics as a scholar of the *Deutsche Akademische Austauschdienst* at the *Universidad de Barcelona* from October 1994 till September 1995, he moved to Berlin, Germany, where he finished his studies at the *Technische Universität Berlin* in August 1998. His main subjects were 'applied semiconductor physics' and 'applied laser physics'. The research for his master thesis on the 'Optimization of a-Si/c-Si Heterostructure Solar Cells' was performed at the *Hahn-Meitner-Institut* in Berlin-Wannsee. From September 1998 till March 1999 he worked on the 'RIE texturing of multicrystalline silicon wafers for solar cells' at the RWTH Aachen. In March 1999 he joined the Surfaces, Interfaces, and Devices group of the Debye Institute at Utrecht University, where he worked on a NOVEM project on Transparent Conductive Oxides. He is co-author of the European PVnet Roadmap for R&D, and till March 2005 he worked for the Helianthos project on the development of thin-film silicon solar cells suitable for roll-to-roll production. Part of the research carried out at Utrecht University is described in this thesis. Between August 2001 and Oktober 2001 Jochen Löffler was on leave from Utrecht University to work as assistant of the head of the technology department of Q-Cells AG, Germany, during ramp-up of the production of multicrystalline silicon solar cells.

